STUDY OF AN ONLINE ELECTRON ELASTIC SCATTERING SYSTEM FOR RADIOACTIVE BEAM

Ву

Ambar C. Rodriguez Alicea

A THESIS

Submitted to
Michigan State University
in partial fulfillment of the requirements
for the degree of

Physics—Master of Science

2024

ABSTRACT

Information about the absolute charge radius of nuclei is a critical ingredient for theoretical models of the atomic structure, including the ongoing search for violations to parity conservation and physics beyond the Standard Model. This observable is best measured experimentally using the elastic electron scattering technique in which the angular dependence of the nuclear response is proportional to the charge distribution. Such information is scarce for nuclei beyond bismuth and almost non-existent for radioactive isotopes. Several worldwide facilities are either in the process of or have already coupled electron linac systems to ion storage rings or ion traps for the possibility to extend scattering experiments from stable to exotic nuclei, such as SCRIT - RIKEN in Japan, and ELISE - FAIR and DERICA - Dubna in Europe. This thesis investigates the development of an electron gun, acceleration system, and ion trap that could be coupled to a beamline like the ones at the Facility for Rare Isotope Beams (FRIB) to perform scattering experiments along with laser spectroscopy to probe rare isotopes. We first benchmark our simulation by modeling the electron Accelerator Test Facility (ATF) at Brookhaven National Laboratory (BNL) and compare our results to measurements of the electron transverse profile. We also extracted the parameters of an ion trap (e.g., trapping potential) that a linac with the desired properties could achieve, and estimated the achievable luminosity of the system. This preliminary study provides some baseline for a possible coupling of a new electron acceleration system to FRIB that could enhance the scientific reach of this facility and expand our knowledge of the nuclear structure.

This thesis is dedicated to my daughter, my mother and my beloved shrimp; thank you for supporting me with love and always believing in me. Los amo.

TABLE OF CONTENTS

CHAPTER 1 MOTIVATION	1
1.1 Electron elastic scattering	2
1.2 Beyond stable isotopes	
CHAPTER 2 THEORY	7
2.1 Electron elastic scattering	
2.2 Beam dynamics	
CHAPTER 3 TECHNOLOGIES	23
3.1 Electron Gun	
3.2 Acceleration cavities	
3.3 Ion trap	
3.4 Safety considerations	
CHAPTER 4 PRELIMINARY STUDIES	47
4.1 Electron accelerator measurements and modeling	
4.2 Ion trap and design strategy	
CHAPTER 5 SUMMARY AND OUTLOOK	62
BIBLIOGRAPHY	65
APPENDIX A: BEAM PROFILE IMAGES	71
APPENDIX B: CODES	80

CHAPTER 1

MOTIVATION

The study of nuclear physics sheds light into the fundamental forces and particles that constitute our universe. The recently built Facility for Rare Isotope Beams (FRIB), located on the campus of Michigan State University (MSU), started operation on June 10, 2022 [1]. This facility aims at unravelling the formation and evolution of stars (e.g., how are heavy elements formed from hydrogen? How many nucleons can we packed into a nucleus? What are the levels occupied by protons and neutrons inside isotopes? etc.) through the production and study of rare isotopes, their decay through beta (e^{\pm}) and gamma ray emissions, and nuclear breakout or pick-up reactions. The BEam COoler and LAser spectroscopy (BECOLA) [2] facility at FRIB focuses on one of the most fundamental properties of isotopes: their nuclear charge radii. They obtain the radius by exciting an electronic transition from two different isotopes with equal atomic number and measuring the the difference in transition energy between the two. With this information, and sometimes the help of atomic structure theory, they can infer the nuclear size. This measurement is crucial for developing accurate theoretical models of the atomic structure, as well as searches for violations to parity conservation laws and physics beyond the Standard Model of particles [3]. Despite its importance, data on this observable outside the valley of stability is scarce, with the most significant contributions dating back to the 1980's [4, 5]. This gap in knowledge hampers the advancement of nuclear theory and its applications and yet, it remains wildly unexplored.

In Figure 1.1 we present a compilation of all the existing isotopes, identified by their atomic number Z and number of neutrons N, and highlight those atoms for which the charge radii has been measured, either by electron elastic scattering or other methods.

It is important to make the distinction between nuclear charge radii measured using elastic electron scattering to those using laser spectroscopy. The latter technique, although more precise, can only measure the difference between two isotopes (sometimes this is all the information the scientist care about) and thus rely on reference atoms for which the absolute charge radius has been measured using some other independent method in order to determine the value of the radii for the

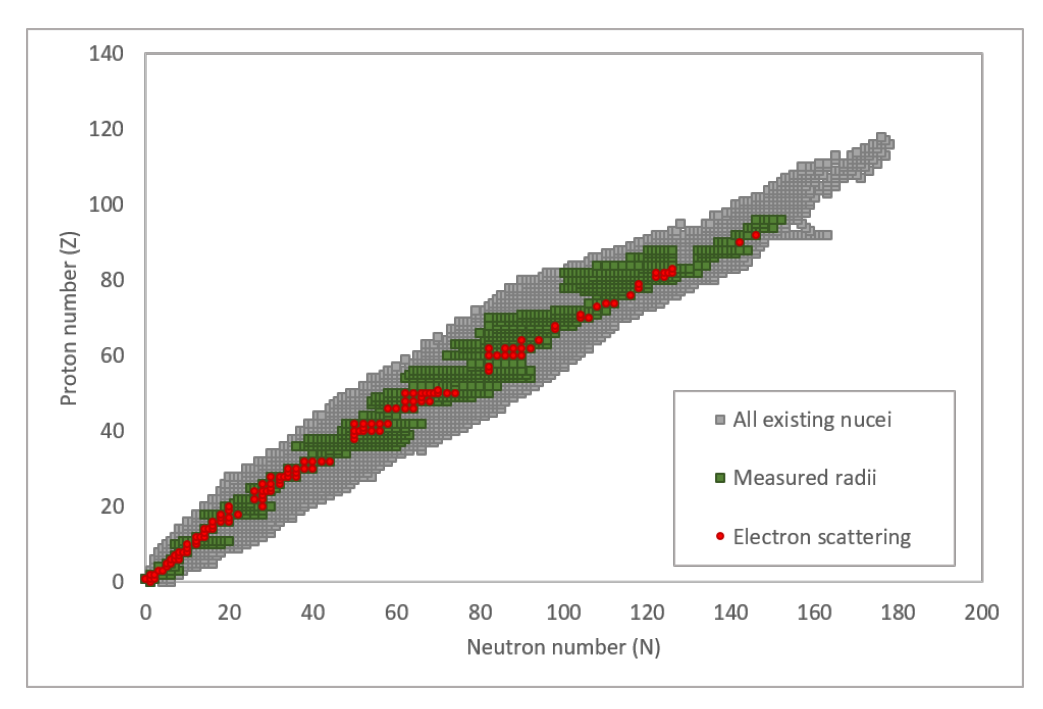


Figure 1.1 Visual representation of all discovered isotopes (grey) with color highlight on those for which the charge radius has been measured (green) and for the isotopes for which the radius was measured using electron elastic scattering (red) [4, 5].

unstable isotope. One of the few methods to this day that can measure the absolute charge radius is electron elastic scattering. Notice the significant gaps in data even within the stable isotopes in Figure 1.1 starting around Z = 35: this lack of scattering measurements inevitably means that the absolute charge radius for isotopes in that area, measured using techniques such as laser spectroscopy, will carry greater uncertainty as they need to rely on theoretical models to extrapolate for reference atoms. Another way to possibly measure the charge radius of atoms is by means of the transition X-ray energy of muonic atoms; however, just as electron scattering, these experiments have been done mainly on stable isotopes [3]. Furthermore, electron (or positron) elastic scattering allows direct measurement of the charge distribution, while others methods mostly use assumptions of the finite distribution of the nucleus to extrapolate the radius information.

1.1 Electron elastic scattering

The first scientist to perform electron scattering experiments with the purpose of determining the nuclear structure was Robert Hofstadter. In his 1953 paper [6], he explained the equipment and

experimental procedure employed to try and find evidence for the finite dimension of the atomic nucleus. Hofstadter and his team deviated the main beam from the Stanford Linear Accelerator (SLAC), about 1.922 nA average current concentrated in a few millimeter spot size with energies between 25 MeV and 150 MeV, into a scattering chamber containing thin foils of beryllium, gold, lead and tantalum. The detection scheme consisted of an analyzing magnet with 40.64 cm curvature of inhomogeneous field up to 1.3 T, followed by a collimator and a Čerenkov counter attached to a photomultiplier. With this system, Hofstadter and his team were able to measure the elastic curves of the materials and founded no clear diffraction minima nor maxima, evidence that the nuclei had no sharp boundaries. They used the exact calculations for a point charge scattering and multiplied that curve by the approximate form factor of an exponential charge distribution assumption fitted to the experimental data to obtain an estimate for the charge radius. Among other elements, the result of his calculation gave the approximate radius of $R_{Be} = 2.2$ fm and $R_{Au} = 7.95$ fm for beryllium and gold respectively [6]. Today, the acceptable values for these radii are $R_{Be} = 2.51$ fm and $R_{Au} = 5.43$ fm according to [5]. Based on these preliminary results, he continued to develop the fundamental experimental and theoretical principles that we use today for nuclear charge radius measurements.

As indicated previously, the current for the electron beam used in Hofstadter experiment was considerably small. Yet, even with such a low current, he was able to measure multiple form factor minima. The low concentration of electrons was compensated by a high number of target particles, made from solid foils with thicknesses from 0.20 mm and up to 50 mm. When considering the current in combination with the target densities, these experiments had luminosities on the order of 9×10^{29} cm⁻²s⁻¹ to 7×10^{33} cm⁻²s⁻¹. Figures 1.2 and 1.3 show the reach of these experiments, allowing to probe up to the third minimum of diffraction: the $\mathbf{q}_{i=\{1,2,3\}}$ in the figures are the momentum transfers corresponding to the first, second and third minima.

Figures 1.2 and 1.3 assumed a two-parameter Fermi charge density distribution, presented in (1.1), for which the radius parameter is taken to be R = 1.1 (fm) $\cdot A^{-3}$ for the atomic mass number A of the stable isotopes, and the surface diffuseness parameter is a = 0.57 fm for all nuclei. Note

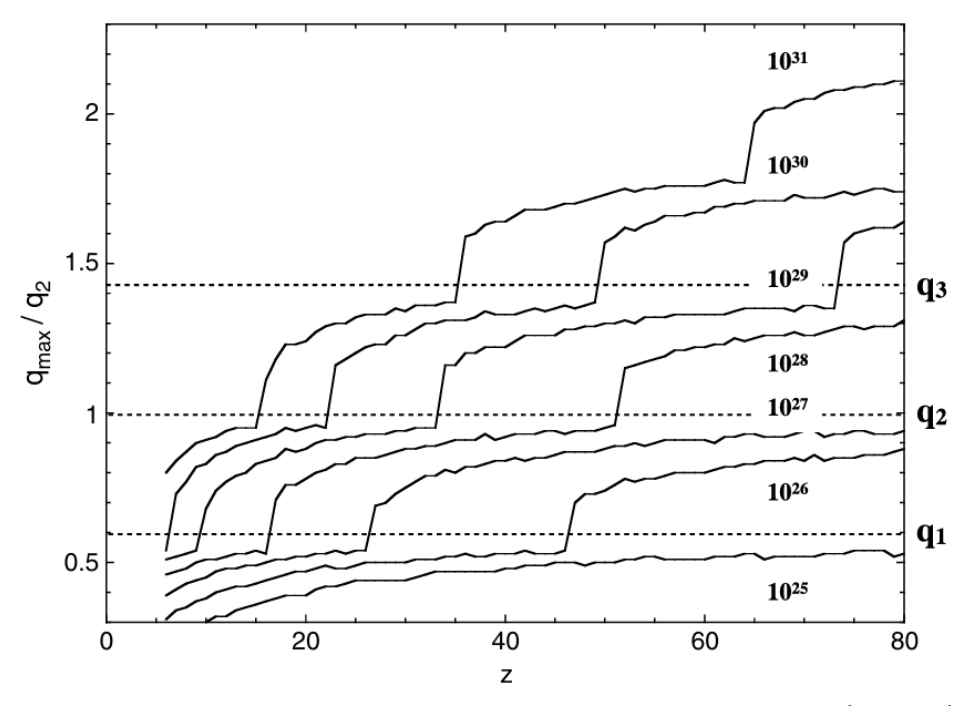


Figure 1.2 The required luminosities needed to access the 1st, 2nd and 3rd minimum of diffraction as a function of the atomic number Z [3].

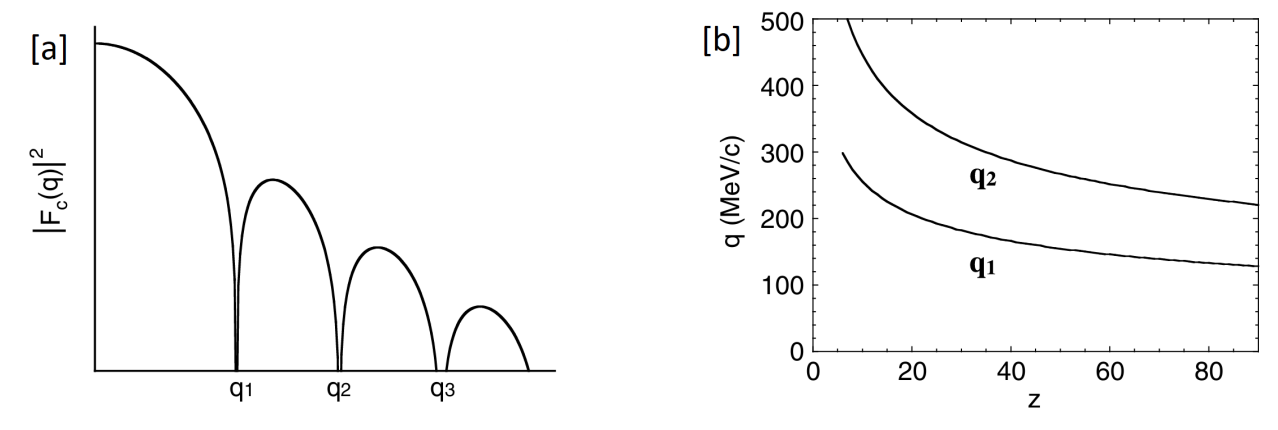


Figure 1.3 [a] The charged (Coulomb) form factor squared of the two-parameter Fermi distribution as a function of the momentum transfer q, with the minima positions labeled as q_i for i = 1, 2, 3. [b] The momentum transfer for the first and second minima as a function of the atomic number Z [3].

that ρ_0 is just a normalization constant that satisfies (1.2) for Z number of protons [3].

$$\rho(r) = \frac{\rho_0}{1 + e^{(r-R)/a}} \tag{1.1}$$

$$\int_0^\infty \rho(r) 4\pi r^2 dr = Z \tag{1.2}$$

For this type of distribution, the square form factor as a function of momentum transfer q would appear as it is shown in Figure 1.3 [a]. The positions of the three minima shown and the height of the maxima are directly correlated to the values of the radius and surface diffuseness parameters, which are then used to determine the gross nuclear charge size and shape. It is then necessary to cover a momentum transfer range beyond the first maximum, that is, approaching q_2 , in order to determine the correct shape of the nuclear charge distribution. It is clear from Figure 1.2 that in order to achieve this, one needs at least a luminosity of 10^{27} cm⁻²s⁻¹ for $Z \ge 30$ nuclei, and few orders of magnitude higher for lighter nuclei.

In the case of rare isotopes, one cannot create solid targets with particle densities in the order of 10^{21} cm⁻³. For example, FRIB can at most deliver beam bunches with 10^{13} particles, with some rare isotopes having as few as 10^3 . Let's assume that we have 10^9 ion particles confined in a cylindrical potential trap of radius 2.5 mm. From (3.4), we can calculate the required electron beam current for a luminosity around 10^{27} cm⁻²s⁻¹ to be on the order of 100 mA. This need for high current of the electron beam imposes limitations on the technologies that can be used at facilities like FRIB to conduct elastic electron scattering experiments.

1.2 Beyond stable isotopes

By coupling an electron linac to an ion beamline such as the ones here at FRIB, researchers can extend electron scattering experiments from stable nuclei to exotic-radioactive ones. Such type of innovative facilities are planned or already happening in Japan [7], Europe [8] and Russia [9]. This thesis covers preliminary investigations for the potential of integrating a compact electron linear accelerator with a beamline at FRIB to perform such scattering experiments. The research presented here focuses on the structure and feasibility of an electron acceleration system that could be coupled with FRIB's capabilities. Chapter 2 provides a review of the theory for behind the experiments of electron scattering, and provides descriptions of the theory of electron beam production, acceleration and steering. Following this, a review of different available technologies that can be used to produce and accelerate electron beams is presented in Chapter 3. This chapter also gives mention to some safety concerns that must be considered when building particle accelerators. In Chapter 4

we present the experimental measurements taken from Brookhaven National Laboratory (BNL) - Accelerator Test Facility (ATF) in conjunction with data from a simulation of the same system. From the measurements of BNL's system, beam transverse profile images, the radius of the beam as well as its emittance were calculated and compared to the simulation. Finally, a brief summary and future steps are given in Chapter 5.

CHAPTER 2

THEORY

2.1 Electron elastic scattering

In the intricate world of nuclear and particle physics, the study of electron interactions has remain a central component for unraveling the mysteries of matter at its most fundamental level. Electron scattering, a phenomenon where electrons deviate from their path due to the influence of forces from a target, is particularly crucial for understanding the underlying structures and properties of atoms. Among various types, electron elastic scattering, where the total kinetic energy is conserved post-interaction, provides insights into the atomic and nuclear structure. In this section, we will explore the mechanisms of electron elastic scattering, specifically its theoretical foundations.

2.1.1 Overview of the scattering processes

In a scattering experiment, the object of study is referred to as the target, and it is probed by an accelerated beam of particles with well defined properties. In Figure 2.1 we show the different types of scatterings, where "a" is the incoming probe particle and "b" is the target particle. These interactions are broadly classified into elastic or inelastic processes, with the primary distinction between the two lying in the conservation of kinetic energy.

- Elastic scattering is a process wherein the total kinetic energy of the particles involved is conserved. In this type of scattering, particles collide and deviate from their path, but their total kinetic energy before and after the collision remains unchanged.
- In contrast, inelastic scattering involves a change in the kinetic energy of the interacting particles. In these interactions, part of the original kinetic energy is transformed into another form, such as excited states, heat, mass, vibrations or light, resulting in a loss of kinetic energy in the system.
- Also depicted in Figure 2.1 are colliding beam reactions. This reaction scheme could be either elastic or inelastic depending on the conservation of the total kinetic energy of the

system, but it involves a special type of configuration where both the target and the probing particles are accelerated [10].

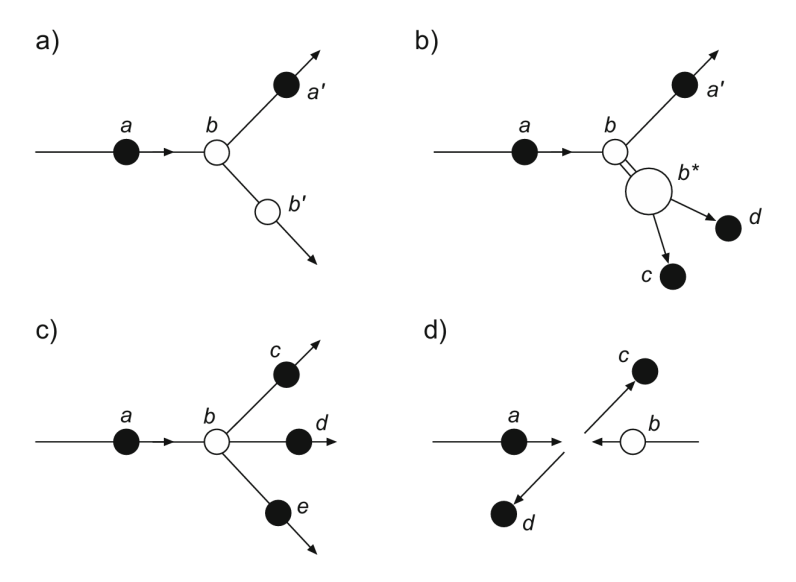


Figure 2.1 The various type of scattering processes: (a) elastic scattering; (b) inelastic scattering (production of an excited state which then decays into two particles); (c) inelastic scattering (direct production of new particles); (d) reaction of colliding beams [10].

2.1.2 Elastic scattering and nuclear charge radii

For the remainder of our discussion, we will focus on the traditional set-up from Figure 2.2, with a fixed target and an incoming probing electron beam. We want to use electrons because their DeBroglie wavelength, when accelerated to a momentum of $p \ge 100$ MeV/c, corresponds to roughly the size of the nucleus, $\lambda \le 10$ fm. Electron elastic scattering studies for the study of nuclear charge radius typically span the energy window of $100 \le p \le 1000$ MeV/c [11].

The target for scattering experiments may be solid, gas or liquid. In any case, we assume that the molecules or atoms that make up the target have a constant density of n_b , and are distributed in a volume characterized by a length l and an area A along and perpendicular to the beam's motion. We assume that the area A is equal or smaller than the beam size, such that it equals the interaction area. The incoming beam, with N_a particles per second at a velocity v_a , interacts with the target via a potential V(r). The potential changes the state of each electron's wave function from $\Psi_i = e^{ik_i \cdot \mathbf{r}}$

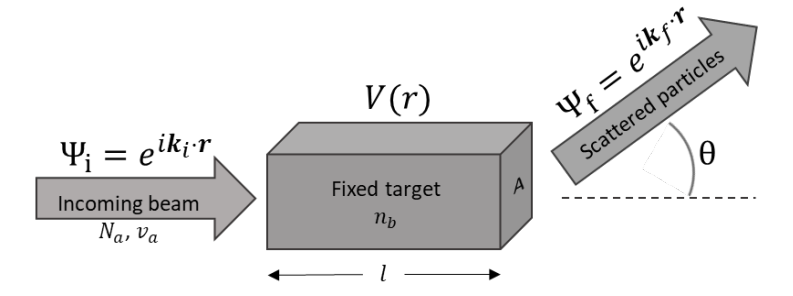


Figure 2.2 Illustration of the electron scattering arrangement.

into $\Psi_f = e^{ik_f \cdot \mathbf{r}}$, by deviating its trajectory by an angle θ . Let us assume that the only force mediating the interaction is due to the nuclear Coulomb potential of the form

$$V(r) = -\frac{Ze^2}{4\pi\epsilon_0} \int \frac{\rho_e(\mathbf{r'})}{|\mathbf{r} - \mathbf{r'}|} d^3r'$$
 (2.1)

where Z is the proton number of the target, $e = 1.6021766 \times 10^{-19}$ C is the magnitude of the elementary unit charge, $\epsilon_0 = 8.8541878 \times 10^{-12}$ F/m is the permittivity of free space, ρ_e is the electric charge distribution of the nucleus, \mathbf{r} is the location of the charge creating the potential, and \mathbf{r} is the probing location. If we assume that the nuclei have spherical symmetry, the charge density distribution can be defined as

$$\rho_e(r) = \frac{1}{2\pi^2} \int F(q) \frac{\sin(qr')}{qr} q^2 dq \tag{2.2}$$

where $q = k_i - k_f$ is the change in the electron's momentum or momentum transferred to the nucleus. F(q) is the Fourier transform of the charge density distribution, most commonly known as the form factor, and defined as

$$F(\mathbf{q}) = \int e^{i\mathbf{q}\cdot\mathbf{r}} \rho_e(\mathbf{r'}) d^3 \mathbf{r'}$$
 (2.3)

Under an ideal elastic scattering, we assume that the kinetic energy of the electron is conserved, $|\mathbf{k}_i| = |\mathbf{k}_f|$, in which case $q = \frac{2|\mathbf{k}_i|}{\hbar} \sin(\theta/2)$ [11].

In the laboratory, we measure the intensity of deflected electrons as a function of scattering angles, $I(\theta, \phi)$. We then normalize this intensity by the total number of incident electrons from the

beam, N_a , and the interaction area, A, to get the scattering probability, also known as the differential cross section $\frac{d\sigma}{d\Omega}$ where $\Omega = \int \int \sin\theta d\theta d\phi$ is the solid angle. This ratio has units of area per solid angle [12].

$$\frac{I(\theta,\phi)}{A\cdot N_a} = \frac{d\sigma}{d\Omega} \tag{2.4}$$

We can express the differential cross section in terms of the scattering amplitude, $f(\theta, \phi)$, normalized by the change in momentum

$$\frac{d\sigma}{d\Omega} = \frac{k_i - k_f}{k_i} |f(\theta, \phi)|^2$$
 (2.5)

Under the first Born approximation, the scattering amplitude is defined as

$$f_{B_1} = \langle \Psi_f | V(r) | \Psi_i \rangle = -\frac{Ze^2}{4\pi\epsilon_0} \int \frac{e^{i\mathbf{q}\cdot\mathbf{R}}}{|\mathbf{R}|} F(q) d^3 q$$
 (2.6)

for nuclei with radius **R**. In this way, we can connect the measured scattering probability to the charge density distribution contained in the form factor. In practice, ρ_e is often approximated using truncated infinite series, such as a Fourier or Bessel expansion, and the measurements are fitted to obtain approximate values for the first few coefficients in the series [11, 13].

Following Hofstadter approach, we can modulate the Mott scattering formula for a point source with the form factor such that

$$\frac{d\sigma}{d\Omega} = \left(\frac{d\sigma}{d\Omega}\right)_{\text{Mott}} |F(q)|^2 = \left(\frac{Ze^2}{4k_i^2}\right) \frac{\cos^2(\theta/2)}{\sin^4(\theta/2)} |F(q)|^2$$
 (2.7)

where k_i is the energy of the probing electrons [13]. This approximation includes effects due to the electron spin, but the recoil of the nucleus as well as magnetic interactions between nucleons and electrons have been neglected.

2.1.3 Higher order corrections to the Born approximation

In the Born approximation, where the energy transferred by the electron to the nucleus is assumed to be carried by one virtual photon, the probability for an electron to scatter off a point charge, also

known as the differential cross section, is given by the Mott scattering formula [14]

$$\left(\frac{d\sigma}{d\Omega}\right)_{\text{Mott}} = \frac{4Z^2 e^4 k^2}{q^4 c^4} \left(1 - \frac{q^2 c^2}{4k^2}\right).$$
(2.8)

For energies higher than 100 MeV we can neglect the electron mass and the Mott scattering formula can be expressed as (with $k_i = k$)

$$\left(\frac{d\sigma}{d\Omega}\right)_{\text{Mott}} = \frac{Z^2 e^4}{4k^2} \frac{\cos^2(\theta/2)}{\sin^4(\theta/2)}$$
(2.9)

as used in the previous section.

The condition for validity of the Born approximation is given by $Z\alpha \ll 1$, where $\alpha \simeq 1/137$ is the dimensionless fine structure constant. For heavier nuclei, one must multiply the Mott scattering by the form factor to accurately represent the extended shape of the nucleus.

The Born approximation can be corrected for radiative effects, straggling and dispersive effects that occur during the scattering interaction process. The first two account for the emission of real and virtual photons, while the latter accounts for only virtual photons. Note that the photons emitted through radiation or straggling must be of very low energies, or else the event wouldn't be accounted as an elastic event (they will be out of the detector acceptance) [14].

- Radiative corrections: This effect accounts for the emission of real and virtual photons
 while the electron gets accelerated or decelerated during its interaction with the nucleus'
 electric field.
- **Straggling correction**: This effect considers the possibility that the electron undergoes multiple small-angle scatterings within the target nucleus. It is dependent on the electron beam energy, and the atomic number and thickness of the target.
- **Dispersive corrections**: This correction accounts for the reduction of the multi-body problem between the incoming electron with the nucleus into the simplified one-body problem of an electron interacting with a static field. It involves an expansion of the Hamiltonian of the system.

The reader is referred to references [14, 15, 16, 17] for more information about these corrections to the Born approximation.

2.2 Beam dynamics

Particle accelerator systems use the electromagnetic force to accelerate, focus and guide the beam. The force felt by electrically charged particles with a velocity \mathbf{v} and charge q when moving through a magnetic field \mathbf{B} , and an electric field \mathbf{E} is called the Lorentz Force (2.10). The energy gain of the particle as it crosses the volume with the fields is obtained from (2.11). Although the magnetic field does not contribute in the acceleration of the particle, it plays a vital role in focusing, steering and bending particles, as will be explained later in this chapter.

$$\mathbf{F} = q(\mathbf{v} \times \mathbf{B} + \mathbf{E}) \tag{2.10}$$

$$\Delta E_{\text{gain}} = \int_{\mathbf{r}_1}^{\mathbf{r}_2} \mathbf{F} \cdot d\mathbf{r} = q \int_{\mathbf{r}_1}^{\mathbf{r}_2} \mathbf{E} \cdot d\mathbf{r}$$
 (2.11)

In the following sections, we will take a closer look at the theory behind electron beam emission and manipulation. We will first explore the theory for photoemission and thermal emission of electrons, which are the two main processes used for electron beam production. Then, we will explain how magnetic fields are used to bend and focus a beam using a simplified model of the system. Finally, a brief explanation of how Direct Current (DC) and Radio Frequency (RF) acceleration works will be given, including the "phasing" (proper alignment of the time at which the beam enters the RF cavity) and its importance when designing an acceleration system.

2.2.1 Electron beam emission

The two most common processes used to generate an electron beam are photoemission and thermionic emission. In the photoemission process, powerful laser sources are shone onto a cathode surface, exciting the electrons in the material with sufficient energy to leave the surface as an applied electric field guides them to an accelerating cavity. For the thermionic emission, the source of energy for the electrons comes from heating the cathode.

2.2.1.1 Photo-cathode guns

When an electron absorbs a photon, it can be excited from a bound states in the material all the way to a free state in vacuum. This one-step model is very crude and unrealistic: it assumes that the electron's energy as well as its momentum are conserved. More widely known is the three-step model, which breaks the emission process into: (1) photon absorption and electron excitation, (2) transport of the ejected electrons to the material surface, and (3) escape into vacuum [18].

Photon absorption and electron excitation

In the first step, we assume that all the energy levels below the Fermi energy (E_F) are filled, while all the energy states above it are empty: this approach idealizes the photocathode material as a conductor at 0 K. One also assumes that the excitation probability is exclusively dependent on the photon energy and the number of available states for electrons to move from and to (e.g., number of states below and above E_F). From the reflectivity $R(\nu)$ of the material, the probability of absorption $A(\nu)$ into the material (which is the same as the transmission) as a function of the incident light's frequency ν is

$$A(\nu) = 1 - R(\nu) \tag{2.12}$$

One would need to also know the material's absorption coefficient at $h\nu$ to determine the absorption depth, where $h=6.62607\times 10^{-34}$ J/Hz is Planck's constant. As for the number of available states, the probability of exciting the electron from an energy state E_0 to $E_0+h\nu$ is given by

$$P(E, \hbar \nu) = \frac{N(E)N(E - \hbar \nu)}{\int_{E_F}^{E_F + h\nu} N(E')N(E' - h\nu)dE'}$$
(2.13)

in which we assumed that the momentum is not conserved and thus the probability of transition is exclusively dependent on the material's electronic density of states. N(E) is the number of states for the energy $E = E_0 + h\nu$, while the integral accounts for the total number of possible transitions.

Transport of the ejected electrons

After we account for the probability of excitation, we need to consider the probability of the electron to effectively reach the surface of the material. This process is significantly different for metallic and semiconductor materials. For metallic cathodes, electron-electron (e-e) scatterings are the primordial energy loss processes that inhibit the electron from reaching the surface. On the other hand, e-e scattering are forbidden in semiconductors when the photon's energy is less than double the band gap energy (as is the case for most applications). Thus, electron-phonon (e-p) scatterings is the mechanism that dominates. It is important to mention that one single e-e scattering can reduce the energy of the involved electrons sufficiently for these to be lost, while e-p scatterings mostly affect the electron's momentum, such that an electron can undergo multiple scattering events and still retain sufficient energy to escape.

For metals, we can assume that the probability S(E) of an excited electron with energy $E > E_F$ to interact with another electron of energy $E < E_F$ is purely proportional to the number of electrons with energy E_0 , $N(E_0)$, and the number of empty states $N(E_0 + \Delta E)$ and $N(E - \Delta E)$. S(E) is then defined as in (2.14), and we can obtain the scattering length $\lambda_e(E)$ from (2.15), where λ_0 is an empirical constant of proportionality.

$$S(E) \propto \int_{2E_F - E}^{E_F} \int_{E_F - E_0}^{E - E_F} N(E_0) N(E - \Delta E) N(E_0 + \Delta E) d(\Delta E)$$
 (2.14)

$$\lambda_{e}(E) = \frac{\lambda_{0}\sqrt{E - E_{f}}}{\int_{2E_{F} - E}^{E_{F}} \int_{E_{F} - E_{0}}^{E - E_{F}} N(E_{0})N(E - \Delta E)N(E_{0} + \Delta E)d(\Delta E)}$$
(2.15)

Then, the probability that an electron created at a depth d will reach the surface is given by (2.16). From this probability, and knowing that the absorption length λ_{ph} is determined by the imaginary part of the index of refraction $n = \eta + ik$ and the incident photon's wavelength λ as in (2.17), we can integrate over all the possible depths of absorption d and get the fraction of electrons reaching the surface without scattering from (2.18).

$$P = e^{-\frac{d}{\lambda_e}} \tag{2.16}$$

$$\lambda_{ph} = \frac{\lambda}{4\pi k} \tag{2.17}$$

$$T(E, \nu) = \frac{\lambda_e(E)/\lambda_{ph}(\nu)}{1 + \lambda_e(E)/\lambda_{ph}(\nu)}$$
(2.18)

The multiple scattering events that can happen in the case of a semiconductor make the derivation of an analytical expression practically impossible. For this reason, computational methods, such as Monte Carlo techniques, are commonly employed to simulate the movement of electrons towards the surface in semiconductors.

Escape into vacuum

The final step requires the perpendicular component of the excited electron's momentum, k_{\perp} , to satisfy the inequality depicted in (2.19), where Φ is the work function energy. Note that it is not only necessary that the electron's energy surpasses the work function, but it's direction of motion must also be close to perpendicular with the surface.

$$\frac{\hbar^2 k_\perp^2}{2m} \ge \Phi \tag{2.19}$$

During experiments, photocathode electron guns undergo an "activation" process before extraction. In the process, the laser is directed at the cathode while some gas is allowed to circulate inside the chamber. The circulating gas particles attach to the cathode and form a negative affinity layer that reduces the effective work function and allows electrons to escape more easily, thus increasing the Quantum Efficiency (QE).

More details about the three-step model, and modification to this theoretical framework, can be found in [19]. In terms of losses, the first step accounts for the loss due to reflection of the incident light, while the second step reflects on the losses due to scattering processes. The final step accounts for the loss of electrons for which the direction of motion wasn't at the right angle with the surface. In general, semiconductors yield higher QE due to their band gap. This gap doesn't allow electrons to be excited into states that lack sufficient energy to escape, and additionally it prohibits e-e scatterings. As a result, the mean free path of electrons in metals is much smaller than

the laser penetration depth, resulting in unproductive absorption that will never leave the material, while for semiconductors the mean free path can even be larger than the laser penetration, thus fundamentally all excited electrons could potentially be extracted [18].

2.2.1.2 Thermionic guns

Photoemission is not the only source available to produce electron beams: thermionic emission has also proven to be capable of delivering high average current beams with relatively small radial sizes. This type of emission is described by the Richardson-Laue-Dushman equation (2.20) for a temperature T. For this equation, k_B is the Boltzmann constant, and m and e are the mass and elementary charge of the electron, respectively. This equation provides the current density J_{RLD} emitted from the cathode. Note that the work function W can be calculated from (2.21) and relates the electric potential $e\Phi$ with the Fermi level E_F [20].

$$|\mathbf{J}_{RLD}| = \frac{em}{2\pi^2 \hbar^3} (k_B T)^2 e^{-W/(k_B T)}$$
(2.20)

$$W = e\Phi - E_F \tag{2.21}$$

2.2.2 Beam focusing and bending

The nominal trajectory in accelerator science is along the path of an ideal particle, perfectly aligned with the center of every instrument in the system. In real life, accelerator systems deal with bunches of particles, not individual ones, and none of these particles perfectly follows the nominal trajectory. To prevent particles from continuously steering away and being lost inside the cavities' wall, focusing elements are strategically placed to correct for angular divergence and place such particles closer to the nominal path. Although it is common practice to use magnetic fields to manipulate the trajectory of the beam (specially at high energies), the electric force could and is also utilized at low energies. In this section, we will look in detail at the physics of the focusing process with magnetic fields only.

Let us define a Cartesian coordinate system K = (x, y, s) whose origin moves with the center of

the beam, thus, the nominal trajectory. The beam motion is aligned with the s axis, while the x axis points in the horizontal direction and y in the vertical direction. In the areas where a magnetic field bends the beam's direction, the coordinate system K must be adjusted for it. We will assume that this bending occurs exclusively in the horizontal direction, thus rotations are limited to the y-axis.

Giving a rotation by an angle φ , the axes x and s are transformed into the axes x_0 and s_0 as (2.22), or in differential form by (2.23).

$$x_0 = x \cos \varphi + s \sin \varphi,$$

$$s_0 = -x \sin \varphi + s \cos \varphi$$
(2.22)

$$\frac{d\mathbf{x}_0}{d\varphi} = \mathbf{s}_0 \qquad , \qquad \frac{d\mathbf{s}_0}{d\varphi} = -\mathbf{x}_0 \tag{2.23}$$

An infinitesimal length of the particles' path is described as $ds = Rd\varphi$ for a radius of curvature R, and it follows that the curved trajectory is

$$\frac{d\varphi}{dt} = \frac{1}{R} \frac{ds}{dt} \tag{2.24}$$

Since there is a unique correspondence between the path length s and time t, one can replace time derivatives by the corresponding derivative with respect to the s spatial coordinate as

$$\dot{x} = \frac{dx}{ds}\frac{ds}{dt} = x'\dot{s},\tag{2.25}$$

$$\ddot{x} = \frac{d(x')}{dt}\dot{s} + x'\frac{d\dot{s}}{dt} = x''\dot{s}^2 + x'\ddot{s}.$$
 (2.26)

Then, for some particle with coordinates

$$\mathbf{r} = s\mathbf{s}_0 + x\mathbf{x}_0 + y\mathbf{y}_0 \tag{2.27}$$

and mass m under the influence of the magnetic force $\mathbf{B} = B_x \hat{x} + B_y \hat{y}$, such that

$$\ddot{r} = -\frac{e}{m}(\dot{r} \times B), \tag{2.28}$$

it follows that

$$\ddot{r} = \frac{e}{m} \begin{cases} -\left(1 + \frac{x}{R}\right) \dot{s} B_y \\ \left(1 + \frac{x}{R}\right) \dot{s} B_x \\ x' \dot{s} B_y - y' \dot{s} B_x \end{cases}$$
 (2.29)

We can assume that the effects on the longitudinal component, s, are negligible since the particles are moving a relativistic velocities, and we can focus our discussion only on the transverse components. In addition, we can assume that $\ddot{s} \approx 0$ such that the forward velocity of the particles remains virtually unchanged as it transverse the region with magnetic fields. Let the momentum be defined as p = mv where $v = \dot{s}(1 + x/R)$, it can be shown that the equations of motion for this particle are

$$x'' - \left(1 + \frac{x}{R}\right)\frac{1}{R} = -\frac{ve}{\dot{s}p}B_y\left(1 + \frac{x}{R}\right)$$
$$y'' = \frac{ve}{\dot{s}p}B_x\left(1 + \frac{x}{R}\right)$$
 (2.30)

Since the dimensions of the beam are relatively small compared to the radius of curvature, $x, y, s \ll R$, we can expand the magnetic field in the vicinity of the nominal trajectory as

$$\mathbf{B}(x,y) = \left[B_{y0}\hat{x} + B_{x0}\hat{y} \right] + \left[\frac{dB_y}{dx} x \hat{x} + \frac{dB_x}{dy} y \hat{y} \right] + \frac{1}{2!} \left[\frac{d^2 B_y}{dx^2} x^2 \hat{x} + \frac{d^2 B_x}{dy^2} y^2 \hat{y} \right]
+ \frac{1}{3!} \left[\frac{d^3 B_y}{dx^3} x^3 \hat{x} + \frac{d^3 B_x}{dy^3} y^3 \hat{y} \right] + \dots
\frac{e}{p} \mathbf{B}(x,y) = \left[\frac{1}{R_x} \hat{x} + \frac{1}{R_y} \hat{y} \right] + \left[k_x x \hat{x} + k_y y \hat{y} \right] + \frac{1}{2!} \left[m_x x^2 \hat{x} + m_y y^2 \hat{y} \right] + \frac{1}{3!} \left[o_x x^3 \hat{x} + o_y y^3 \hat{y} \right] + \dots$$
(2.31)

Note that the brackets, in order from left to right, represent the dipole field through bending radius R, the quadrupole field with quadrupole strength k, and the sextupole and octupole fields with strengths m and o respectively. The two lowest multipoles are the only ones used for linear beam optics, since they are either constant and used for steering (dipole) or linear and used for focusing/defocusing (quadrupole). Normally the sextupole, octupole and higher orders of

multipoles are either used for field corrections or unwanted field errors, reason for which we will only use the dipole and quadrupole moments for this example and will assume that only horizontal dipole deflection is present.

If the momentum spread of the particles is low, as it is for typical accelerators where $\Delta p/p < 1\%$, we can rewrite the momentum as

$$\frac{1}{p} = \frac{1}{p_0} \left(1 - \frac{\Delta p}{p_0} \right). \tag{2.32}$$

If all the previous assumptions are taken we can neglect the squared terms, after which we obtain the linear equations of motion for a particle traveling through magnetic structures in accelerator:

$$x''(x) + \left(\frac{1}{R^2(x)} - k(s)\right)x(s) = \frac{1}{R(s)} \frac{\Delta p}{p}$$
$$y''(s) + k(s)y(s) = 0$$
 (2.33)

These derivations followed the explanation from [21].

2.2.3 Beam acceleration

2.2.3.1 Basic overview

There are two main common methods to accelerate a charged particle: with a static electric field (E-field) or with alternating RF electric fields, the most intuitive and simple of the two being the former. The E-field is produced by a high voltage DC supply and the beam travels between two or more electrodes with increasing voltage. After the beam exits the static field region, it usually continues its trajectory in a field-free drift tube with constant energy until it hits a target. This method imposes a limitation on the particle's energy based upon the maximum achievable voltage, that is primarily limited by corona discharge. The electrons and ions near the high voltage electrode are released with sufficient energy to cause an avalanche when they interact with the residual gas, and thus lead to a breakdown. Up to a few MeV are normally achievable; yet, the technology is still useful for some applications that do not require high energy.

For nuclear physics and particle accelerator facilities, the customary type of acceleration used today is based on alternating electric fields produced from an RF source. Via this method, the

particles travel along a cavity with high-frequency alternating voltage of the form displayed in (2.34) and illustrated in Figure 2.3: the particles gain energy when crossing the electric field, then drift through a field-free space while the field switches polarity, such that they enter the next region when the electric field is again aligned to the direction of acceleration of the beam leading to further increase in its energy [21].

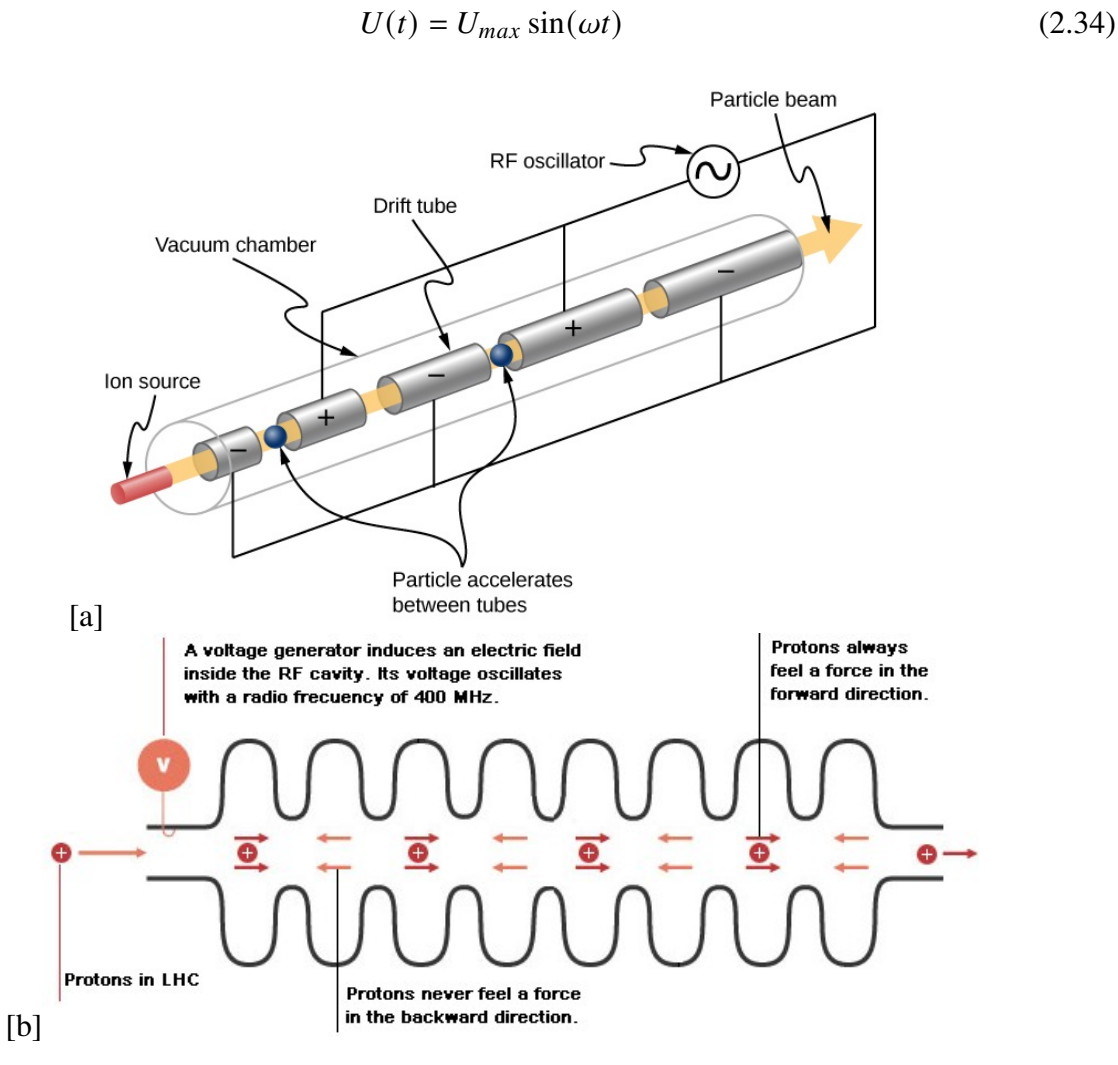


Figure 2.3 Schematics for the basic principles of RF accelerating cavities for proton acceleration. [a] Design with alternating polarity drift tubes [22]. [b] Parabolic box cavity design [23].

2.2.3.2 Cavity phases

When particles exits the *i*th drift tube, their energy had increase following (2.35), where Ψ_0 is

the average phase of the RF voltage the particles perceive as they cross the applied field sections with a maximum achievable voltage U_{max} . The length of each subsequent drift tube (i) must increase in proportion to the energy gain of the particles (E_i) , that is related to their momentum (p_i) and velocity v_i through (2.36) and (2.37).

$$E_i = iq U_{max} \sin \Psi_0 \tag{2.35}$$

$$E_i = \sqrt{m_0^2 c^4 + p_i^2 c^2} (2.36)$$

$$p_i = \gamma_i m_0 v_i \tag{2.37}$$

$$\gamma_i = \frac{1}{\sqrt{1 - \beta_i^2}} \qquad , \qquad \beta_i = v_i/c \tag{2.38}$$

 γ_i is the Lorentz factor and m_0 the rest mass of the particle. We consider the period time τ_{RF} as the time it takes the alternating field to complete a full cycle as

$$\tau_{RF} = \frac{\lambda_{RF}}{c} \tag{2.39}$$

Therefore, the necessary length for a drift tube, such that the particles arrive at the region with the electric field at its peak, must satisfy (2.40) for the non-relativistic case ($E_i = \frac{1}{2}mv_i^2$) or (2.41) for the relativistic case (see (2.36)) [21]. Note that in the case of electron beams ($m_0 = 0.511$ MeV) their velocity approaches the speed of light with just few MeV and the length of the tubes remains constant.

$$l_i^{NR} = \frac{1}{v_{RF}} \sqrt{\frac{iqU_{max}sin\Psi_0}{2m}}$$
 (2.40)

$$l_i^R = \frac{\tau_{RF}}{2} \frac{\sqrt{i(qU_{max}\sin\Psi_0)^2 - im_0^2 c^4}}{\gamma m_0}$$
 (2.41)

In accelerator systems, it is not uncommon to have multiple accelerating sections. Consequently, particles are often found to acquire energies off-peak U_{max} , and thus becoming out of phase relative to the RF voltage. In other words, if the cavities are designed for particles to arrive at exactly the maximum power of the voltage, the beam would become unstable and be lost. Instead of using $\Psi_0 = \pi/2$ at the peak voltage U_{max} , some positive degree below Ψ_0 is used at $U_{eff} < U_{max}$. The optimal phase should be around 30° or $\pi/6$, with the exact value depending on the real structure. A visual concept of this optimal phasing is provided in Figure 2.4.

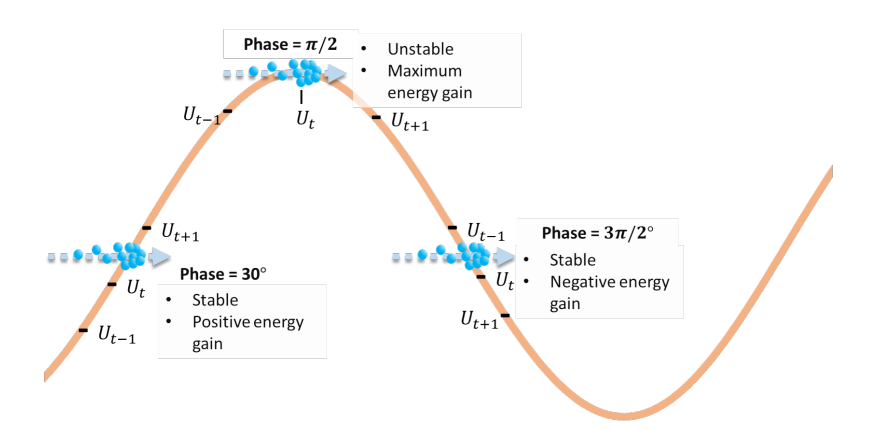


Figure 2.4 Visual representation for the needed phase focusing between the beam and the RF voltage. Beam stability is achieved for phases around $\pi/6$ and $3\pi/2$.

For a structure designed to receive an ideal particle at the nominal phase $\Psi_0 = \pi/6$ at some time t, a slightly faster particle that arrives at the time t-1 would perceive a weaker accelerating voltage $U_{t-1} < U_t$. On the other hand, a particle moving slightly slower and arriving at time t+1, would feel a voltage $U_{t+1} > U_t$ that would then accelerate it. Thus, this phase promotes a longitudinal self focusing effect. From Figure 2.4, it is clear that a design for maximal voltage amplitude is unstable as it produces the opposite effect: faster particles are still accelerated while slower particles are decelerated as they perceive the field in the opposite direction. Choosing even higher values for the phase, such as $3\pi/2$, cause deceleration of the beam [21].

CHAPTER 3

TECHNOLOGIES

3.1 Electron Gun

In this section, we will delve into the intricate details of electron injector systems and their application in high performance environments, with an emphasis on photonic guns. We will briefly discuss the thermal emittance of the beam and how it must be considered in the design, the materials most commonly used in photocathodes, as well as the challenges of operating electron guns. The chapter also presents the latest advancements in photocathode technology, including the design and performance of specific high-efficiency photocathode and thermionic guns. This chapter offers a thorough exploration of electron injectors' complexities, challenges, and the cutting-edge technological solutions developed to optimize their performance.

3.1.1 Beam Emittance, Brightness and Luminosity

An essential aspect of the injector's performance is the beam's emittance and brightness. The brightness of the beam describes its angular divergence, and it is dependant on the beam's emittance, which can be defined as the area of the ellipse in the phase space of transverse velocity as a function of position. In concrete terms, the brightness is the ratio of the beam current to the transverse emittance, as shown in (3.1.1). This important beam parameter, the emittance ϵ , is determined after extraction by the balance between betatron oscillations and damping, which ultimately depends on the magnet structure [21]. Understanding and optimizing both of these parameters is crucial for maximizing the beam's performance.

The space charge effect, the Coulomb repulsion of electrons within the beam bunch, can rapidly increase the emittance, specially so for high current guns. This can be compensated by using extraction DC voltages above 100 kV. For most high performance applications, somewhere between 400-600 kV could suffice for emittance compensation. The normalized thermal emittance of the beam, ϵ , when it comes out from the photocathode is directly proportional to the laser spot size σ_{laser} , and to the square root of the electrons' transverse energy k_BT . Since the beam's

brightness is dependant on the emittance, it is thus dependant on these parameters as well. This can be seen in (3.1) and (3.1.1) for the emittance and brightness respectively.

$$\epsilon = \sigma_{laser} \sqrt{\frac{k_B T}{mc^2}} \tag{3.1}$$

Here, m is the electron's mass and c is the speed of light. The brightness, B_n , on the other hand, is described as

$$B_n = \frac{2I}{\pi^2 \epsilon(n, x) \epsilon(n, y)}$$
 (3.2)

where I is the beam current, and $\epsilon(n, x)$ and $\epsilon(n, y)$ are the normalized emittances in the corresponding transverse planes. More importantly, the maximum transverse brightness for an electron bunch with repetition frequency f, can be described as

$$\frac{B_n}{f} = \frac{mc^2 \epsilon E_{cathode}}{2\pi k_B T} \tag{3.3}$$

where $E_{cathode}$ is the electric field at the cathode surface. Here, it is evident that finding materials with low emitting transverse thermal energy k_BT , and increasing the electric field at the cathode's surface, is essential for maximizing the obtainable beam brightness [19].

It is worth noting that the emittance of electron beams have a minimum theoretical value determined by the starting values of the beam's dispersion and the optical functions of the magnets in the structure, as described by [24], [25]. This value must be individually calculated for every system [21].

Luminosity, in the context of accelerator science, is a term that combines the characteristics of the incident beam and the target to determine the interaction rate per unit cross-section, and has units of cm⁻²s⁻¹. This is,

$$L = n_1 n_2 l \tag{3.4}$$

where n_1 is the number of particles per second in the beam, while n_2 is the particle number density of the target and l is the length of the target. Using this, we can define the rate of interactions per second as

$$\frac{dR}{dt} = \sigma L \tag{3.5}$$

where σ is the cross section for the type of interaction concerned, with units cm² [26]. We have here assumed that the target has homogeneous particle density n_2 and its cross-sectional area is larger than the incoming beam's.

3.1.2 Photoinjectors

For the application at hand, it is said that a source is DC if the duration is longer than 1 μ s. This must not be confused with Continuous Wave (CW), which denotes that for each period of an RF cycle a bunch of electrons is present [19]. It is well known that RF accelerating structures can achieve higher acceleration gradients than a DC acceleration structure due to the lower voltage breakdown threshold of the later, which allows RF accelerating systems to be more compact and energy efficient. Yet, at the initial stages of beam extraction, DC acceleration offers a simple and stable configuration that can yield lower emittance [27]. Additionally, only DC guns can be used for extraction of spin polarized electron beams, a possible upgrade for the system. For this reason, here I will discuss a hybrid system that uses a high voltage Direct Current to extract the electrons from the cathode, which are then accelerated by one or more RF acceleration cavity.

3.1.2.1 Advanced DC guns

In this section we present two advanced photocathode electron guns. The first gun, an enhanced version of a Jefferson Lab's earlier model, incorporates several upgrades to optimize its performance and reliability. These improvements include a more effective vacuum system, refined motion mechanisms for the photocathode, and a novel approach to cesium deposition for high voltage operations. Additionally, a unique shield door mechanism is introduced to protect the cathode from damage during the high voltage conditioning. The second gun, developed by Cornell, features a cryogenically cooled design with a Cs₃Sb photocathode. It was constructed primarily from stainless steel and it showcases a unique electrode configuration and a specialized insulator design. The

gun's baking and cleaning procedures, both needed to achieve an optimal vacuum environment, are described in details, and the gun's operational characteristics at various temperatures and voltages are also mentioned. Both guns could potentially be used in electron elastic scattering experiments.

Jefferson Lab's high average current gun

Figure 3.1 depict a newer model of a Cs:GaAs photocathode gun that was made based on the Thomas Jefferson National Laboratory (JLab) 1 kW Demo IR FEL gun [28]. Note that the optical set up is external, as per usual for photocathode guns, and the laser is directed onto the cathode through one of the viewing ports of the cathode chamber. In the newer model, they decreased the vacuum level, added motion mechanisms for better photocathode performance and developed a new method for depositing Cs to allowed a more reliable high voltage operation. One of the new features for photocathode handling included a swing shield door to protect the cathode from back-ion bombardment damage during high voltage conditioning. A detailed schematic inside the ball cathode, that shows the shielding, is presented in Figure 3.2. This gun demonstrated up to 9.1 mA CW beam for a 122 pC bunch with 75 MHz repetition rate [29].

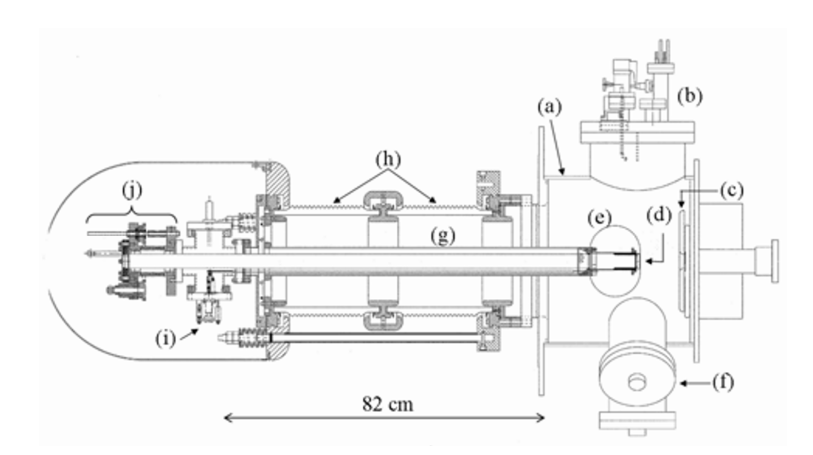


Figure 3.1 DC photocathode gun schematic. (a) vacuum chamber, (b) instrumentation, (c) anode, (d) photocathode, (e) ball cathode, (f) NEG pumps, (g) ball support tube, (h) ceramics, (i) shield door actuator mechanism, and (j) stalk retracting mechanism [29].

The exposed area of the photocathode has a diameter of 2.54 cm, much greater than the laser spot of 0.8 cm diameter, and it is illuminated off center to reduce QE degradation through back-ion

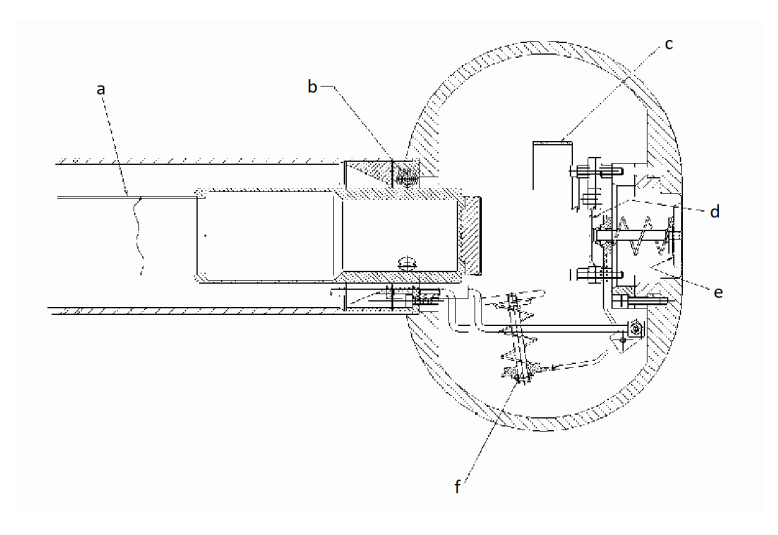


Figure 3.2 Detail of the inside of the ball cathode with the stalk retracted. The shield door is closed only during high voltage conditioning. (a) Stalk retracted, (b) roller guide unit for stalk end - sapphire rollers, (c) charge collector, (d) cesium channels, (e) cathode shield closed, and (f) cathode shield retracted [29].

bombardment. The cathode is a single crystal GaAs Zn-doped wafer, mounted on a molybdenum disk brazed to one end of the stalk. Before use, the cathode goes through a hydrogen and heat cleaning cycle, followed by baking of the full system, a high voltage conditioning, and finally the photocathode activation to increase QE. The equipment was baked at 500 C for 45 minutes, followed by a longer baking at 250 C until there was no significant vacuum improvement. The electrodes were conditioned to 420 kV, with the stalk retracted and the shield door closed, for about 80 hours to reliably operate at 350 kV. They followed a standard cesium-oxygen activation procedure, as described in [30]. They tested two exact wafers, from the first one a total of 1300 Coulombs were extracted, 100 Coulombs per re-cesiation and 5% QE. With improvements in the vacuum condition and reduction in the beam halo (they installed more pumps and anodized the outermost part of the photocathode), they increased the extracted charge from the second wafer to 500 C per re-cesiation and 7% QE [29].

Cornell's cryo-cooled gun

Another model for high average current electron gun was recently developed by Cornell. It is a high voltage cryogenically cooled photoemission gun with Cs₃Sb photocathode. The gun walls were made out of stainless steel, and pure helium gas was used during high voltage conditioning.

The system allows for back-illumination of the photocathode, although only standard forward reflecting illumination has been tested. The gun uses two main electrodes, a screening electrode and a spherical shell one. The first one consist of a thin tube that shields against high field emissions at the triple junction of the insulator, High Voltage (HV) stalk and the vacuum, and prevents thermal conduction from the insulator to the cryogenic electrode. The later spherical electrode is made of two joined hemispheres of 316SST vacuum remelt with an internal copper electrode structure, and is where the photocathode is located. The system also has a grounded flat mesh anode to create a uniform electric field in the gap between the cathode and the anode, it is a 0.01 cm wire with 22 lines per cm, and it is located 2 cm away from the cathode and parallel to the flat surface of the spherical electrode. This grid has two holes, one allows the laser beam to reach the cathode, and the other allow the extracted electrons to fly out. They used an inverted insulator made of AL_2O_3 ceramic with a measured resistance of $16~G\Omega$ [31]. Diagrams and pictures of the system are displayed in figures 3.3 and 3.4.

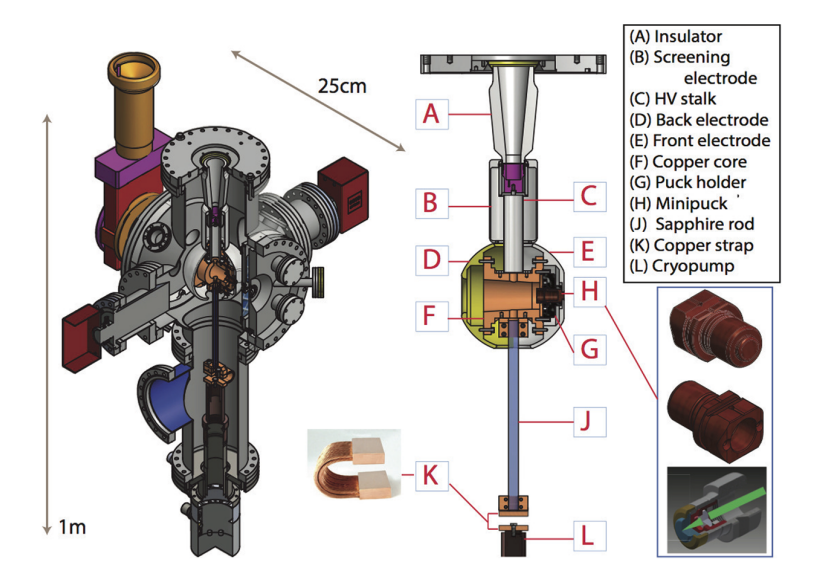


Figure 3.3 Left: A 3D model of the gun. Right: The internal structure of the gun. The two different types of substrate holders (H) are shown. The standard puck (top), is the INFN/DESY/LBNL type used in the FLASHX-FEL gun and on the APEX photoinjector. The modified transmission puck (bottom), was designed and realized to allow the operation of the photocathode in the transmission mode [31].

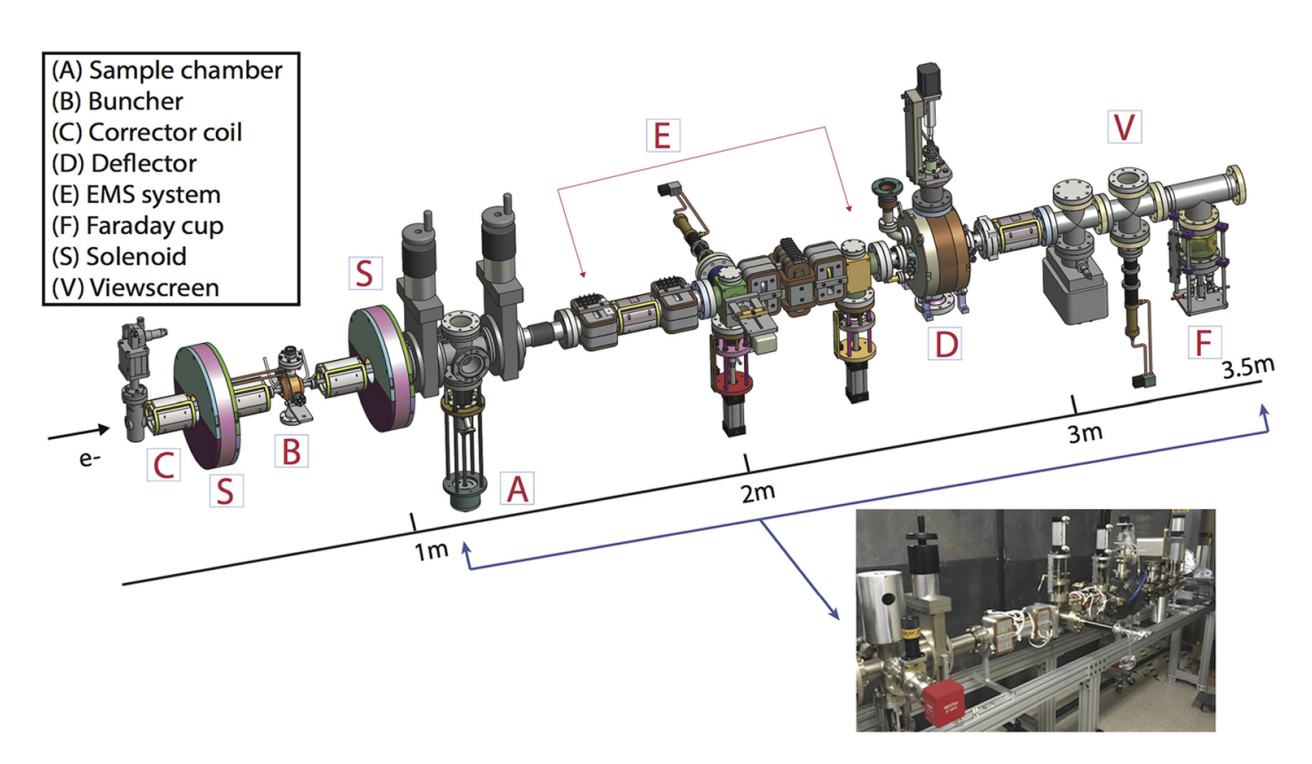


Figure 3.4 3D model of the beamline of the Cornell Cryogenic DC gun. The electron beam enters from the left as indicated by the arrow. The inset shows a picture of the pre-assembled beamline [31].

To achieve a static vacuum pressure of 2×10^{-11} Torr, they baked chambers and fittings individually in air at 400 °C for 5 days, then thoroughly cleaned the components, and carried out a final bakeout, after assembly, at 120 °C for three days. The electrodes were polished with different materials, the finest being diamond suspension of 0.25 μ m for the electrode. The HV conditioning was carried out both at room temperature and after the gun was cryogenically cooled down. During room temperature conditioning, highly pure He was introduce into the gun vessel until vacuum was raised above 10^{-5} Torr with ion pumps off, while the voltage of the gun was increased up to ~ 270 kV. The He gas was introduced periodically. Because the introduction of He gas would significantly increase the temperature at the gun, no gas was introduced during the cryogenic conditioning where ~ 300 kV was reached. They set up automatic limits to shut off the HV power supply in order to avoid major voltage breakdowns. The triggers included: four radiation monitors with threshold at 2 mR/h, vacuum level larger than 10^{-8} Torr in the gun vessel, and excess current larger than $300~\mu$ A from the supply controller. The temperature for the cathode

was 43 ± 1 K in the first sample, and 39 ± 1 K after replacing the photocathode puck with a polished one. The cooling took 22 to 30 h, with the time required to reach thermal equilibrium steadily increasing [31].

The cathode is grown and transported under vacuum, avoiding possible contamination from air exposure. It was shine with 500 nm wavelength laser at 78 MHz repetition rate and 0.5 mW power, to produce 0.1 pC bunches with 10μ A average current and 5% QE. At room temperature, the gun was operated at 230 kV, corresponding to 11.5 MV/m extraction electric fields, and had a beam root mean square (rms) of $\sigma_x = 1.31 \pm 0.07$ mm and $\sigma_y = 1.03 \pm 0.07$ mm. At 43 K, the gun was operated at 190 kV, corresponding to 9.5 MV/m extraction electric fields, and had a beam rms of $\sigma_x = 1.23 \pm 0.07$ mm, $\sigma_y = 1.10 \pm 0.07$ mm [31].

3.1.2.2 Considerations and Challenges

As of today, semiconductors such as GaAs (the only known cathode that can generate spin polarized electrons), Cs₂Te, GaN, and K₂CsSb, are the most commonly used materials with highest QE and lowest emittance used for photo-production of electron beams. Particularly, QE of up to 20% have been measured for GaAs and K₂CsSb using 520 nm light [19]. High power lasers for this particular wavelength have been commercially available for a long time, with multiple sources offering systems at reasonable prices and high performance [32],[33],[34]. The same cannot be said for Cs₂Te and GaN, which require Ultra Violet (UV) light, a spectrum for which no laser system has yet been able to produce enough average power. It is important to notice that even for these materials there is a trade off between QE and thermal emittance [19]. GaAs has demonstrated to be the semiconductor with the lowest thermal emittance [35]. Unfortunately, this minimum happens near it's band gap, as shown in Figure 3.5, where the QE also reaches a minimum lower than 1%.

After deciding the material with which the cathode will be made of, one must caution against the production of "accidental" electrons from scattered light hitting the cathode outside the desired spot. This has become one of the greatest factors limiting the lifetime of cathodes, as these electrons scatter around the chamber producing more electrons, light and ultimately degrading the vacuum conditions. GaAs is one of the most sensible material, requiring vacuum levels under 1×10^{-9} Pa for

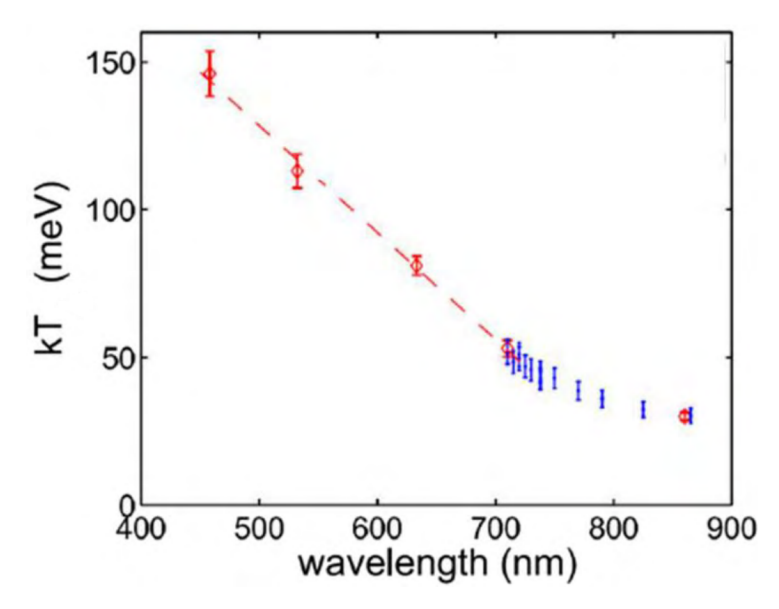


Figure 3.5 Transverse thermal energy for the electrons photoemitted from GaAs as a function of wavelength. The red points were measured using multiple laser spot sizes while the blue points were measured using a single spot size. The dashed line shows a fit over the linear region. kT is the electron's effective transverse energy normal to the cathode's surface [19].

successful operations. A solution to this problem is to inactivate the outer area of the cathode. This has been done by coating the cathode with an oxide layer, or masking the surface while activating with cesium [36]. Other mechanisms that limit the lifetime of the cathode are chemical poisoning and ion back-bombardment. These problems can be overcome by the same coating method of the cathode surface. Although this coating could potentially lower the QE, the use of such coating has been demonstrated to deliver higher total currents over the lifetime of the cathode [37]. Improving the vacuum level could significantly extend its lifetime as well.

One of the main sources of vacuum contamination comes directly from the walls of the system, a process known as outgassing. To reduce the hydrogen outgassing, systems are baked at 150 °C for at least 24 hours. The pieces are baked at even higher temperatures and for longer periods of time before assembly. Another way to minimize contamination in the system is to clean each part with high pressure (5×10^5 to 7×10^6 Pa) ultra pure de-ionized water or gas (nitrogen or dry-air) and allowing it to dry in a clean room [19]. A normal spectrum for residual gas found inside a photoinjector system after baking is found in Figure 3.6.

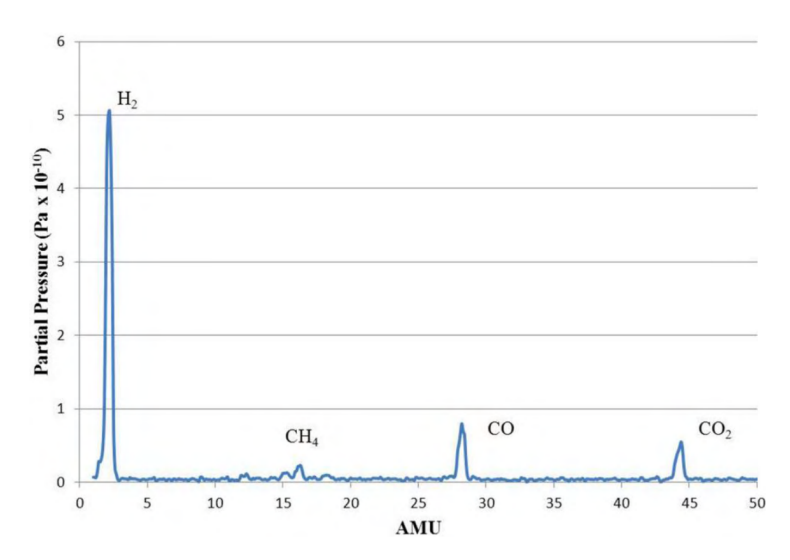


Figure 3.6 Residual gas spectrum after bake-out and non-evaporable getter pump activation, showing hydrogen, methane, carbon monoxide and carbon dioxide. The total measured pressure was 6×10^{-10} Pa [19].

Given the constant high voltages during the operation of electron guns, voltage breakdowns can become a significant problem. In the earlier years of photoemission, cesium activation (needed to increase the quantum efficiency) was performed in the same chamber where the experimental extraction was carried on. This contaminant made breakdowns more likely, as it lowers the work function of the electrodes as much as it lowers the cathodes'. Thus, more recent systems include a dedicated-isolated vacuum cavity for the purpose of activation, and from there the cathode is taken into the experimental area by means of a load-lock. Additionally, guns are processed to 10-20% above the operating value, in some cases up to 750 kV maximum voltage, to reduce field emission and arcing.

Another factor that influences the beam's emittance and the behavior of trapped contaminants are stray magnet fields from the system's walls. To minimize these, stainless steel is preferred for vacuum chambers and flanges. Other materials may be used as well, such as molybdenum, copper, or other pure metals with low outgassing rates. For cathodes and anodes, experiments suggest that the best materials are niobium, stainless steel, or molybdenum for the former, and titanium or beryllium for the later.

It is worth noting that using turbo pumps or cryopumps is advice against, since the vibration

caused by these can cause disturbances in the beam during extraction. Instead, ion pumps together with getter pump strips are more suitable for photoemission guns. Every component of the system, buncher, RF cavities, load-lock, or any other, must be maintained under the same vacuum condition as the gun chamber to avoid contamination [19].

The development and optimization of photocathodes for electron beam production have made significant strides, particularly with semiconductors like GaAs and alkali antimonides. These materials, offering high quantum efficiency and low emittance, are central to advancing the field of electron injection technology. The balance between quantum efficiency and thermal emittance remains a key area of research, especially in the context of their operational environments and the challenges posed by factors like vacuum contamination and voltage breakdowns. Innovations in cathode design and system maintenance, such as specialized coatings and vacuum techniques, continue to play a critical role in enhancing the performance and longevity of these vital components in electron guns.

3.1.3 Thermionic gun

Another alternative for the electron injection are thermionic guns. These have a simpler design, can be bought from commercial sources at moderate prices, and typically have longer lifetimes than photo-guns. Furthermore, recent advancements in this technology have led to the achievement of remarkably high electron currents, enhancing their applicability in various experimental settings, including elastic scattering experiments.

One notable example of a high current thermionic gun is the Low Energy Electrons from a Thermionic Cathode at High Intensity (LEETCHI) system, designed and tested by European Council for Nuclear Research (CERN). LEETCHI is a Pierce-type gun that has the electrode of the cathode holder and the anode electrode at 30° and 45° with respect to the cathode surface. This arrangement prevents beam divergence within the accelerating gap [38]. It uses a commercial cathode assembly that includes a 10 mm radius planar thermionic emitter and two grids that serve to limit the beam current exiting the cathode. All together, it is capable of delivering a current density of 6 A/cm² [39]. The gun output current is limited by the cathode temperature and by

space-charge effects between the cathode and the first grid. During operation, the extracted beam is accelerated up to 140 keV using DC voltages, then, it is focused and measured by an Optical Transition Radiation (OTR) diagnostic. It is stated that the machine can maintain a constant emission of 5 A for pulses as long as 150 μ s, yet, all the reported optical measurements were limited to 6 μ s pulses to prevent the deterioration of the OTR. When they measured the rms radii of the beam for electron currents of 0.5 A and 5.5 A, they got minimum values of roughly 2.5 mm and 4.1 mm respectively. The normalized rms trace-space emittance was estimated using computer simulations to be between $\epsilon_{rms} = 35$ mm mrad and $\epsilon_{rms} = 70$ mm mrad. All of this was achieved with a vacuum of only 10^{-8} mbar across the full system [38]. A diagram of the beam line can be seen in Figure 3.7, together with measurements and calculations of the rms radii of the collected beam at the OTR.

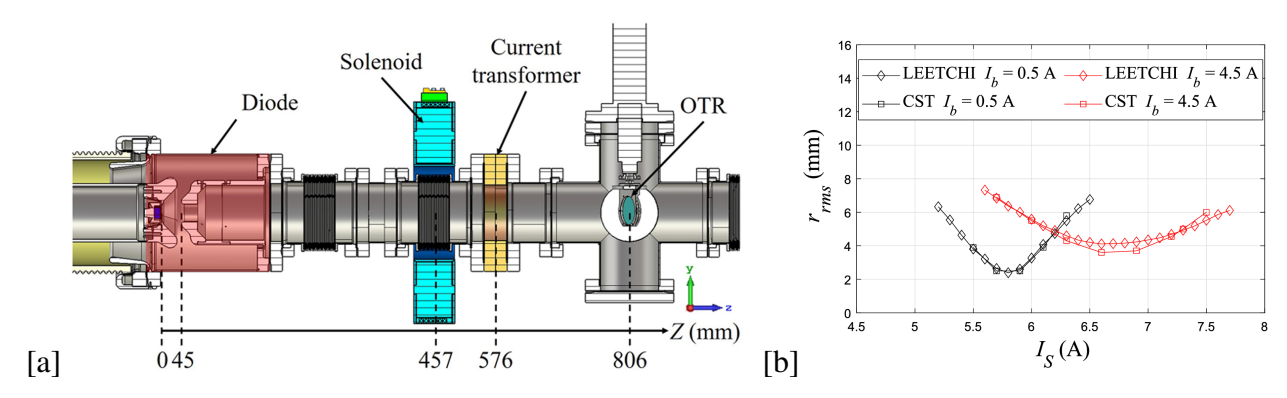


Figure 3.7 [a] Diagram of the layout for the LEETCHI system. [b] Experimental and simulated rms radii for 0.5 A (black) and 4.5 A (red) as a function of the coil current I_s , for a gap between the grid and the anode aperture of 45 mm [38].

Other systems have been made to deliver up to 100 A/cm^2 current densities over 10,000 hours of operational lifetimes, using advanced cathodes and/or high temperatures at vacuum levels between 10^{-8} to 10^{-7} Torr [40]. Some studies about this using simulations have indicated that guns equipped with cathodes made of LaB₆ can generate a 10 mA average current electron beam with 100 keV energy and normalized emittance of 40 mm mrad, at a filament temperature of 1760 K [41].

Thermionic electron guns play a pivotal role in various high-current applications, with their design and operational efficiency constantly under improvements. Although this work has mainly

focused on the use of photoguns, given the luminosity requirements and the prospect of extracting currents in the order of 1 A using thermionic guns, it is worth taking the time to consider them.

3.2 Acceleration cavities

In this section we will explore electron bunchers, give some general information about RF acceleration cavities, and provide detailed experimental results obtained from an advanced cold copper acceleration cavity. Each of these components plays a pivotal role in the intricate dance of accelerating electrons to near-light speeds. Electron bunchers, serving as the bridge between initial electron extraction and high-speed acceleration, are instrumental in grouping and preparing electrons for the RF cavities. Their ability to modulate particle velocities and densities is essential for reducing energy spread, thereby ensuring that electrons are suitably prepared for acceleration. This process is critical in maintaining the integrity and efficiency of the entire system. Moving to classical RF cavities, because of the high acceleration gradients needed for rapid energy gain, these structures need to deal with the daunting challenge of managing RF breakdowns, a phenomenon that can cause significant permanent damage. Understanding and mitigating these breakdowns are vital for the longevity and effectiveness of the system. Finally, the development of the Cryo-Cu-SLAC, a high gradient X-band cryogenic copper accelerating cavity, represents a remarkable achievement in this field. Its ability to deliver substantial accelerating gradients while maintaining a manageable breakdown rate is a testament to the ingenuity and collaborative efforts of researchers. Each component discussed in this section – from the precise bunching of electrons to the management of RF breakdowns and the groundbreaking development of the Cryo-Cu-SLAC – represents a critical piece in the complex puzzle of building an electron elastic scattering systems.

3.2.1 Electron buncher

In a typical set-up, electron accelerators consist of a DC gun injector, where electrons are extracted from the cathode, followed by a buncher, that groups the particles into longitudinal bunches and accelerate them into almost the speed of light, and finally, the bunches are accelerated to the desired energies by an RF cavity. It is not uncommon for the buncher to be coupled with the RF elements as one single accelerator assembly. Electrons that come from the gun have uniformly

distributed phases and the same energy. Unlike DC acceleration, that is not dependent on phase, once the particles enter the RF cavity, their energy gain is dependent on their phase, as given by (??). Reducing the energy spread before entering the accelerating $\beta = 1$ section is the main purpose of grouping the electrons into small phase spread bunches, separated in space by one wavelength in the waveguide [42].

The simplest bunching technique is known as "ballistic" or "klystron". It uses a stand-alone RF cavity that modulates the particles' velocities, resulting in density modulation after a drift. The cavity is physically separated from the accelerator by a drift space. Another common type of buncher use an accelerating waveguide section with constant phase velocity, which bunches the beam using phase motion. These are known as "tapered bunchers", and are very efficient since they allow for simultaneously accelerate and bunch. They provide the best capture rate and allow for specific beam parameters to be achieved, but because of their complexity, it is the most challenging design [42].

In a system from Los Alamos National Laboratory, as an example, the initial bunch length after exiting the gun is approximately 30 - 40 ps, then it is compressed to 5 - 10 ps using a normal conducting RF buncher cavity, and it is further compressed while passing through several super conducting RF cavities to achieve a bunch length of 1 - 2 ps. The system also includes several solenoid focusing magnets that control the beam size and emittance [19].

3.2.2 Considerations and challenges of RF cavities

RF breakdowns is one of the major limiting factors for higher accelerating gradients. We call an RF breakdown when the transmission and reflection power abruptly and significantly changes while emitting a burst of X-rays and visible light. The specific change of RF power for Standing Wave (SW) and Traveling Wave (TW) are different, but both cause damage to the accelerating structure, as well as the RF components and sources. In the case of TW, the transmitted power drops and up to 80% of the incident power is absorbs. On the other hand, the input RF power is reflected for SW structures [43]. Typically, RF breakdowns are separated into trigger and secondary. While the secondary breakdowns appear to be caused by the damage caused by the

trigger breakdown, the trigger breakdown is understood to be dependent on material properties and structure geometry. Some of the things that can affect the rate of breakdowns are pulsed surface heating, peak electric and magnetic fields, peak Poynting vector, hardness of the cavity material, among others. Peak RF pulsed heating is more important for SW, while RF electric peak fields matter most for TW structures [44].

When measuring the RF breakdown rates, the RF power into the structures is slowly increased. The number of breakdowns is recorded and the official breakdown rate is obtained once the rate stabilizes and remains constant for hours. Variability in the original state of the metal surface, due to different manufacturing methods and surface preparations, make the initial state of breakdowns irreproducible. The breakdown rate nonetheless can be reproduced, and it is dependant on the structure geometry and material, as well as working conditions [43].

It has been empirically found, with some theoretical models agreeing, that the breakdown rate, BDR, depends on the accelerating gradient. G, as $BDR \propto G^{30}$ for many TW structures [44]. Numerous studies have been carried out to increase the accelerating gradient while decreasing the RF breakdown rate. One study found that heat-treated structures (those that used brazing or diffusion bonding for manufacturing) result in significantly higher breakdown rates [45]. Other methods like wielding and electroforming (deposit copper onto aluminum mandrel in an electro-chemical bath and subsequently removing the aluminum by etching) have been suggested as alternatives for high gradient accelerating structures [43].

3.2.3 Cold copper acceleration cavity

SLAC National Accelerator Laboratory, in collaboration with the University of California - Los Angeles and Cornell University, have developed a high gradient X-band cryogenic copper accelerating cavity, Cryo-Cu-SLAC, that has proven to deliver up to 250 MV/m at 45 K with 10⁸ RF pulses, the highest achieved accelerating gradient with it's reported RF breakdown rate. Furthermore, this accelerating system reached the highest accelerating gradient for X-band RF structures maintaining the same breakdown rate of other structures with lesser accelerating gradient. It must be noted however that by running the machine at gradients higher than 150 MV/m considerable structural

degradation was observed, and therefore a trade-off must be made to preserve its operational lifetime [44].

Since it is currently understood that breakdowns are caused by movement of crystal defects, induced by periodic mechanical and/or thermal stress, it was theorized that cryogenic temperatures could decrease such mobility and stress, thus decreasing the total RF breakdown rate. This was the primary motivation of the group to develop the Cryo-Cu-SLAC. Reducing the cavity temperature to below 77 K decreases the RF surface resistance and coefficient of thermal expansion, and it increases the yield strength and thermal conductivity. These changes decrease the pulsed surface heating and mechanical stress experienced by the cavity. The decrease in RF surface resistance has been extensively studied, and in cryogenic copper the phenomena can be described by the theory of anomalous skin effect [46]. Unluckily, there are not many studies of copper cavities at temperatures below 100 K with high input RF power corresponding to fields greater than a few MV/m. More so, one study showed a decrease of the intrinsic quality factor, Q_0 , with increasing fields at 3 GHz, 77 K and surface electric fields of up to 300 MV/m. This study did not reported the observed breakdown rate [47].

The structure developed by SLAC, Cryo-Cu-SLAC, is made of three cells with the highest field in the middle cell, and it is shaped to mimic the properties of longer periodic structures. It has a small aperture of a=2.75 mm radius and elliptical shaped irises of 2.0 mm thickness. It was designed to be critically coupled at 96 K with $Q_0=19,100$, under-coupled at 293 K and over-coupled at 45 K, using a TM_{01} mode launcher as the RF power coupling. This cavity didn't have field probes, as they distort surface fields and degrade high power performance. Instead, they measured the input/forward RF power, reflected RF power, and signals from current monitors that intercept the field emission currents, to determine the electric field in the cavity. Its resonant frequency is 11.424 GHz at 150 K, and 11.4294 GHz at 45 K [44]. Other parameters are shown in Table 3.1.

The cavity was in contact with the head of the pulsed cryocooler Cryomech PT-415, and placed inside a vacuum cryostat. A heat shield of 0.015 inch thick copper foil was placed in between the

Parameter	293 K	45 K
Q-Value	8,590	29,000
Shunt impedance [M Ω /m]	102.891	347.39
Hmax [MA/m]	0.736	0.736
Emax [MV/m]	507.8	507.8
Eacc [MV/m]	250	250
HmaxZ0=Eacc	1.093	1.093
Losses in a cell [MW]	7.97	2.36
Peak pulsed heating (150 ns) [K]	86.9	21.9
a [mm]	2.75	2.75
$a=\lambda$	0.105	0.105
Iris thickness [mm]	2	2
Iris ellipticity	1.385	1.385

Table 3.1 Parameters of periodic accelerating structure with π phase advance per cell and dimensions of the Cryo-Cu-SLAC middle cell at 45 K and 293 K. Fields are normalized to $E_{acc} = 250$ MV/m for $f_0 = 11.424$ GHz. Peak pulsed heating is calculated for a pulse with 150 ns flat gradient [44].

SW structure and the rest of the cryostat, before the current monitor, to prevent contamination of the accelerating structure from gases of the vacuum of the cryostat. A diagram of the system can be seen in Figure 3.8. The source for the RF power was a SLAC 50 MW XL-4 klystron, with repetition rate of 5, 10, or 30 Hz and pulse length of up to 500 ns [44].

The studies with Cryo-Cu-SLAC found that lowering temperatures allowed to sustain larger RF surface electric fields with decreased probability for breakdowns. Still, Q_0 decreased with increase in the accelerating gradient due to dark current beam loading. The processing history of the cavity for high power measurements, recordings of the acceleration gradient and breakdown accumulation as a function of pulses, is presented in Figure 3.9. For the accelerating gradient after 70×10^6 pulses, they measured an RF trigger breakdown rate of 2×10^{-4} /pulse/m and a total breakdown rate of 2×10^{-3} /pulse/m for a shaped pulse with 250 MV/m, corresponding to 507 MV/m peak surface electric field, and 150 ns flat gradient. These rates were measured for periods of 1-3 million pulses where the gradient and rate of trigger breakdowns were relatively constant [44]. We can see how the breakdown rates for the Cryo-Cu-SLAC compares with measurements of other equivalent shape (2.75 mm aperture radius) accelerating structures of different materials at room temperatures is presented in Figure 3.10.

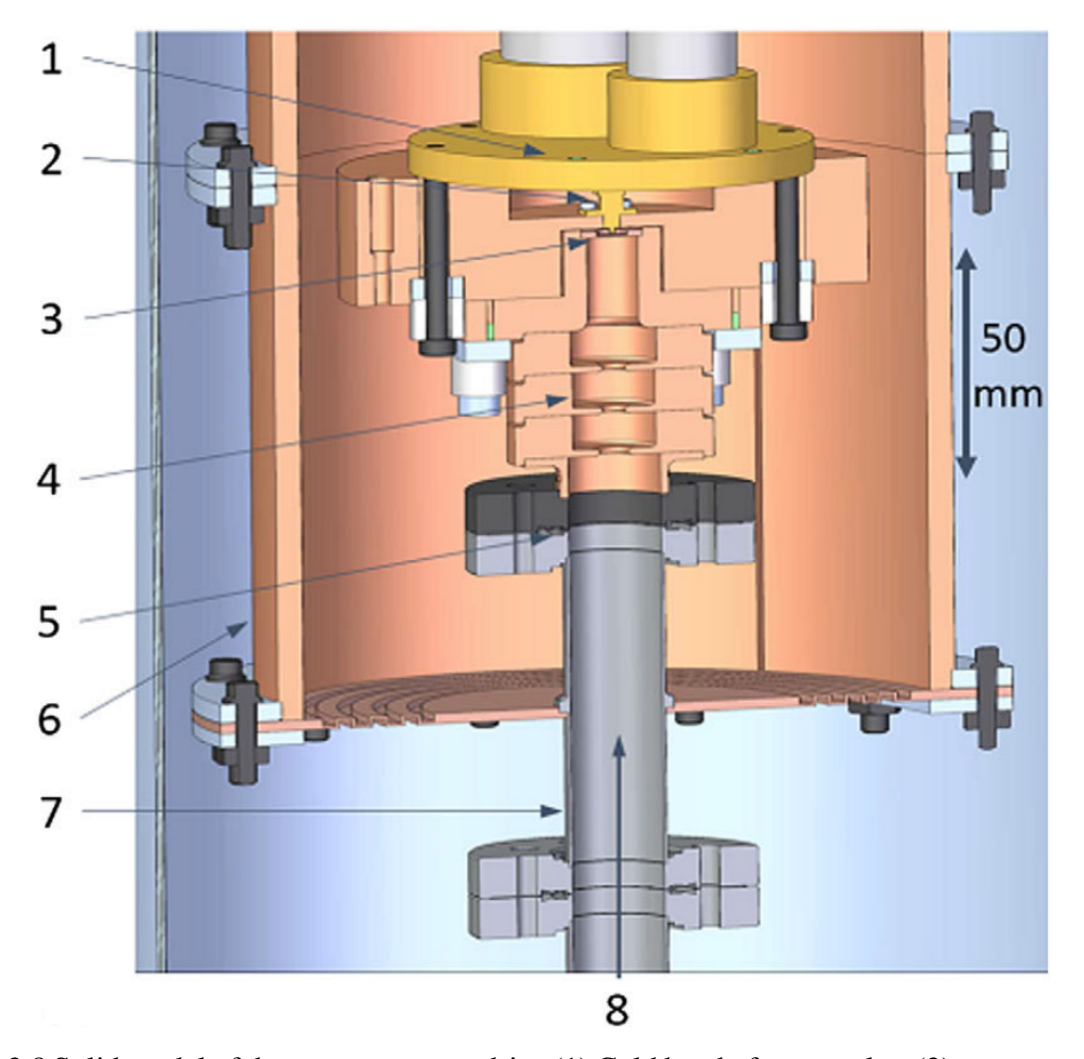


Figure 3.8 Solid model of the cryostat zoomed-in. (1) Cold head of cryocooler; (2) current monitor; (3) brazed metal foil; (4) Cryo-Cu-SLAC; (5) RF flange; (6) thermal shield; (7) Cu-plated stainless steel waveguide; (8) RF input [44].

3.3 Ion trap

For the discussion of ion traps, we will focus on the pioneering work conducted at The Institute of Physical and Chemical Research (RIKEN), Japan. We first set the stage by detailing the components of RIKEN's sophisticated electron-ion elastic scattering system, which includes specialized equipment such as a race track microtron, an electron storage ring, and a unique electron-beam driven rare isotope separator, among others. We then dive into a detailed exploration of the SCRIT device, its trapping efficiency, the overall setup and details of the electron beam performance. The facility's capacity to achieve a high luminosity for stable ions was only the beginning of their trajectory to become the first facility to perform nuclear charge radius measurement on short-lived

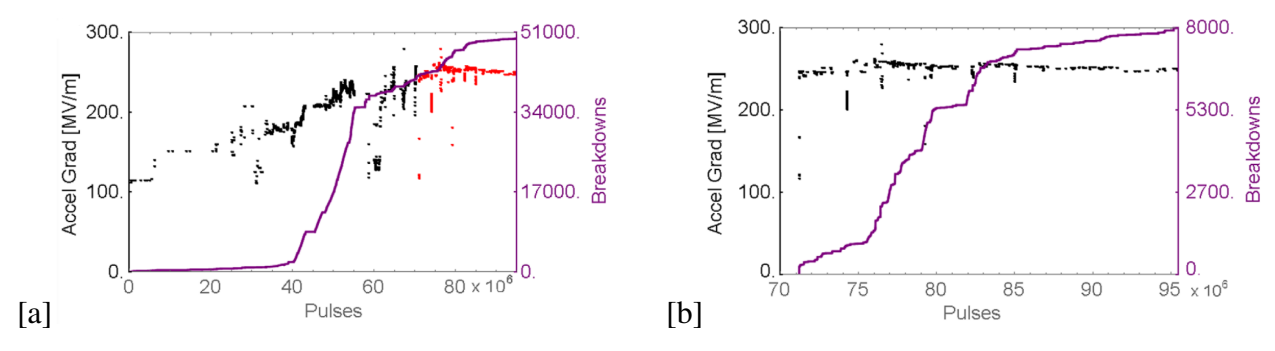


Figure 3.9 The processing history for Cryo-Cu-SLAC. [a] Purple is the number of accumulated breakdowns. Black and red points are the calculated average gradient. Red indicates the time period where breakdown rate was measured. [b] Zoom in of the same data for the period where breakdown rate was measured [44].

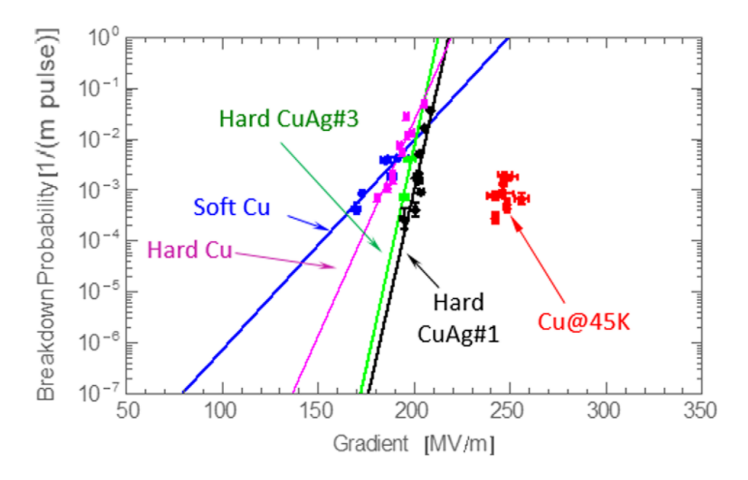


Figure 3.10 Total breakdown rate as a function of accelerating gradient for different structures [44].

nuclei; isotopes that have been out of the reach for electron scattering for decades. This section not only showcases RIKEN's technological prowess, but also underlines the importance of such advanced systems in pushing the boundaries of nuclear physics research.

The Self-Confining Radioactive Ion Target (SCRIT) system at RIKEN was designed to perform precise measurements of the atomic charge radii for short-lived radioactive isotopes, and has already demonstrated it's capabilities with the first ever measurement of electron elastic scattering off 137 Cs last year. Measurements showed up to 10^{27} cm $^{-2}$ s $^{-1}$ luminosity for stable ions with 250 mA electron beam current, and average luminosity of 0.9×10^{26} cm $^{-2}$ s $^{-1}$ for unstable isotopes [48],[49]. The system design consist of a 150 MeV race track microtron (RTM) for electron beam generation, a repurposed electron storage ring (SR2) donated from the National Institute of Advanced Industrial

Science and Technology for electron charge accumulation, an Isotope Separation On-Line (ISOL) system, an electron-beam driven rare isotope separator (ERIS), a DC to RF converter (FRAC), a luminosity monitor (LMon) and a window-frame spectrometer for electron scattering (WiSES). A schematic of the system is presented in Figure 3.11. The storage ring is a second generation synchrotron, composed of a four dipoles and two straight 3.5 m sections for a total circumference of 20 m. These components work in synchrony to generate, accelerate, and accumulate electron beams, as well as to produce and select rare isotopes for experimentation. The ring takes the 150 MeV injected electron beam and can accelerate it up to 500 MeV [7].

Central to the SCRIT system's operation is its innovative ion trapping mechanism located inside the electron ring and illustrated in Figure 3.12. This setup allows the system to hold up to 10⁸ ions in a 500 mm length [50]. When the ions are dumped into the SCRIT device, at energies of about 6 keV, they essentially form a three-dimensional gas target. The recirculating electrons provide transverse focusing, while simultaneously serving as probe for elastic scattering, and a mirror potential, described in more details below, provides longitudinal trapping [7]. For an electron beam current of 250 mA, used normally during data collection, the transverse potential depth produced is roughly 50 V [48]. Data is taken for 1 to 2 s, after which the ions are dumped and the accumulation of electrons starts again.

The SCRIT device has one main electrode structure, with dimensions $99(h) \times 115(w) \times 780(d)$ mm³, and two sub-electrodes. The main composite electrode structure is made of a combination of two 3 mm thick electrodes at the top and bottom, and thin 0.1 mm thick mesh electrodes on both side walls. In order to allow the scattered electrons to enter the detectors, no mesh was placed horizontally over the 35 mm center of the vertical direction. Outside here, the mesh was extended for 8 mm in the horizontal and 5 mm in the vertical direction respectively. The sub-electrodes, used to produce the 6 kV barrier potential, are made of a 2 mm diameter wire in a birdcage-shaped racetrack at both ends of the main electrode [50]. The careful design of these electrodes, including the use of mesh and wire components, facilitates the trapping of ions while allowing scattered electrons to reach the detectors.

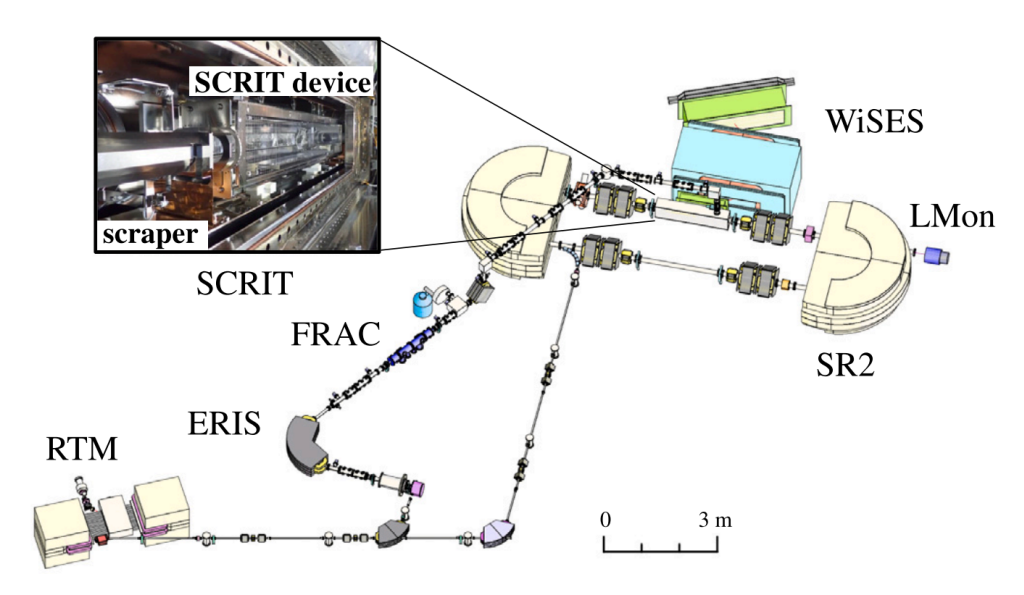


Figure 3.11 Schematic of the SCRIT electron scattering facility. A picture of the SCRIT device in the vacuum chamber is included in the figure [50].

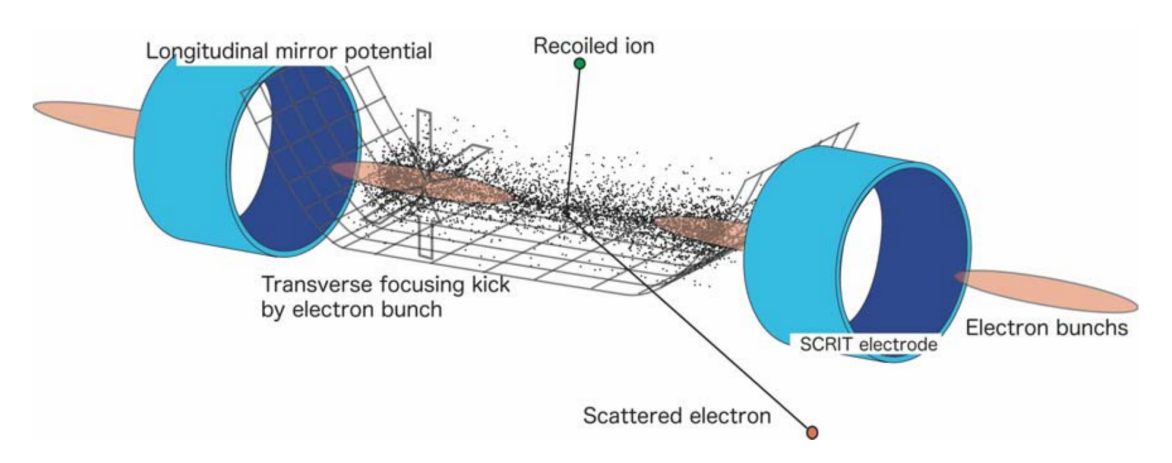


Figure 3.12 Ion trapping concept of SCRIT [7].

During injection, the electron beam power is around 0.4 W at a 2 Hz repetition rate, the repetition rate is later increased for the ion beam production to 20 Hz, which increases the power to 20 W. The peak current for the microtron is almost 3 mA, while at the storage ring 300 mA current is maintain for 1 h lifetime. The cooler buncher system consists of six quadrupole electrodes and a set of einzel-lens and other electrodes for a total length of 950 mm. This buncher converts the continuous ion beam into a 500 μ s pulsed beam [48]. The measured electron beam size is about 2 mm in the horizontal and 0.4 mm in the vertical direction. Once accumulation is completed, the electron beam is deflected before entering the ring to irradiate a uranium carbide target to produce

rare isotopes through photo-fission reactions. The rare isotope beam are selected based on mass and accumulated at FRAC and subsequently dumped at SCRIT where they are trapped and ready for data collection. Investigations of the efficiency of the trapping system have yield a maximum trapping efficiency, as defined in (3.6), of $\epsilon_{trap} = 42\%$, and a overlap efficiency, defined in (3.7), of $\epsilon_{over} = 42\%$, for currents between 200 – 230 mA [50].

$$\epsilon_{trap} = N_{trap}/N_{ini} \tag{3.6}$$

$$\epsilon_{over} = N_{col}/N_{trap} \tag{3.7}$$

In these equations, N_{col} refers to the number of ions colliding with the electron beam, N_{trap} refers to the number of trapped ions, and N_{inj} is the number of injected ions [50].

3.4 Safety considerations

3.4.1 Radiation shielding

When highly energetic particles are bent, accelerated or stopped, they emit different forms of radiation. Of particular interest to us are electrons with energies above a few tens of MeV. Almost every component of an electron acceleration system is capable of producing radiation either by design or due to beam losses. When radiation fields are generated by beam losses they're called prompt radiation. When the electrons hit a target material, they will generate an electromagnetic cascade and those secondary particles will result in prompt radiation. At the energies here considered, the radiation field mainly consist of photons and neutrons.

For a material made of an element with atomic number Z, the critical energy, that is the energy at which the electron collision losses equal the radiation losses, can be approximated as $E_c[\text{MeV}] = 800/(Z+1.2)$. With most accelerators structures made of metals such as copper and stainless steel, with $6 \le Z \le 42$, our electrons with energies above 150 MeV will be well beyond this limit. This implies that the electrons colliding with the material will loose energy mostly through bremsstrahlung photon generation. These photons are generated after an average distance χ_0

[g/cm²] (radiation length) and will take about 63% of the initial electron's energy. After a distance of about 9/7 χ 0, the high energy photon will produce an electron-positron pair and both of these will generate bremsstrahlung photons again after another χ 0 distance, thus the cascade effect. This will continue until the energy of the produced electrons fall bellow E_c and the dominating energy loss process becomes Compton scattering. Photons from bremsstrahlung radiation is the most important hazard at the first line shielding and its emission is forward peaked. The approximate angle at which the intensity drops to half of that at 0° is approximately $\theta_{1/2} = 100/E$ for an electron energy E in MeV. Neutron radiation, on the other hand, does not usually have a predominant angle of radiation emission. When the nucleus absorbs a photon and subsequently emits a neutron, a process called giant resonance production, all the angular information is lost, leading to nearly isotropic radiation fields. Beyond 140 MeV, production of pions and other particles becomes energetically possible and must be considered as well [51].

There are numerous codes, both open source as well as available for purchase, that can help with the design of appropriate shielding. Because of the random nature of scattering events involved in the generation of photons inside the material, the Monte-Carlo technique is often employed to simulate the radiation production. Some of the available codes that employ three -dimensional geometries are FLUKA[52], EGS[53], MCNPX[54] and MARS[55]. Other simpler codes that make use of semi-empirical models also include SHIELD11[56] and SKYSHINE[57].

3.4.2 High voltage insulation

In order to maintain a vacuum of $< 1 \times 10^{-9}$ Pa and bear the high temperatures involved in the baking process, Alumina alloys, with concentrations ranging from 92% up to 99.5%, is the most commonly used choice for insulation. We present the properties of different concentrations in Table 3.2. The insulator must be brazed to a metal ring and then either brazed or welded to a vacuum vessel or flange for vacuum preservation. Much consideration must be made to the brazing geometry and material used for joint.

One can do a rough estimate of the needed insulation diameter by using the formula for a coaxial cylinder, (3.8), although simulation is needed for the final design.

Property	92%	96%	99%	99.5%
Compressive Strength [MPa]	2300		2160	2350
Tensile Strength [MPa]	180	193	241	
Young's Modulus	280	320	360	370
Thermal Expansion [40-800 °C, $\times 10^{-6}$ °C ⁻¹]	7.8	7.9	8.0	8.0
Thermal Conductivity @ $20 ^{\circ}$ C [W (m K) ⁻¹]	18	24	29	32
Dielectric Constant	9.0	9.4	9.9	9.9
RF Loss Factor ($\times 10^{-4}$) @ 1 MHz	54	38	20	10
Volume Resistance @ 20 °C [Ωcm]	$> 10^{14}$	$> 10^{14}$	$> 10^{14}$	$> 10^{14}$
Volume Resistance @ 300 °C [Ωcm]	10^{12}	10^{10}	10^{10}	10^{13}

Table 3.2 Properties of alumina with varying alumina content [19].

$$E = \frac{V/R_{inner}}{ln(R_{outer}/R_{inner})}$$
(3.8)

where V is the voltage on the central conductor, R_{outer} and R_{inner} are the outer and inner radii for the conductor respectively, and E is the electric field on the inner conductor. The outer conductor is part insulator and part conductor [19].

CHAPTER 4

PRELIMINARY STUDIES

4.1 Electron accelerator measurements and modeling

In order to better understand electron accelerator systems, we have studied the Accelerator Test Facility (ATF) at Brookhaven National Laboratory (BNL). We obtained the blueprint of the original design as well as experimental images of the electron beam's transverse profile at different locations. With the first information, we constructed an online version of the system using the open software for particle accelerator simulations OPAL. We then compared the results from this simulation to the experimental images to verify the validity of the simulation. Although some numbers seemed to be close to the actual data, further tuning of the simulation needs to take place before predictions from the model are reliably accurate at all instances. From the images, not only the radius and shape of the beam could be seen, but also the emittance was measured using four images from subsequent beam monitors. Some samples were chosen for these sections to showcase general trends. The reader is referred to Appendix A if interested in observing more data.

4.1.1 Capabilities and specifications of ATF

The Accelerator Test Facility (ATF) electron linac at Brookhaven National Laboratory (BNL) is capable of delivering an electron beam of energies up to 65 MeV, in 0.1-2.0 nC bunches with repetition rate of 1.5 Hz. This beam's normalized emittance has been measured to 1 μ m at 0.3 nC. As can be seen in Figure 4.1 from right to left, the system has a photoinjector gun, followed by two S-band acceleration cavities, a beam diagnostics and focusing section, and at last the experimental hall with different beam-lines. The photonic gun matches the linac section, that is, the copper-elliptical 1.6 cell is operated in the S-band region (2.586 GHz), at a base pressures of 1×10^{-10} Torr [58].

In Figure 4.2, we can see more detailed pictures of the different sections of this system. At the top, Figure 4.2 [a], we have the specific section that we are simulating for, and where all the

¹This image is from a previous model that hasn't been updated with the latest modifications to the experimental hall. Currently, the beam-line at the bottom has been removed, and the middle beam-line bending dipole has been redirected towards the lower left corner.

experimental data was taken. The acceleration sections consist of two TW linear acceleration structures from Stanford Linear Accelerator Center (SLAC). The drive power for both cavities comes from a single XK5 klystron tube, also from SLAC. This klystron provides macro-pulses of 3 μ s with up to 25 MW, 1 to 6 times per second, and those macro-pulses accelerate electron micro-pulses with repetition rates of up to 81 MHz. The other klystron present in the drawings provides the driving power for the SW photoinjector electron gun and it is from Thales. The gun area is magnified in Figure 4.2 [b]. Electrons are extracted from a copper cathode, located in the center of the removable back flange, using a 266 nm laser at around 30 μ J. The QE for this arrangement has been measured to be around 0.01 %. The Thales klystron is connected to the 1.6 elliptical copper cell gun cavity as seen in the image. It can deliver up to 10 MW, although it is typically run at 2.5 MW in 2.5 μ s repetition rate, and has a designed accelerating field of 100 MV/m. Following the gun cavity is a 6 coil pack solenoid that compensate for initial thermal emittance while keeping zero longitudinal magnetic field at the cathode. Through this solenoid runs a 100 A current cooled by water. After the solenoid there is one electron beam monitor right before the accelerator cavities. This monitor is called "LPOP", where L stand for low energy and the POP designation was given in the software used to manipulate these cameras. Lastly, Figure 4.2 [c] at the bottom shows the area right after the beam is accelerated. This section is used for emittance optimization and beam manipulation before it is sent to the experimental area where the users add their probes for experiments. Depicted in this image are three "focusing triplets", Q1, Q2 and Q3. Each of these triplets consist of two 10cm long quadruple magnets, with one 20cm long quadrupole in between them. While the data was taken for the analysis presented here, Q1 and Q2 were off, thus creating a long drift space in which emittance could be calculated. In this picture, there are six electron Beam Position Monitors (eBPM) named "HPOP's" where the "H" stands for high energy. The bunch compressor shown in the image shortens the beam longitudinal spread to around 100 fs with up to 1 kA peak current.

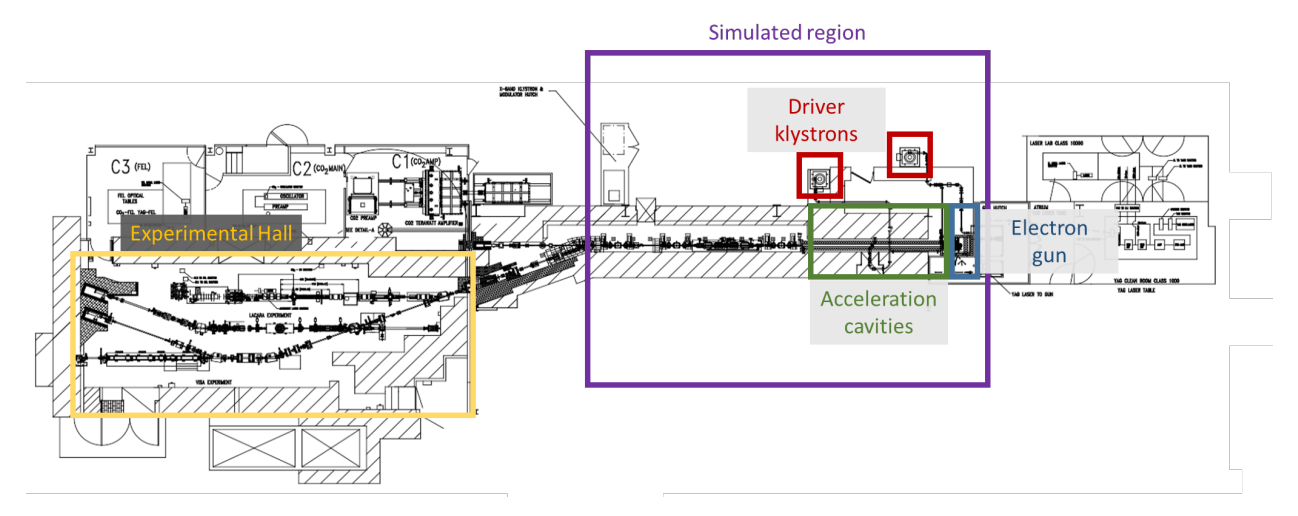


Figure 4.1 Schematic layout of the ATF full system. From right to left, the blue box encapsulates the electron gun, where the electrons are emitted from cathode and focused once, after which follows the acceleration cavities in the green rectangle. These, and the driving klystrons, are all part of the bigger purple rectangle of all the components included in the OPAL simulation. At the lower left corner, the experimental hall is highlighted in a yellow rectangle.

4.1.2 Experimental measurements

Using the Charge-Coupled Device (CCD) cameras with phosphor screens at different locations of the beamline, observed in Figure 4.2, we obtained current intensity images for the transverse profile of the electron beam. These images were then cut to the approximate radius of the beam using an automated python script (presented in Appendix B), in some cases ignoring halo effects and the tail. We determined the edges of the beam by summing over all the rows and columns of each image, thus projecting the beam in the *y* and *x* axis respectively, and cutting wherever the summed intensity was lower than 65% of the average highest intensity. This method at this intensity empirically proved to be very successful at determining the radius for the images after acceleration used for the emittance calculation, but failed to provide an accurate representation of the beam edges for some images taken at LPOP, before acceleration, when the shape of the beam was particularly dim. For that reason, we modified the code to specifically treat images at LPOP1 with a reduced threshold of 35%. Some images were chosen to represent the common trends and are presented in Figure 4.3 with their respective trimmed version. The lines in the images were drew into the CCD cameras by the operators to help them during alignment procedures. The estimated radius obtained with the code for the beam before acceleration ranged from 0.52 mm to

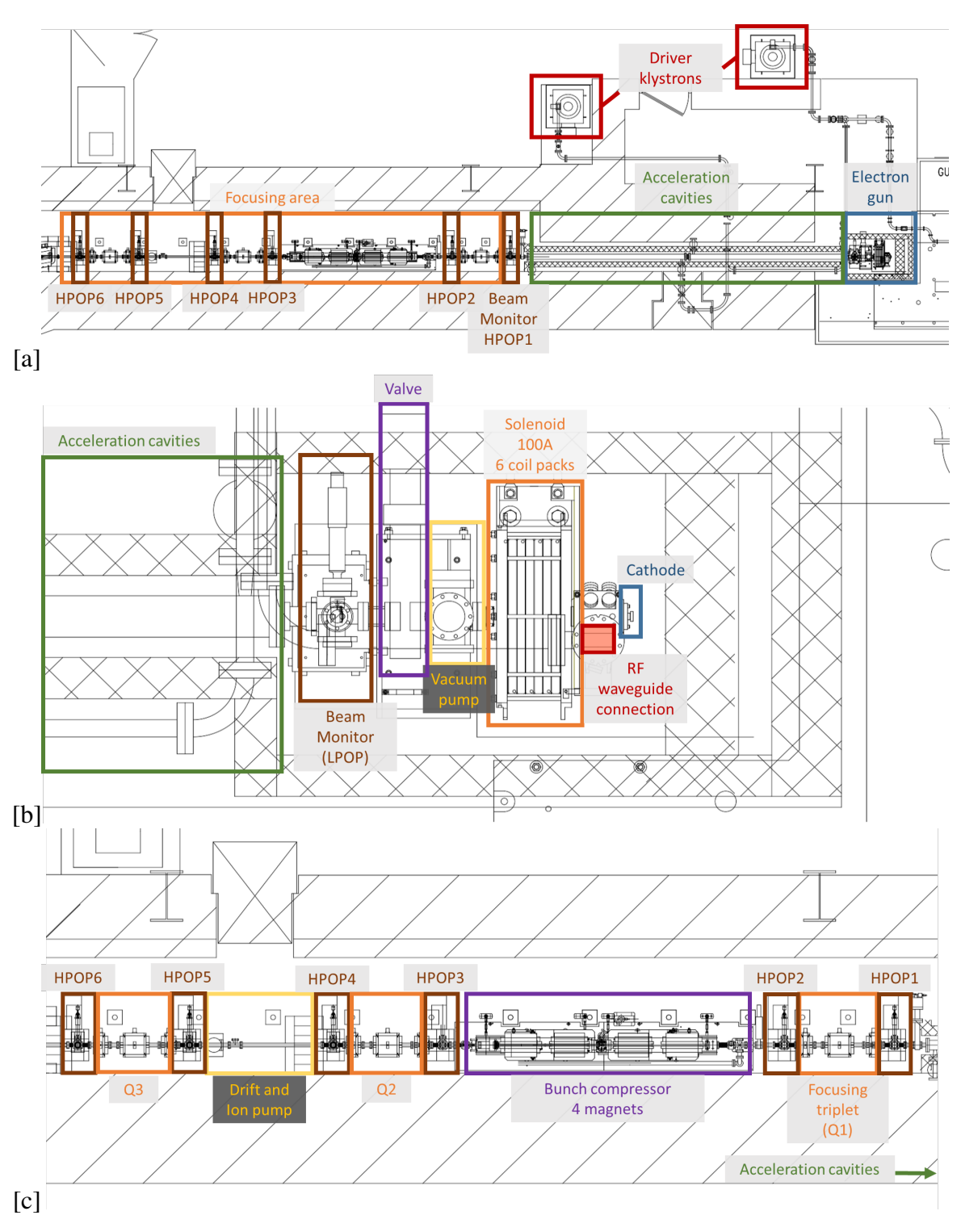


Figure 4.2 Zoomed-in areas of the ATF system. [a] Area simulated using the OPAL software and the locations at which experimental data was collected using eBPM (HPOP's). [b] Components of the electron gun, from extraction up to before acceleration. [c] Systems for beam manipulation and observation after the RF acceleration of the beam.

up to 10 mm, while the range after acceleration was from 0.13 mm (only in the vertical axis while being more prolonged in the horizontal) and up to 1.4 mm.

We observed that to focus the beam at location LPOP, the current solenoid needed to be increased to 120 A or 125 A, the specific one dependant upon the phase of the RF gun. For this location, we analyzed images with RF phases ranging from -19° up to 23°, crossing through 0°. The requirement of either 120 A or 125 A for precise focus did not depended linearly to the phase, but instead oscillated between these two numbers as the phase was varied. As the solenoid current deviates from this number, the beam radius increases drastically in size, with decreasing changes maintaining a more homogeneous shape while increasing changes made the beam look more defused. This is because as the current of the solenoid is increased, the location at which the beam is focus gets closer and after which it defocus again. For the beam to be focused in the vicinity of locations HPOP1 through HPOP5, the solenoid current needed to be reduced to around 100 A. In these images post-acceleration, we can see the projection of the "tail" (examples shown in Figures 4.3 [c] and [d]). Such tail is caused by wakefield effects in the acceleration sections. This effect is mainly created at the irises of the linac section, which are connecting around 100 cells of 10 cm in diameter through holes of about 10 mm diameter. As the beam enters the linac, it posses a longitudinal extension of a few hundred femto-seconds. This not only causes different particles to perceive different RF fields, but as the beam crosses each iris, the field from the front-most part of the beam is reflected in the front wall of the cell and pushes the back-end particles further away. If we could look at the beam from a longitudinal cross-section, one would observe a "fish"-like shape. The upmost front part of the beam would be focus into a Gaussian-like distribution, followed by a thin connection and finally a dispersed extended tail of particles that are being lost due to this wakefield effect. More images showcasing all of the observed attributes are presented in Appendix A.

Another interesting set of data obtained from ATF were alignment images. During normal operation, a roughly homogeneous circular laser profile, depicted in Figure 4.4 [a], is used to create a correspondingly homogeneous circular laser beam. If the laser is not directed exactly perpendicular

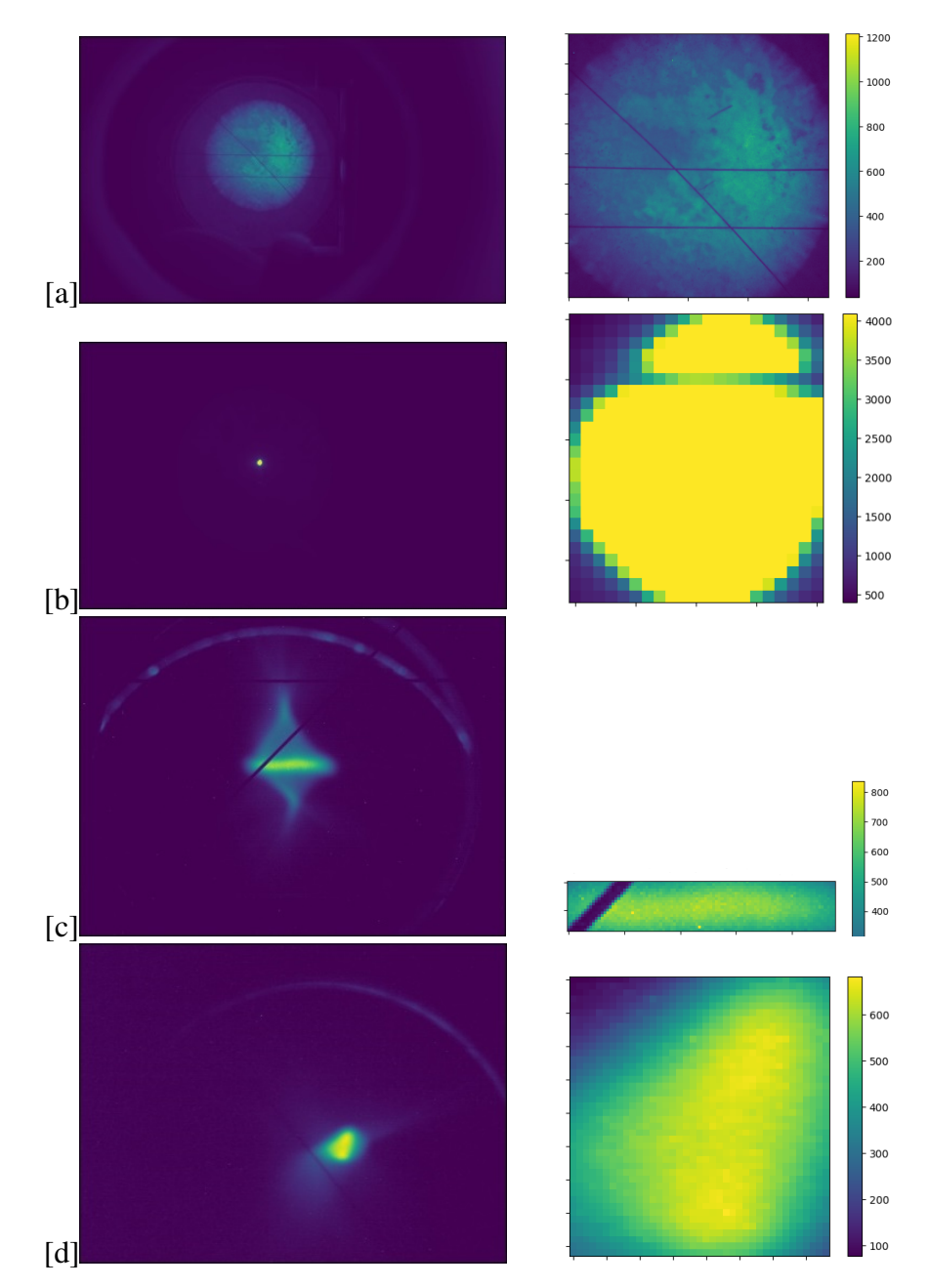


Figure 4.3 Transverse beam profiles of the electron system at ATF unprocessed (left) and after process for beam radius trimming (right), with an RF voltage of 120 V in the gun. [a] and [b] were both taken from the first camera, LPOP1. The former was under an RF phase of -9.0°, solenoid current of 105 A and laser power of 30.44 μ J; while the later was under the conditions of -19°RF phase, solenoid current of 120 A and laser power of 31.95 μ J. [c] and [d] were taken at locations HPOP2 and HPOP4 respectively, both with RF phase of 31°, solenoid current of 100 A and laser power of 30.72 μ J. Intensity scale is for beam current and is given in arbitrary units relative to self.

to the cathode surface, the image will be distorted and will cause unwanted deformations in the beam shape. In order to verify the alignment of the laser, a mask is placed over the laser [b]) and beam is checked for deviations. As can be seen in Figure 4.4 [b], this mask is made of various points that make a circle with line toward the center. If the laser is coming at the cathode with an angle, some points of the circle would appear elongated while the other side would look shortened. In Figure 4.5 we can see a reasonable symmetric beam that was focused onto monitor LPOP by varying the solenoid current.

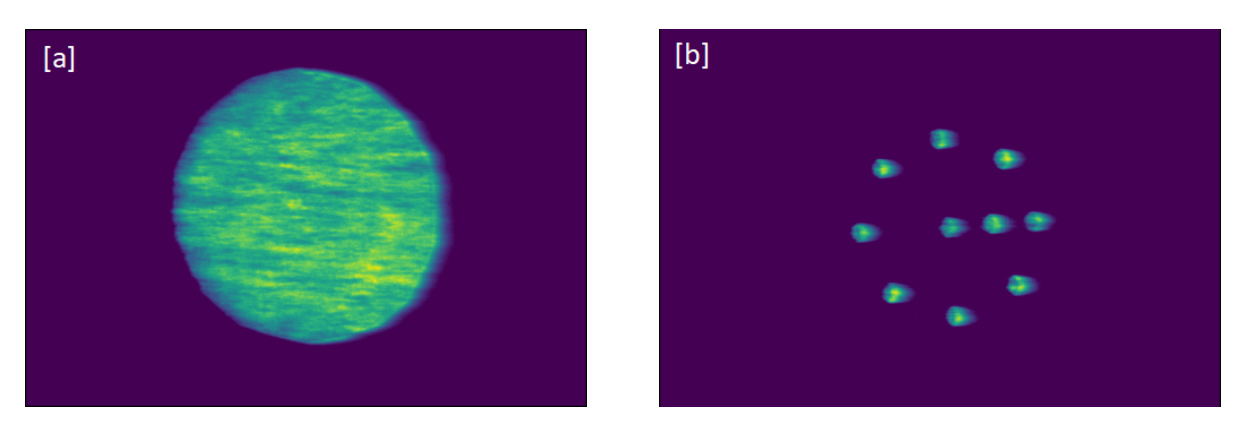


Figure 4.4 Images of the laser illuminating the cathode at ATF. [a] Is the normal operation distribution, while [b] is the mask used during the alignment process.

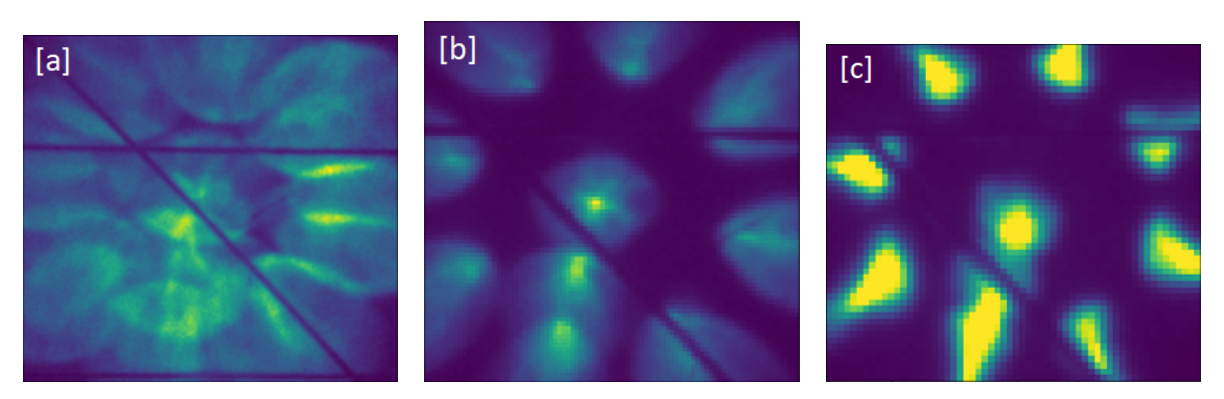


Figure 4.5 Alignment process of ATF. Images were taken with laser power around 1.5 μ J, RF phase of 23° at 120 V in the gun, and solenoid currents of [a] 135 A, [b] 130 A and [c] 125 A. All images come from location LPOP.

4.1.3 Emittance calculation and comparison

We saw before that the beam emittance is by definition the area enclosed by the beam in the phase space of space-angle, mathematically expressed as in (4.1). Here γ , α and β are constants

known as the twiss parameters.

$$\epsilon_x = \gamma x^2 + 2\alpha x x' + \beta x'^2 \tag{4.1}$$

According to [59], one can measure the beam emittance using images from the transverse profile of the beam at three different locations where the beam wasn't accelerated or magnetically manipulated, since any electric or magnetic manipulation can and will change the beam's emittance and the equations herein used to describe the beam's emittance will not apply. Equation (4.2) gives the beam's width based on the measured emittance ϵ , and beta function of the linac $\beta(z)$.

$$\sigma(z) = \sqrt{\beta(z)\epsilon} \tag{4.2}$$

Suppose that we have a electron acceleration system for which we would like to determine the beam emittance that follows the diagram in Figure 4.6. To do the calculation at the location of the dark blue vertical line, we would need three subsequent beam profile monitors at a known distance L_a , L_b and L_c from the reference point, with measured beam width σ_a , σ_b and σ_c respectively. These measurements are taken in drift space, where the beam is not affected by any external electric nor magnetic field. We can use to our advantage the relation (4.3), and solve for two of the twiss parameters and the emittance in the linear equations (4.4).

$$\gamma = \frac{1 + \alpha^2}{\beta} \tag{4.3}$$

$$\sigma_a^2 = \beta \epsilon - 2L_a \alpha \epsilon + L_a^2 \gamma \epsilon,$$

$$\sigma_b^2 = \beta \epsilon - 2L_b \alpha \epsilon + L_b^2 \gamma \epsilon,$$

$$\sigma_c^2 = \beta \epsilon - 2L_c \alpha \epsilon + L_c^2 \gamma \epsilon$$
(4.4)

Using this approach, we were able to calculate the emittance of the beam at ATF. To find the radius of the beam, we trimmed the images using the sum of the intensities in each column and row for the y-axis and x-axis projections respectively as described earlier. We evaluated the emittance in both axes, ϵ_x and ϵ_y , as well as for the diagonal, ϵ_{ms} , where the radii for ϵ_{ms} is the diagonal

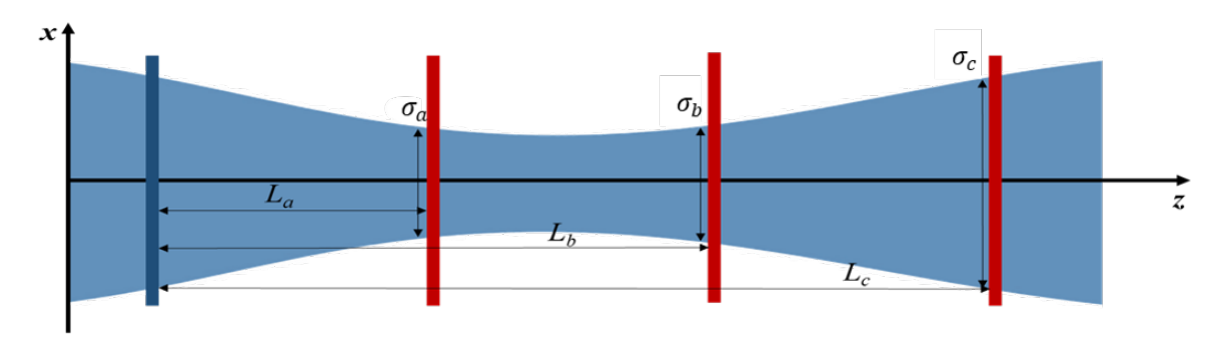


Figure 4.6 Diagram of measurement scheme for emittance in an electron linac. The light blue shade represents the beam's profile, the dark blue vertical line is the reference point where the emittance will be calculated, and the red vertical lines are three positions with beam profile monitors from which we will acquire the data.

formed between the x and y axes, as described in (4.5). We took four consecutive beam profile images from HPOP2, HPOP3, HPOP4 and HPOP5, and made parabolic fittings for (4.6) to obtain the real or geometric emittance. Here We know the actual values of σ_i at the locations z_i and we are using the fitting to find the predicted emittance ϵ , and the value and location of the minimum of the beta function, β_0 and z_0 respectively. Some results of these fittings are presented in Figure 4.7. We obtained normalized emittance ranging from 0.767 mm-mrad to 5.63 mm-mrad, in agreement with previous measurements [60].

$$r_{ms} = \sqrt{r_x^2 + r_y^2/2} (4.5)$$

$$\sigma_i(z_i) = \sqrt{\epsilon \beta_0 \left(1 + \frac{z_i - z_0}{\beta_0^2} \right)} \tag{4.6}$$

4.1.4 Simulation using OPAL framework

The OPAL-t open source tool was used to simulate charged electron particles from the ATF linac. The software records the bunch spatial distribution, the energy spread, the emittance, among other parameters [61]. In Figure 4.8, we show the model used to simulate ATF electron beamline. It included the gun, the 6 coil solenoid, the two acceleration cavities, the first focusing triplet and the CCD cameras from LPOP up to HPOP2. For the emission distribution, we used a Gaussian flattop of 2.8 mm radius. The initial phase space distribution in the x-px plane is portrayed in

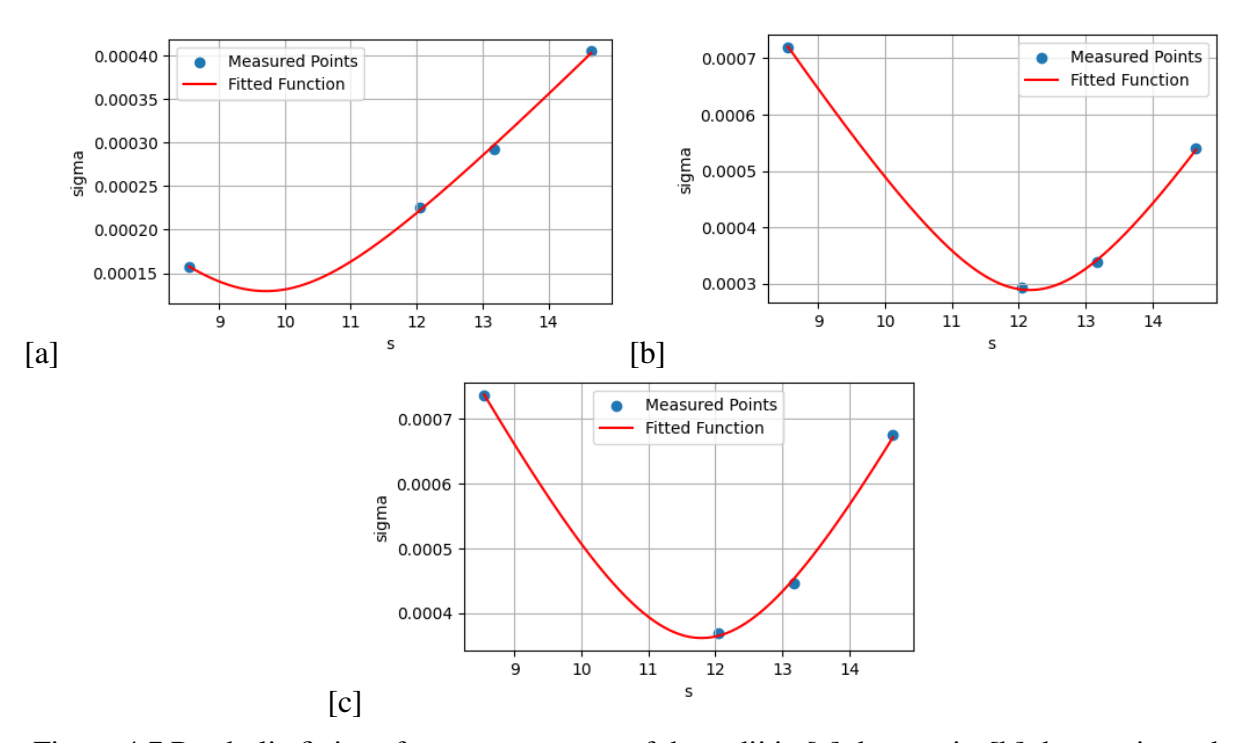


Figure 4.7 Parabolic fittings for measurements of the radii in [a] the x-axis, [b] the y-axis, and [c] the diagonal radius calculated from (4.5), for the operational conditions of RF phase of 31°, RF voltage of 120 V at the gun and a solenoid current of 100 A for space charge correction. Notice that the x-axis in this graphs, 's', is the position in the beamline in meters, while the y-axis 'sigma' refers to the electron beam radius also in meters.

Figure 4.9 [a]. The simulation accounts for the space charge effect created by the electron beam bunch using self-consistent electrostatic approximation, and determines the equation of motion from the relativistic Lorentz equation of these particles as they travel through the electromagnetic fields created in the acceleration system. OPAL has tools to account for wakefield effects, but we did not incorporated them into our simulation because of the intense computing power required for the calculation, which would have extended by a factor of 15 the time for each simulation.

We used 3 different field maps for this simulation; two "AstraDynamic" for the electron gun and the acceleration sections, and one "AstraMagnetoStatic" for the solenoid in the gun. These field maps describe the magnetic or electric profile of the element along the beam axis, and are used by OPAL to calculate a Fourier series from which values off-axis can be determined. For all the fields in this simulation, only the first N = 40 Fourier terms were used. The field maps are generic ones taken from online examples. The parameters shown in Table 4.1 were used for the simulation from

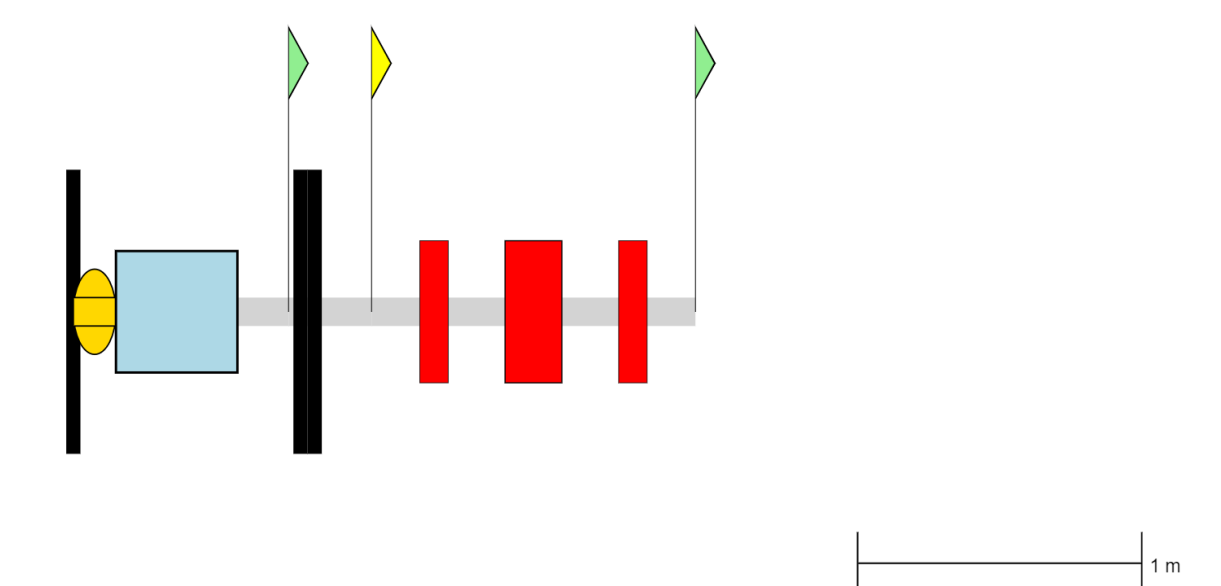


Figure 4.8 Visual representation of the beamline created using OPAL. From left to right: the first black rectangle is the cathode, the yellow circle is the gun acceleration, the blue box is the solenoid, the flags are CCD cameras, the two joint thin black rectangles are the acceleration sections (compacted) and the later three red rectangles are more quadrupole magnets.

which all the images in this section were taken.

Parameter	Value	Units
RF gun phase	3.5	degrees
RF gun voltage	100	volts
Linac phase	19	degrees
Linac power	10	volts
Beam current	2.46×10^{-8}	amperes
Solenoid current	96	amperes
Quadrupole current	7	amperes

Table 4.1 Variable parameters used for the OPAL simulation.

In Figure 4.9 [b] we can see the energy gain of the particles along the beamline with the end of the linac section marked with a dash line. This graph was the first sign that the field maps used for the simulation may not be a realistic representation of the system. We can see that the beam gains energy after the linac sections, particularly, the quadrupoles seem to be providing acceleration to the particles. This was proven by changing the current; with increasing current we observed increasing energy. On the other hand, the energy gained by the particles inside the acceleration cavities accurately represents the energy of the beam measured at the facility.

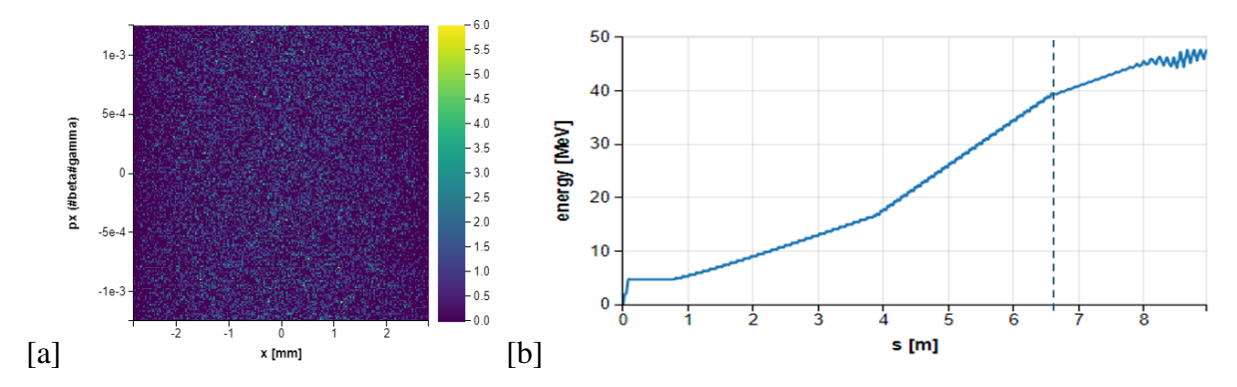


Figure 4.9 Simulation using OPAL codes for [a] initial phase space and [b] the energy gain of the electron beam. In [b] the vertical blue dash line marks the end of the acceleration sections.

We can observe the transverse beam profile images of the simulated electron beam at different locations in Figure 4.10. We first notice that the image after acceleration doesn't posses any tail or halo' it is perfectly symmetric. This is because space charge effects only cause the beam to spread, and all deformations from a circle come from the wakefield effect ignored in this simulation. The second thing to notice is that the beam profile after exiting the solenoid (this corresponds to the location of LPOP) has immediately been compressed. In real life, we know that with a current of 96 A the beam should be focusing at a minimum radial shape around HPOP4, much further down the beamline. This is the second clue that suggested errors within the magnetic field maps. Furthermore, notice that right after exiting the quadrupoles the beam profile has increased almost four times its size. This is the contrary effect of what is expected. Quadrupole fields are supposed to focus the beam in one direction while defocusing in the perpendicular axis. It is well known, though, that the focusing effect is much stronger than the defocusing, such that after various successive quadrupoles positioned in perpendicular to each other, the net result should be a compressed beam. The emittance of the beam was estimated to be around 51 mm mrad before acceleration and 14 mm rad after acceleration. This discrepancy with experimental results is believed to be correlated to the magnetic fields as well since we know that solenoids and quadrupoles are used for emittance compensation.

Upon concluding this investigation we have decided that refinement of the magnetic field maps for the elements in this simulation needs to take place in order for the simulation to match

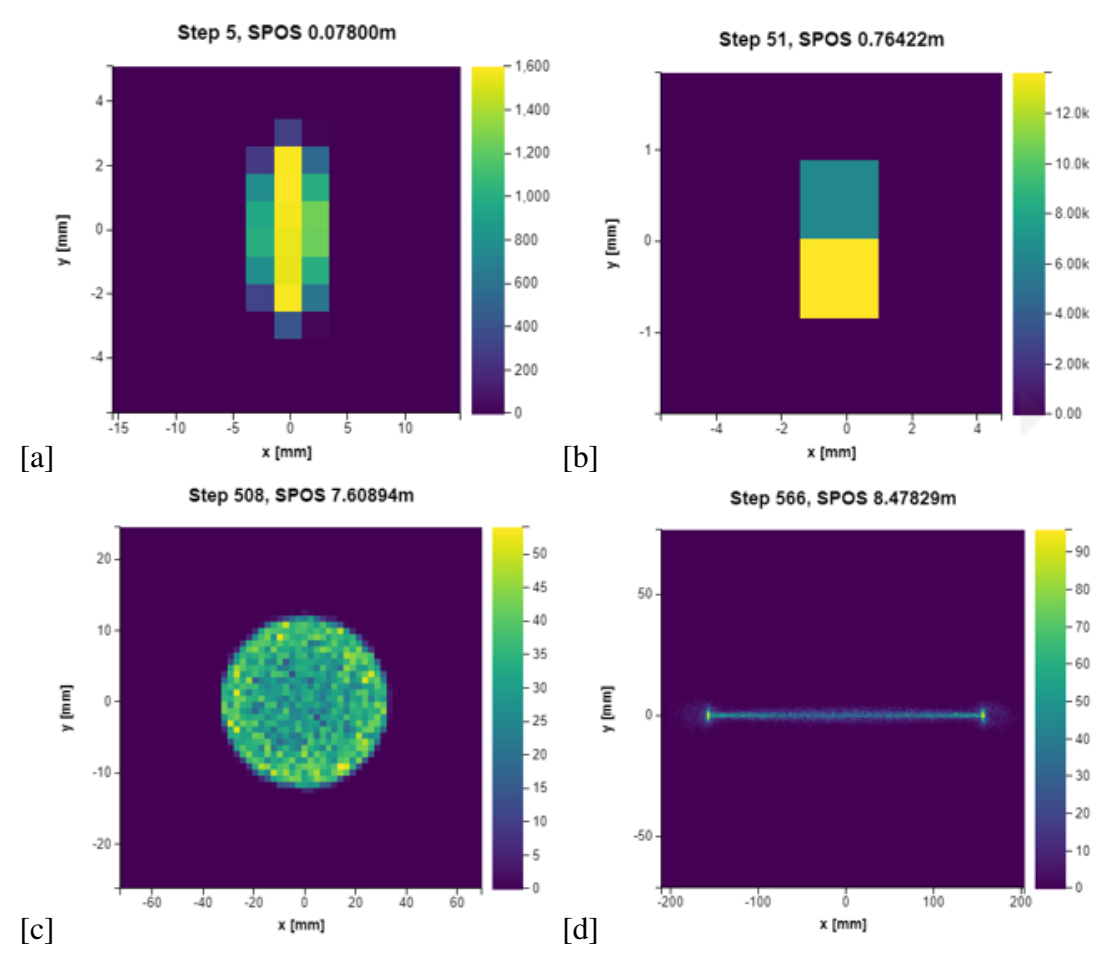


Figure 4.10 Simulation using OPAL codes for the beam profile images [a] before entering the solenoid, [b] right after exiting the solenoid, [c] after exiting the linac sections and [d] right after exiting the first focusing quadrupole triplet (Q1).

experimental results. Other simulation software will be used to generate them.

4.2 Ion trap and design strategy

4.2.1 Capabilities and specifications of D-line

FRIB is capable of producing ion beams from an assortment of elements, ranging from H to 238 U, with energies of over 200 MeV in current beams as high as 3.7 p μ A² of approximately 0.5 mm radius. This beam is produced from the collision of a primary-very-fast stable-isotope beam (generated using electron-cyclotron resonance sources) with a selected (also stable and usually light, such as beryllium or carbon) target which causes projectile fragmentation, and the resulting unstable

²"The electrical current in nanoamperes (10^{-9} A) that would be measured if all beam ions were singly charged" [62].

isotopes follow particle and energy selection processes [63]. After selection, the rare isotopes can be stopped in helium gas-cells for low energy experiments. For our interest, we take a closer look at a later portion of the beamline named D-line, where the ion beam's energy is significantly reduced to about 30 keV and can be cooled to a momentum spread as small as $\frac{\Delta p}{p} \approx 10^{-5}$.

4.2.2 Calculations for rare isotope and electron interactions

The number of ions per unit of time, N_{τ} , that can be confined inside the trap can be estimated from the known parameters of the electron beam. If we assume that the electron beam is fully neutralized with the ions in the target, such that the total charge for each is the same, we can calculate N_{τ} as in (4.7). In this equation, I_e is the electron current, v is the velocity of the beam, L is the length of the trap, and e is the unit charge of an electron $e = 1.602 \times 10^{-19}$ C.

$$N_{\tau} = \frac{I_e L}{e v} \tag{4.7}$$

If our electrons have energies of about 150 MeV, they are relativistic and we can calculate their velocity from (2.36) giving approximately v c, and from this one can estimate the density capacity of the trap. We present such estimates in Table 4.2 for an electron current ranging from 1 mA to 1 A, assuming 100% efficiency for a trap length of 0.5 m (the length of SCRIT) and assuming that all of our ions are confined in a 2.5 mm radius from the center of the electron beam.

Current in A	# of ions	# of electrons	Ion density in 1/cm ²	Luminosity in 1/s/cm ²
0.001	1.04×10^{07}	6.24×10^{15}	5.30×10^{07}	3.31×10^{23}
0.01	1.04×10^{08}	6.24×10^{16}	5.30×10^{08}	3.31×10^{25}
0.1	1.04×10^{09}	6.24×10^{17}	5.30×10^{09}	3.31×10^{27}
0.2	2.08×10^{09}	1.25×10^{18}	1.06×10^{10}	1.32×10^{28}
0.3	3.12×10^{09}	1.87×10^{18}	1.59×10^{10}	2.98×10^{28}
0.4	4.16×10^{09}	2.50×10^{18}	2.12×10^{10}	5.29×10^{28}
0.5	5.20×10^{09}	3.12×10^{18}	2.65×10^{10}	8.27×10^{28}
0.6	6.24×10^{09}	3.74×10^{18}	3.18×10^{10}	1.19×10^{29}
0.7	7.28×10^{09}	4.37×10^{18}	3.71×10^{10}	1.62×10^{29}
0.8	8.32×10^{09}	4.99×10^{18}	4.24×10^{10}	2.12×10^{29}
0.9	9.37×10^{09}	5.62×10^{18}	4.77×10^{10}	2.68×10^{29}
1	1.04×10^{10}	6.24×10^{18}	5.30×10^{10}	3.31×10^{29}

Table 4.2 Predicted luminosity and number of ions for a given electron beam current.

According to [64], the electric space charge potential produced by an electron beam can be calculated by (4.8), with the linear charge density as in (4.9). A description of the variables used in these equations, with the assumed values, can be found in Table 4.3, and the resulting potential is presented in Figure 4.11.

$$\phi = \frac{Q_e}{2\pi\epsilon_0} \begin{cases} \left[\frac{1}{2} \left(1 - \frac{r^2}{b^2} \right) + \ln\left(a/b\right) \right], & 0 \le r \le b, \\ \ln\left(a/r\right), & b < r \le a, \end{cases}$$
(4.8)

$$Q_e = \frac{-I_e}{\beta c} \le 0 \tag{4.9}$$

Parameter	Value	Unit
Electron beam radius b	0.005	m
Beam tube radius <i>a</i>	0.25	m
Permittivity of free space ϵ_0	8.85×10^{-12}	F/m
Electron current I_e	0.5	A
Relativistic electron velocity β	1.00	unit-less
Speed of light <i>c</i>	3.00×10^{8}	m/s

Table 4.3 Variables used for the calculation of the electric potential produced by an electron beam of 150 MeV.

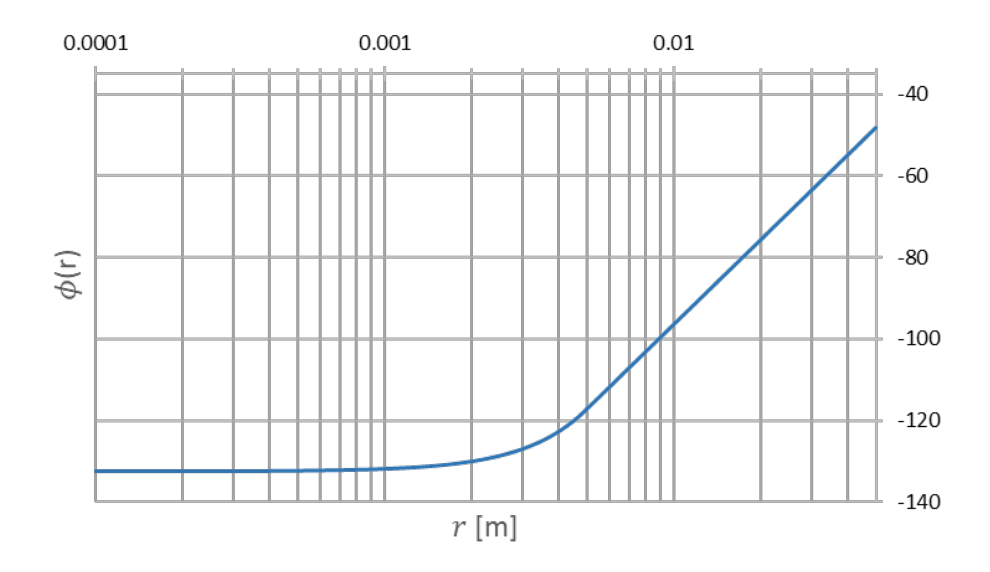


Figure 4.11 Predicted electric potential inside the ion trap.

CHAPTER 5

SUMMARY AND OUTLOOK

The Facility for Rare Isotope Beams (FRIB) stands at the forefront in the quest to deepen our understanding of the nuclear structure, by providing beams of isotopes with sub-milliseconds lifetimes in the greatest densities ever seen. This thesis aimed to investigate the feasibility of integrating an electron beam with FRIB's capabilities to perform electron elastic scattering experiments, thereby contributing to the precise measurement of nuclear charge radii and the charge density distribution of rare isotopes, complementing the existing reach of its BECOLA facility. A comprehensive review of the technology necessary to perform electron elastic scattering off online ions was presented in pair with the theory of the experiment. We discussed the details from the cathode, explored the option of using either photoemission or thermionic guns, presented the latest advanced compact RF acceleration cavity, explained the technology implemented at RIKEN for the simultaneous trapping and scattering of electrons off ions, and presented information of the science that allows precise measurement of the angular and energy distributions. High voltage insulation and radiation safety aspects were also discussed since ensuring the safety of the system and the personnel is always a priority.

The study of the BNL electron linac test facility helped us understand the structural and operational requirements of an electron beam facility. With the measurements of the transverse beam profile at multiple locations, we were able to extract the geometrical and normalized emittance. The measurement of the emittance, as well as the reconstructed beam radius, were in agreement with previous observations. The effect of the RF phase on the beam was evaluated from the profile images. Our computational model needs further improvements, one of which being a revision of the field maps. Additional upgrades will include wakefield effects and RF cavities with higher accelerating gradient such as the cold copper cavity developed by SLAC.

We also analyzed the electron-ion trapping potential and made an estimate for the achievable luminosity of the system. The ability to trap ions effectively and achieve high luminosity is vital for conducting successful scattering experiments. Our findings indicated that with an electron gun

that can provide 100 mA, it is possible to attain a luminosity of up to $3 \times 10^{27} \text{ cm}^{-2} \text{s}^{-1}$, sufficient for high-precision measurements of absolute nuclear charge radius. In order to achieve the required luminosities, thermionic guns offer the best beam properties (high average currents with small radius) for a one-pass system. If a photocathode gun is desired, for the potential to be upgraded to allow a spin polarized electron beam, a re-circulation scheme is required in order to obtain the necessary average current. The cold copper structure for particle acceleration developed by SLAC would be the best fit for a compact system that could achieve the desired energies since it has demonstrated the highest accelerating gradients to date. It is possible to use other accelerating structures, but these would lead to a higher space requirement since their accelerating gradients are significantly smaller. As for the interaction region, a modified version of the SCRIT concept developed by RIKEN to trap the ions while simultaneously carrying out both scattering experiments and laser spectroscopy is a good starting point.

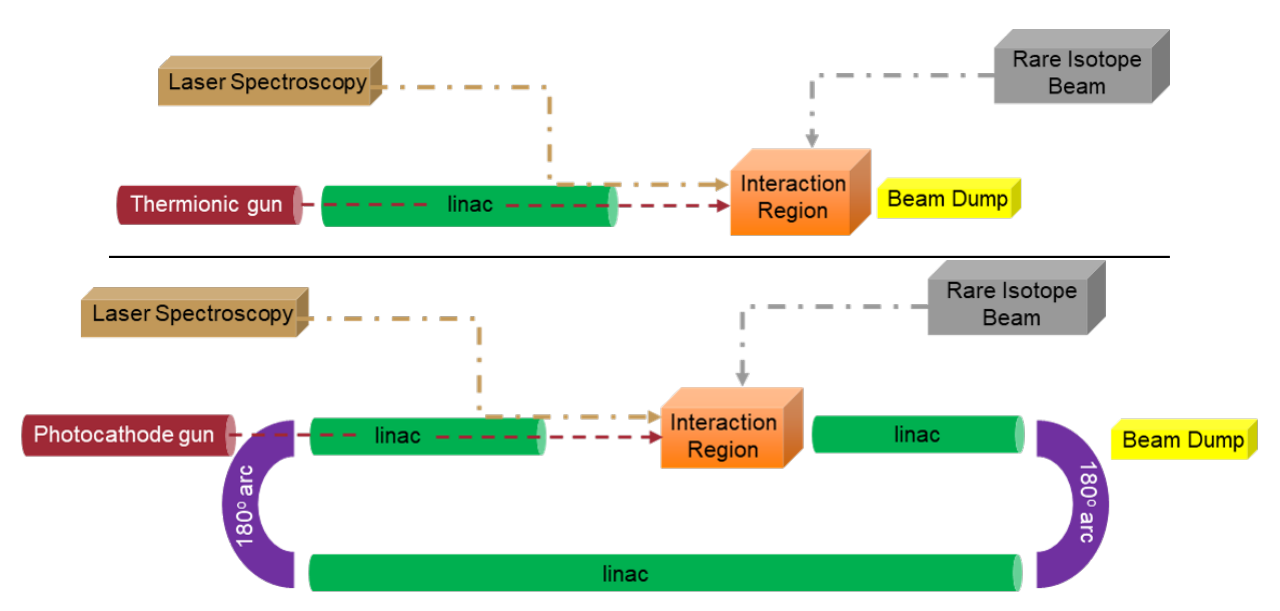


Figure 5.1 Possible schematic concepts for the electron acceleration systems that would allow charge radius and charge density distribution experiments with radioactive isotopes at FRIB. At the top is the idea of a single-pass system and below the recirculating electron beam for current accumulation. Courtesy of Paul Gueye.

Figure 5.1 depicts two schematics of the concept developed in this thesis, showing the essential components of the system while detectors, cooling systems, power supplies and other supporting equipment are omitted. The dual use of laser spectroscopy and electron scattering will provide

cross-reference measurements. The diagram at the top shows a single pass before the electrons are dumped. This design can only be achieved using thermionic guns because of the high average current required to observe beyond the first minimum of the form factor. If a photoemission gun is chosen, one would need to accumulate enough electrons before performing the experiments in order to have a sufficiently high luminosity. This concept of re-circulating electrons is implemented at RIKEN and also with slightly different implementation at the Continuous Electron Beam Accelerator Facility (CEBAF) at Jefferson National Laboratory. Using energy recovery linacs would be ideal for either single-pass or re-circulating systems in order to reduce cost.

The precise measurement of nuclear charge radii for radioactive isotopes will fill a critical gap in our current knowledge of the nuclear matter, providing essential data for theoretical models. These models are foundational for understanding various nuclear phenomena and for applications in nuclear medicine, astrophysics, and energy research. While this thesis lays the groundwork for integrating an electron acceleration system with FRIB, several avenues for future research and development remain. In the future, the computational model must be expanded to achieve an electron beam with energies above 150 MeV, and potentially the design of the gun should be modified to accommodate for higher currents and subsequently higher brightness. After the electron beam is modelled with the desired parameters, the next step would be to build a small prototype of the ion trap, and potentially the electron gun with minimum energy. This will involve collaborative efforts with national labs and universities, and multi-disciplinary teams to overcoming complex technical hurdles.

BIBLIOGRAPHY

- [1] MSU Today. "FRIB Grand Opening". In: (2022). Accessed: 2024-06-26. URL: https://msutoday.msu.edu/news/2022/frib-grand-opening.
- [2] A. J. Miller. "Measurements of charge radii of neutron-deficient calcium using collinear laser spectroscopy at BECOLA". PhD dissertation. Michigan State University, 2019.
- [3] T. Suda and H. Simon. "Prospects for electron scattering on unstable, exotic nuclei". In: *Progress in Particle and Nuclear Physics* 96 (2017), pp. 1–31. URL: https://api.semanticsc.holar.org/CorpusID:125679986.
- [4] H. De Vries, C.W. De Jager, and C. De Vries. "Nuclear charge-density-distribution parameters from elastic electron scattering". In: *Atomic Data and Nuclear Data Tables* 36.3 (1987), pp. 495–536. ISSN: 0092-640X. DOI: https://doi.org/10.1016/0092-640X(87)90013-1.
- [5] I. Angeli and K.P. Marinova. "Table of experimental nuclear ground state charge radii: An update". In: *Atomic Data and Nuclear Data Tables* 99.1 (2013), pp. 69–95. ISSN: 0092-640X. DOI: https://doi.org/10.1016/j.adt.2011.12.006.
- [6] R. Hofstadter, H. R. Fechter, and J. A. McIntyre. "High-Energy Electron Scattering and Nuclear Structure Determinations". In: *Phys. Rev.* 92 (4 1953), pp. 978–987. DOI: 10.1103/PhysRev.92.978.
- [7] M. Wakasugi. "Electron scattering from unstable nuclei with the SCRIT". in: 2005. URL: https://ribf.riken.jp/RIBF-TAC05/14_SCRIT.pdf. Presentation given at RIBF TAC05, Japan.
- [8] CPI-Eimac. *Model YU-156*. Accessed: 2024-07-10. URL: https://fair-center.eu/user/experiments/nustar/experiments/elise.
- [9] L. G. Grigorenko et al. "Scientific program of DERICA—prospective accelerator and storage ring facility for radioactive ion beam research". In: *Physics-Uspekhi* 62.7 (2019), p. 675. DOI: 10.3367/UFNe.2018.07.038387.
- [10] B. Povh et al. *Particles and Nuclei: An Introduction to the Physical Concepts.* 7th ed. Graduate Texts in Physics. Springer Berlin, Heidelberg, 2015. ISBN: 978-3-662-46321-5. DOI: 10.1007/978-3-662-46321-5.
- [11] K.S. Krane. *Introductory Nuclear Physics*. John Wiley and Sons, 1987. ISBN: 97804718055 33.
- [12] B. Simons. *Lecture 20: Scattering theory*. University of Cambridge lecture. Accessed: 2024-07-11. 2020. URL: https://www.tcm.phy.cam.ac.uk/~bds10/aqp/lec20-21.pdf.

- [13] K. Foster. *Electron Scattering: Form Factors and Nuclear Shapes*. Electronic Notes. Accessed: 2024-06-02. 2011. URL: https://www.pdffiller.com/396817084--eScatteringFormFactors_Supplementalpdf-Electron-Scattering-Form-Factors-and-Nuclear-.
- [14] R. C. Barrett. "Nuclear charge distributions". In: *Reports on Progress in Physics* 37.1 (1974), pp. 1–54. DOI: 10.1088/0034-4885/37/1/001.
- [15] Y. S. Tsai. *Radiative corrections to electron scattering*. SLAC-PUB-848. 1971. URL: https://www.slac.stanford.edu/pubs/slacpubs/0750/slac-pub-0848.pdf.
- [16] P. Guèye et al. "Dispersive corrections in elastic electron-nucleus scattering: an investigation in the intermediate energy regime and their impact on the nuclear matter". In: *The European Physical Journal A* 56.5 (2020), p. 126. DOI: 10.1140/epja/s10050-020-00135-7.
- [17] A. Afanasev et al. *Radiative Corrections: From Medium to High Energy Experiments*. 2023. arXiv: 2306.14578.
- [18] Georg Gaertner, Wolfram Knapp, and Richard G. Forbes, eds. *Modern Developments in Vacuum Electron Sources*. 1st ed. Topics in Applied Physics. Springer Cham, 2020. ISBN: 978-3-030-47291-7. DOI: 10.1007/978-3-030-47291-7.
- [19] T. Rao and D. H. Dowell. *An Engineering Guide to Photoinjectors*. Independent Publishing Platform, 2014.
- [20] K. L. Jensen. et al. "Electron emission from a single Spindt-type field emitter structure: Correlation of theory and experiment". In: *Applied Physics Letters* 68 (May 1996), pp. 2807–2809. DOI: 10.1063/1.116331.
- [21] K. Wille. *The Physics of Particle Accelerators: An Introduction*. Oxford University Press, 2000. ISBN: 9780198505495.
- [22] OpenStax University Physics. 11.5: Particle Accelerators and Detectors University Physics III Optics and Modern Physics. https://phys.libretexts.org/Bookshelves/University_Physics/University_Physics_(OpenStax)/University_Physics_III_-_Optics_and_Modern_Physics_(OpenStax)/11:_Particle_Physics_and_Cosmology/11.05:_Particle_Accelerators_and_D etectors. Accessed: 2024-02-28.
- [23] X Cid Vidal and R. Cid Manzano. *Taking a Closer Look at LHC: RF Cavities*. Accessed: 2024-02-28. URL: https://www.lhc-closer.es/taking_a_closer_look_at_lhc/0.rf_cavities.
- [24] L.C. Teng. *Minimizing the.Emittance in Designing the Lattice of an Electron storage Ring*. Fermilab Report No. TM-1269. URL: https://lss.fnal.gov/archive/test-tm/1000/fermilab-t m-1269.pdf.
- [25] S. Y. Lee. "Emittance optimization in three- and multiple-bend achromats". In: *Phys. Rev.*

- E 54 (2 Aug. 1996), pp. 1940–1944. DOI: 10.1103/PhysRevE.54.1940.
- [26] K M Potter. "Luminosity measurements and calculations; 1985 ed." In: (1985). DOI: 10.5170/CERN-1985-019-V-1.318.
- [27] G. Gevorkyan et al. "A cryogenically cooled 200 kV DC photoemission electron gun for ultralow emittance photocathodes". In: *Review of Scientific Instruments* 94.9 (2023), p. 091501. ISSN: 0034-6748. DOI: 10.1063/5.0160818.
- [28] T. Siggins et al. "Performance of a DC GaAs photocathode gun for the Jefferson lab FEL". in: *Nuclear Instruments and Methods in Physics Research Section A: Accelerators, Spectrometers, Detectors and Associated Equipment* 475.1 (2001). FEL2000: Proc. 22nd Int. Free Electron Laser Conference and 7th F EL Users Workshop, pp. 549–553. ISSN: 0168-9002. DOI: https://doi.org/10.1016/S0168-9002(01)01596-0.
- [29] C. Hernandez-Garcia et al. "A High Average Current DC GAAS Photocathode Gun for ERLS and FELS". in: *Proceedings of the 2005 Particle Accelerator Conference*. 2005, pp. 3117–3119. DOI: 10.1109/PAC.2005.1591383.
- [30] D. T. Pierce and F. Meier. "Photoemission of spin-polarized electrons from GaAs". In: *Phys. Rev. B* 13 (12 1976), pp. 5484–5500. DOI: 10.1103/PhysRevB.13.5484.
- [31] Hyeri Lee et al. "A cryogenically cooled high voltage DC photoemission electron source". In: *Review of Scientific Instruments* 89.8 (2018), p. 083303. ISSN: 0034-6748. DOI: 10.1063/1.5024954.
- [32] *Chromacity 520 nm Femtosecond Laser*. Chromacity Lasers. Accessed: 2024-02-19. URL: https://chromacitylasers.com/ultrafast-lasers/chromacity-520/.
- [33] *PL520B Osram 80 mW 520 nm Green Laser Diode*. Opt Lasers. Accessed: 2024-02-19. URL: https://optlasers.com/laser-diodes/pl520b-osram-80-mw-520-nm-laser-diode.
- [34] Spirit-OPA® High Repetition Rate Automated Optical Parametric Amplifier. Spectra-Physics. Accessed: 2024-02-19. URL: https://www.spectra-physics.com/.
- [35] B. Dunham, L. Cardman, and C.K. Sinclair. "Emittance Measurements for the Illinois/CE-BAF Polarized Electron Source". In: *Proceedings of 1995 Particle Acceleration Conference* 2 (Apr. 1998). DOI: 10.1109/PAC.1995.505119.
- [36] L. Guo et al. "Rugged bialkali photocathodes encapsulated with graphene and thin metal film". In: *Scientific Reports* 13.1 (2023), pp. 1–12. DOI: 10.1038/s41598-023-29374-6.
- [37] J. K. Bae et al. "Operation of Cs–Sb–O activated GaAs in a high voltage DC electron gun at high average current". In: *AIP Advances* 12.9 (2022), p. 095017. ISSN: 2158-3226. DOI: 10.1063/5.0100794.

- [38] K. Pepitone et al. "Operation of a high-current drive beam electron gun prototype for the Compact Linear Collider". In: *Review of Scientific Instruments* 91.9 (2020), p. 093302. ISSN: 0034-6748. DOI: 10.1063/5.0013144.
- [39] CPI-Eimac. *Model YU-156*. Accessed: 2024-02-08. URL: https://www.cpii.com/product.c fm/1/22/131.
- [40] P. Sprangle et al. *High Average Current Electron Guns for High-Power FELs*. Naval Research Laboratory. NRL/MR/6790–09-9230. 2009.
- [41] W.F. Toonen et al. "Development of a low-emittance high-current continuous electron source". In: *Nuclear Instruments and Methods in Physics Research Section A: Accelerators, Spectrometers, Detectors and Associated Equipment* 1013 (2021), p. 165678. ISSN: 0168-9002. DOI: https://doi.org/10.1016/j.nima.2021.165678.
- [42] S. Kutsaev. "Electron bunchers for industrial RF linear accelerators: theory and design guide". In: *European Physical Journal Plus* 136 (Apr. 2021), p. 446. DOI: 10.1140/epjp/s 13360-021-01312-3.
- [43] E. I. Simakov, V. A. Dolgashev, and S. G. Tantawi. "Advances in high gradient normal conducting accelerator structures". In: *Nuclear Instruments and Methods in Physics Research Section A: Accelerators, Spectrometers, Detectors and Associated Equipment* 907 (2018). Advances in Instrumentation and Experimental Methods (Special Issue in Honour of Kai Siegbahn), pp. 221–230. ISSN: 0168-9002. DOI: https://doi.org/10.1016/j.nima.2018.02.0 85.
- [44] A. D. Cahill et al. "High gradient experiments with *X*-band cryogenic copper accelerating cavities". In: *Phys. Rev. Accel. Beams* 21 (10 2018), p. 102002. DOI: 10.1103/PhysRevA ccelBeams.21.102002.
- [45] V. A. Dolgashev et al. "High-gradient rf tests of welded *X*-band accelerating cavities". In: *Phys. Rev. Accel. Beams* 24 (8 Aug. 2021), p. 081002. DOI: 10.1103/PhysRevAccelBeam s.24.081002.
- [46] G. E. H. Reuter, E. H. Sondheimer, and Alan Herries Wilson. "The theory of the anomalous skin effect in metals". In: *Proceedings of the Royal Society of London. Series A. Mathematical and Physical Sciences* 195.1042 (1948), pp. 336–364. DOI: 10.1098/rspa.1948.0123.
- [47] A. H. McEuen et al. "High-Power Operation of Accelerator Structures at Liquid Nitrogen Temperature". In: *IEEE Transactions on Nuclear Science* 32.5 (1985), pp. 2972–2974. DOI: 10.1109/TNS.1985.4334244.
- [48] T. Ohnishi et al. "The SCRIT electron scattering facility project at RIKEN RI beam factory". In: *Physica Scripta* 2015.T166 (2015), p. 014071. DOI: 10.1088/0031-8949/2015/T166/01 4071.

- [49] K. Tsukada et al. "First Observation of Electron Scattering from Online-Produced Radioactive Target". In: *Phys. Rev. Lett.* 131 (9 2023), p. 092502. DOI: 10.1103/PhysRevLett.131. 092502.
- [50] T. Ohnishi et al. "The SCRIT electron scattering facility at RIKEN RI Beam Factory". In: *Nuclear Instruments and Methods in Physics Research Section B: Beam Interactions with Materials and Atoms* 541 (2023), pp. 380–384. ISSN: 0168-583X. DOI: https://doi.org/10.1016/j.nimb.2023.05.038.
- [51] V. Vylet and J. C. Liu. *Radiation protection at high-energy electron accelerators*. SLAC-PUB-9557. Oct. 2002. URL: https://www.slac.stanford.edu/pubs/slacpubs/9500/slac-pub-9557.pdf.
- [52] Istituto Nazionale di Fisica Nucleare (INFN). *FLUKA*. Accessed: 2024-07-21. URL: http://www.fluka.org/fluka.php?id=manuals.
- [53] Radiation Science Center of High Energy Accelerator Research Organization (KEK). *Electron Gamma Shower (EGS) Web Page*. Accessed: 2024-07-21. URL: https://rcwww.kek.jp/research/egs/.
- [54] L. S. Waters et al. "The MCNPX Monte Carlo Radiation Transport Code". In: *AIP Conference Proceedings* 896.1 (Mar. 2007), pp. 81–90. ISSN: 0094-243X. DOI: 10.1063/1.2720 459.
- [55] N. V. Mokhov and C. C. James. *The MARS Code System User's Guide Version 15(2016)*. Feb. 2017. DOI: 10.2172/1462233.
- [56] W. R. Nelson and T. M. Jenkins. *The SHIELD11 Computer Code*. Accessed: 2024-07-21. URL: https://www.slac.stanford.edu/pubs/slacreports/reports15/slac-r-737.pdf.
- [57] C. L. Atwood, J. R. Boland, and P. T. Dickman. *SKYSHIN: A computer code for calculating radiation dose over a barrier*. Nov. 1986. URL: https://www.osti.gov/biblio/7007070.
- [58] Brookhaven National Laboratories: Accelerator Test Facility. *Electron Beam Systems*. https://www.bnl.gov/atf/capabilities/electron-beam-systems.php. Accessed: 2024–03-20.
- [59] D. Kayran and M. Fedurin. *Emittance Measurements*. http://case.physics.stonybrook.ed u/images/7/73/PHY_542_Emittance_Measurements_2023.pdf. Accessed: 2024–03-12. 2023.
- [60] S. G. Biedron et al. "The Operation of the BNL/ATF GUN-IV Photocathode RF Gun at the Advanced Photon Source". In: (1999). URL: https://cds.cern.ch/record/553651.
- [61] A. Adelmann et al. "OPAL a Versatile Tool for Charged Particle Accelerator Simulation". In: *arXiv e-prints* (2019).

- [62] unknown. *Particle nano-Ampere (pnA)*. Accessed: 2024-07-11. URL: https://nukephysik 101.wordpress.com/2018/06/11/.
- [63] G. Machicoane et al. "ARTEMIS-B: A room-temperature test electron cyclotron resonance ion source for the National Superconducting Cyclotron Laboratory at Michigan State University". In: *Review of Scientific Instruments* 77.3 (Mar. 2006), 03A322. ISSN: 0034-6748. DOI: 10.1063/1.2165749.
- [64] S. Schwarz et al. "A high-current electron beam ion trap as a charge breeder for the reacceleration of rare isotopes at the NSCL (invited)". In: *Review of Scientific Instruments* 79.2 (Feb. 2008), 02A706. ISSN: 0034-6748. DOI: 10.1063/1.2801346.

APPENDIX A: BEAM PROFILE IMAGES

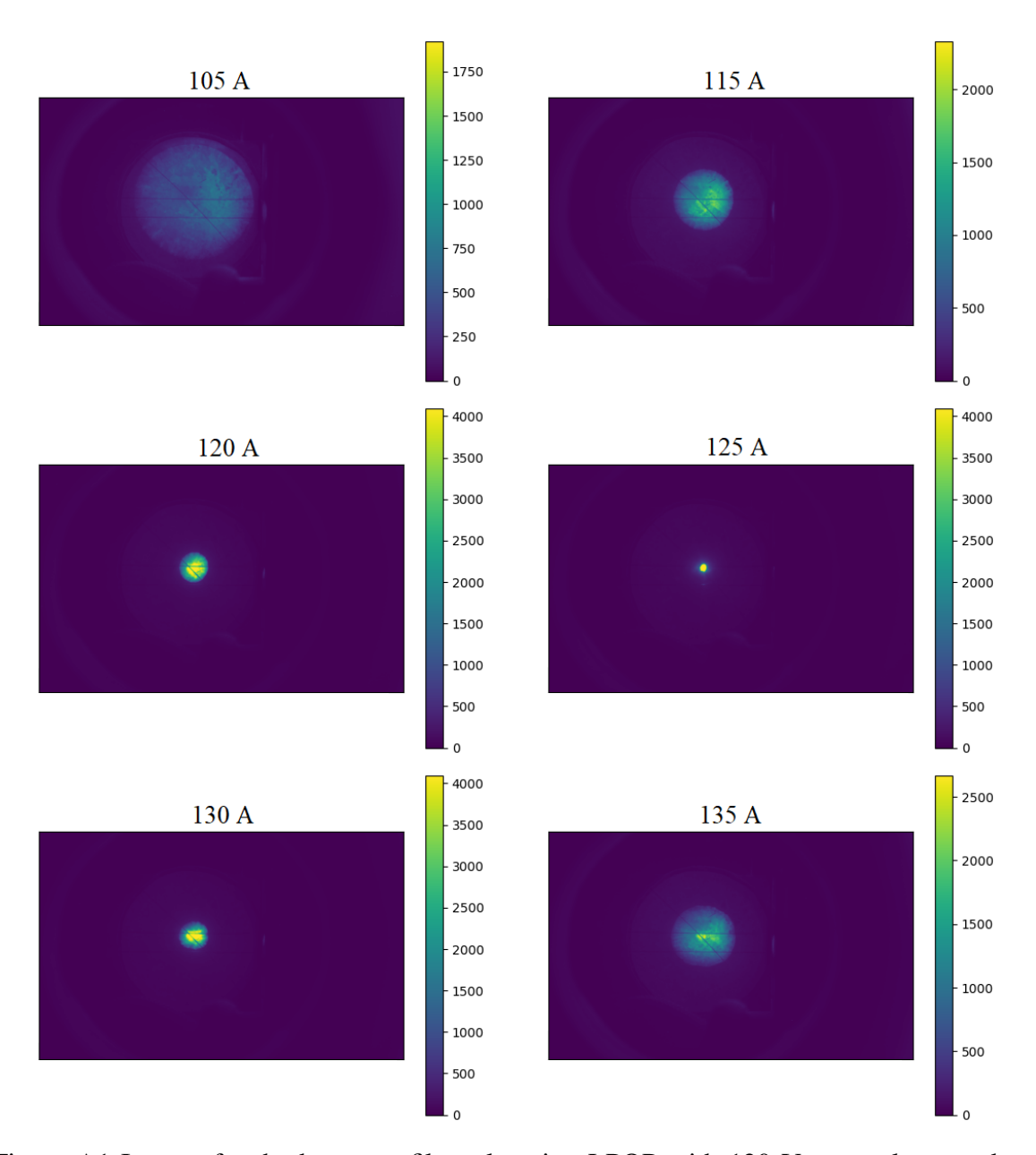


Figure A1 Images for the beam profile at location LPOP with 120 V gun voltage and 10° phase, an average laser power of $\approx 30~\mu J$ and varying solenoid current as indicated in the title of each image.

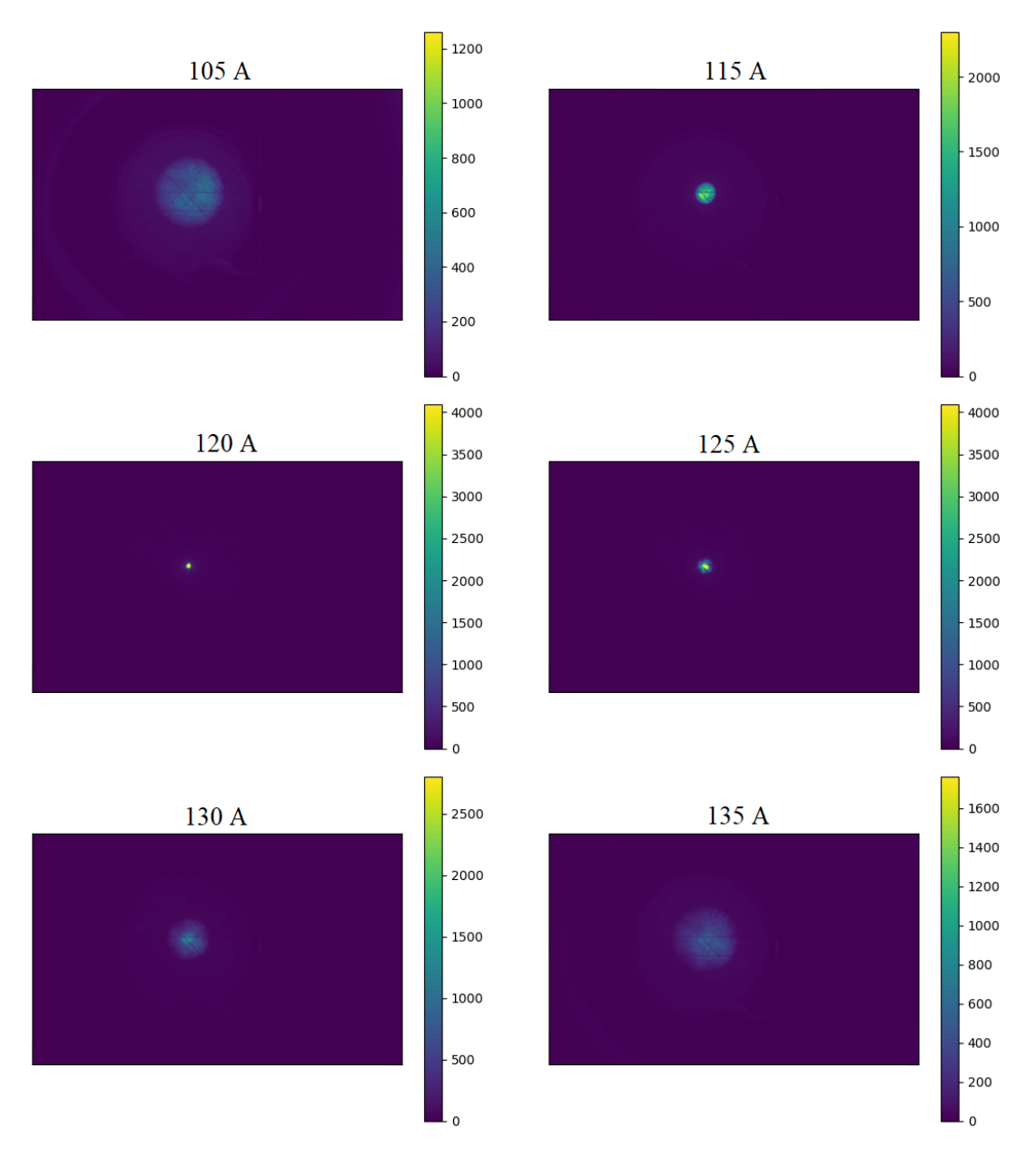


Figure A2 Images for the beam profile at location LPOP with 120 V gun voltage and -19° phase, an average laser power of $\approx \! \! 30~\mu J$ and varying solenoid current as indicated in the title of each image.

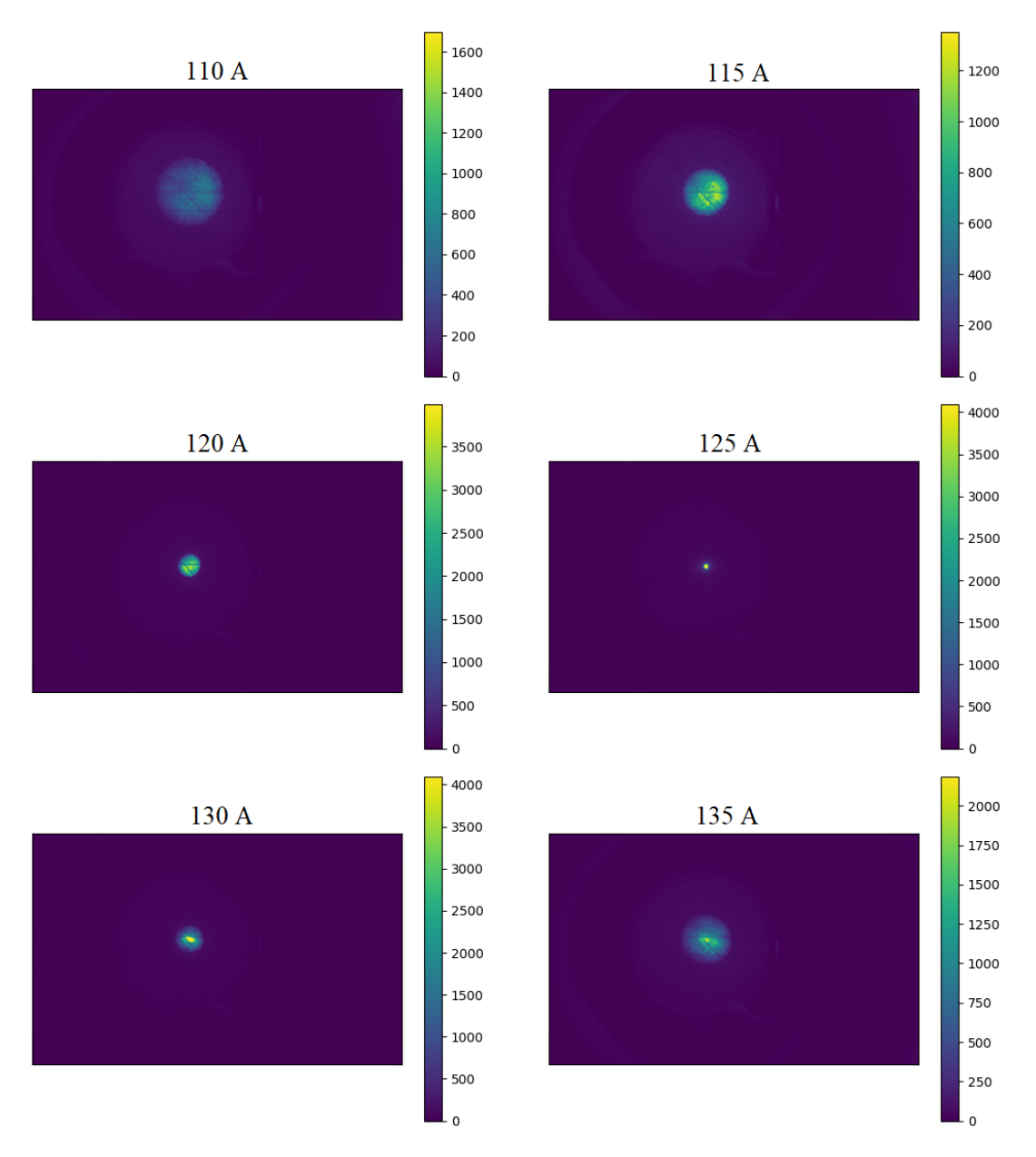


Figure A3 Images for the beam profile at location LPOP with 120 V gun voltage and 0° phase, an average laser power of $\approx 30~\mu J$ and varying solenoid current as indicated in the title of each image.

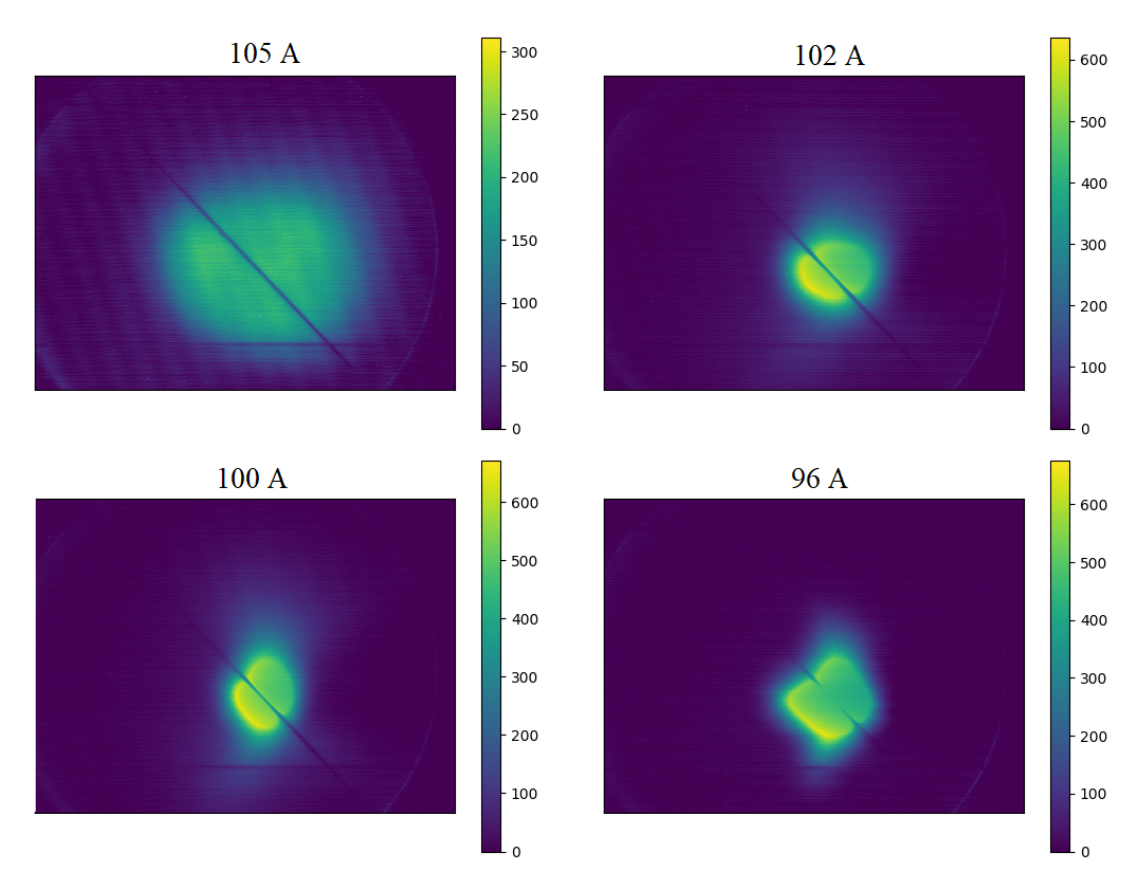


Figure A4 Images for the beam profile at location HPOP1 with 120 V gun voltage and 25° phase, an average laser power of $\approx 28~\mu J$ and varying solenoid current as indicated in the title of each image.

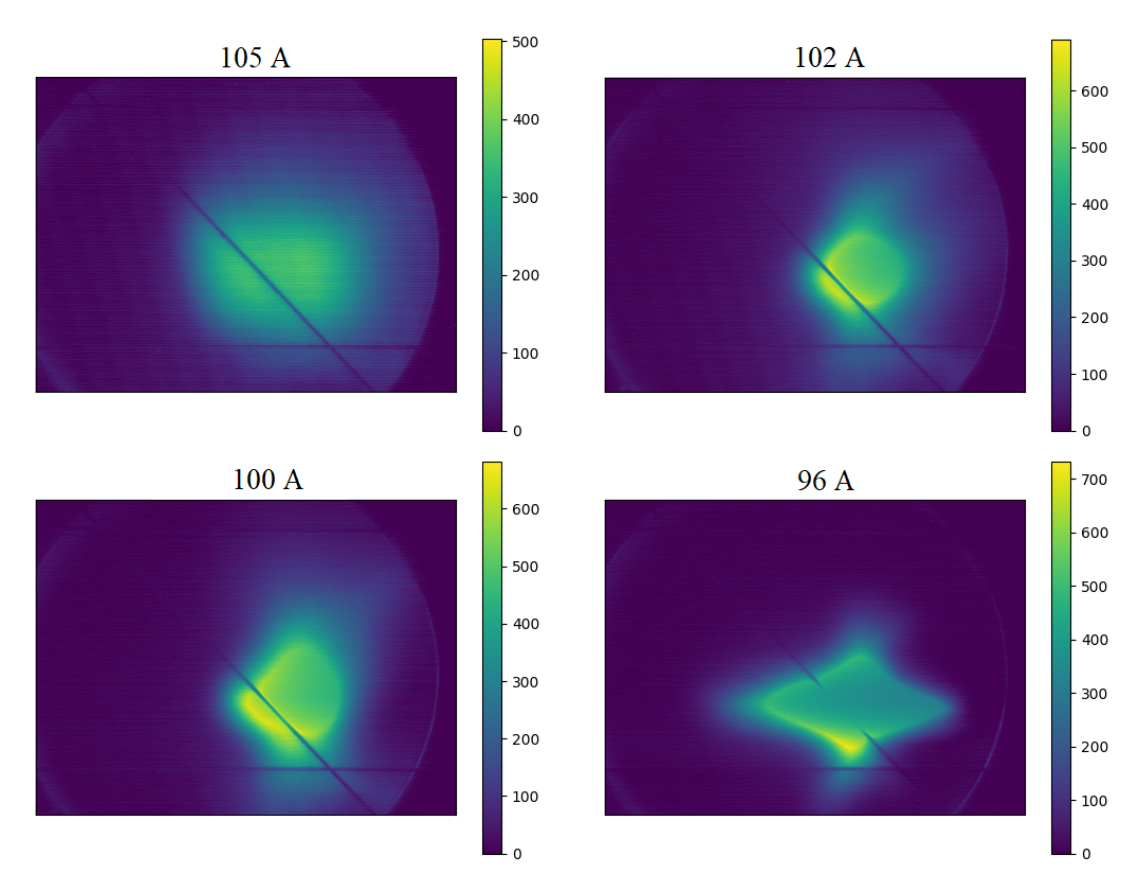


Figure A5 Images for the beam profile at location HPOP1 with 120 V gun voltage and 35° phase, an average laser power of \approx 28 μ J and varying solenoid current as indicated in the title of each image.

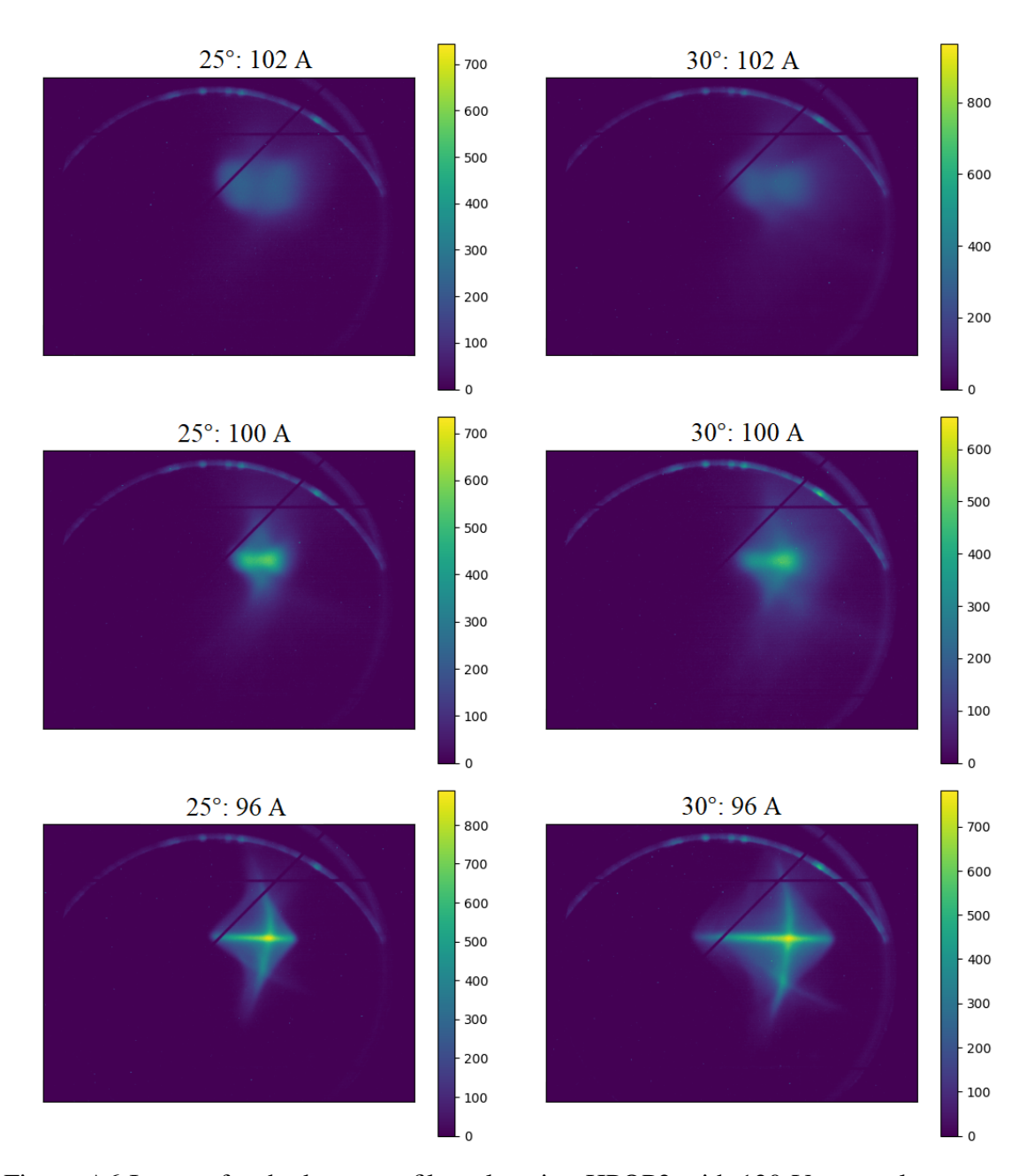


Figure A6 Images for the beam profile at location HPOP2 with 120 V gun voltage, an average laser power of \approx 28 μ J, and varying solenoid current and RF phase as indicated in the title of each image.

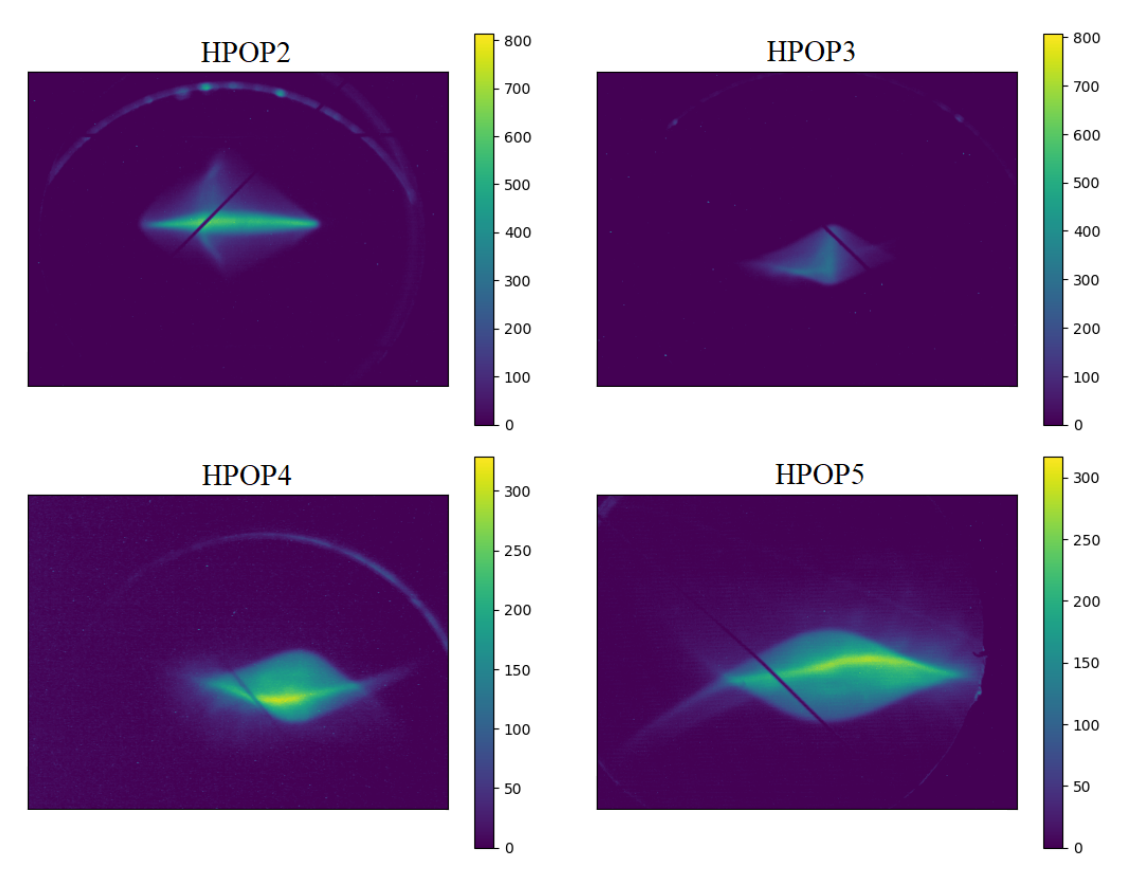


Figure A7 Images for the beam profile at different locations indicated in the title of each image with 120 V gun voltage and 31° phase, an average laser power of $\approx 30~\mu J$ and 96 A solenoid current.

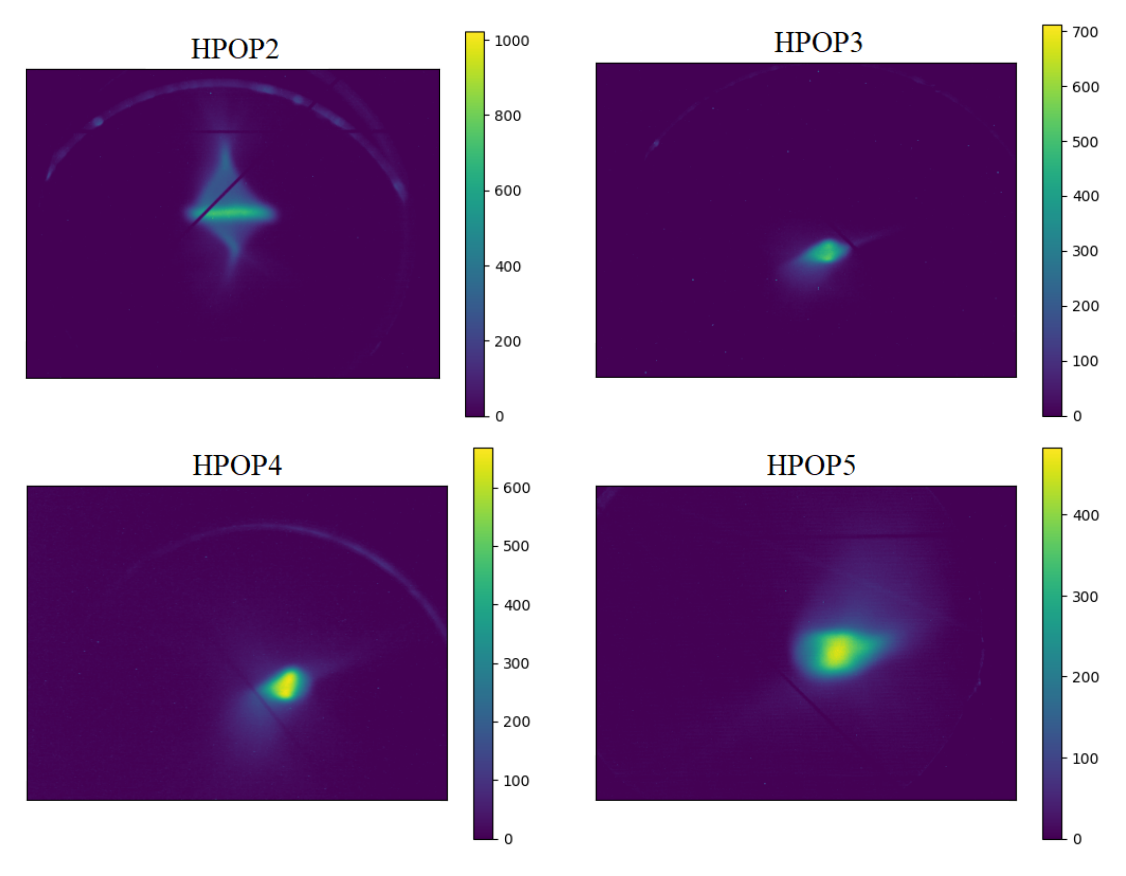


Figure A8 Images for the beam profile at different locations indicated in the title of each image with 120 V gun voltage and 31° phase, an average laser power of $\approx 30~\mu J$ and 100 A solenoid current.

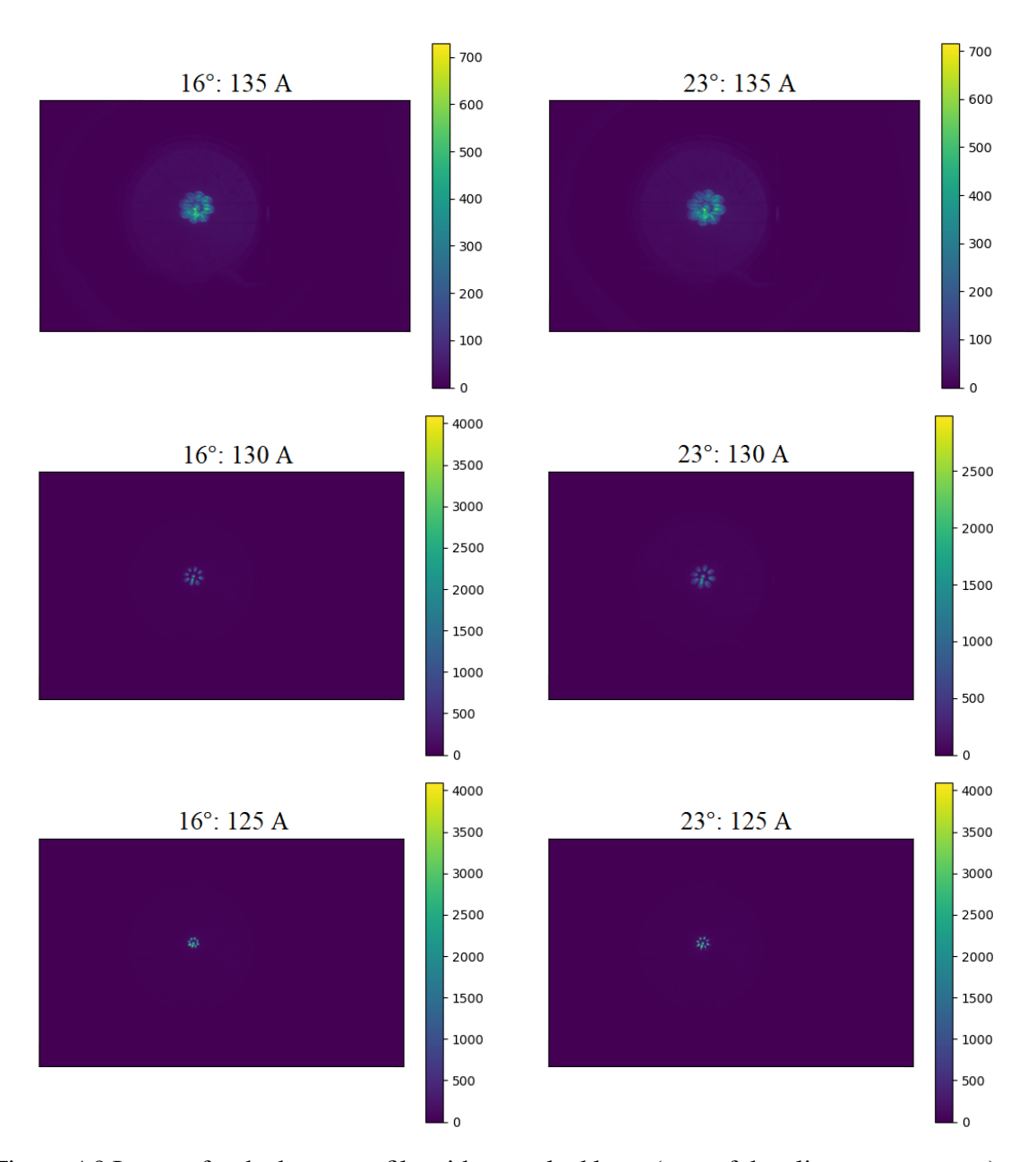


Figure A9 Images for the beam profile with a masked laser (part of the alignment process) at location LPOP with 120 V gun voltage, an average laser power of $\approx 1.8~\mu J$, and varying solenoid current and RF phase as indicated in the title of each image.

APPENDIX B: CODES

OPAL template file for simulation

```
Title, string="ATF Gun and Linac";
REAL bf = 2856.0;
REAL IHQ1 = 7;
REAL IHQ2 = -6;
REAL IHQ3 = 6;
REAL gunphase = 0.05236;
REAL accelphase = 25.0;
REAL accelvolt = 120.0;
REAL beamcurrent = 2.459345657376521e-08;
REAL solcurrent = 96.0;
"OPT1": option, autophase=4.0, psdumpfreq=50.0, statdumpfreq=1.0, version
\hookrightarrow =10900.0;
"D1": DRIFT, 1=0.18;
"D2": DRIFT, 1=0.042;
"D3": DRIFT, 1=0.05;
"D4": DRIFT, 1=0.20;
"D5": DRIFT, 1=0.17;
"D6": DRIFT, 1=0.20;
"D7": DRIFT, 1=0.20;
"D8": DRIFT, 1=0.17;
"LPOP1": MONITOR, OUTFN="LPOP1f";
"HPOP1": MONITOR, OUTFN="HPOP1f";
"HPOP2": MONITOR, OUTFN="HPOP2f";
"ATF_RFGUN": RFCAVITY, fmapfn="DriveGun.T7", freq=BF, l=0.15, lag=gunphas

    e,type=STANDING,volt=100.0;

"ATF_SOLENOID":
SOLENOID, fmapfn="ATFsolenoidFmap.T7", ks=solcurrent, l=0.42756;
"GUNSOURCE": SOURCE;
```

```
"LINACRF_T1": TRAVELINGWAVE,apveto=true,designenergy=25.0,fmapfn="tws;
\rightarrow _slac_s.T7",freq=2856.0,l=3.0,

    lag=accelphase,mode=0.6666666666666666,numcells=84.0,volt=accelvolt;
"LINACRF_T2": TRAVELINGWAVE,apveto=true,designenergy=55.0,fmapfn="tws_
\rightarrow _slac_s.T7", freq=2856.0, l=3.0,

    lag=accelphase,mode=0.6666666666666,numcells=84.0,volt=accelvolt;
"HQ1": QUADRUPOLE, L=0.1, K1=IHQ1*1.2264;
"HQ2": QUADRUPOLE, L=0.2, K1=IHQ2*1.2264;
"HQ3": QUADRUPOLE, L=0.1, K1=IHQ3*1.2264;
"GUNSOURCE#0": "GUNSOURCE",elemedge=0;
"ATF_RFGUN#0": "ATF_RFGUN",elemedge=0;
"ATF_SOLENOID#0": "ATF_SOLENOID", elemedge=0.15;
"D1#0": "D1",elemedge=0.57756;
"LPOP1#0": "LPOP1",elemedge=0.75756;
"D2#0": "D2",elemedge=0.75756;
"LINACRF_T1#0": "LINACRF_T1", elemedge=0.79956;
"D3#0": "D3",elemedge=3.79956;
"LINACRF_T2#0": "LINACRF_T2", elemedge=3.84956;
"D4#0": "D4",elemedge=6.84956;
"HPOP1#0": "HPOP1".elemedge=7.04956;
"D5#0": "D5", elemedge=7.04956;
"HQ1#0": "HQ1", elemedge=7.21956;
"D6#0": "D6",elemedge=7.31956;
"HQ2#0": "HQ2", elemedge=7.51956;
"D7#0": "D7",elemedge=7.71956;
"HO3#0": "HO3".elemedge=7.91956;
"D8#0": "D8",elemedge=8.01956;
"HPOP2#0": "HPOP2", elemedge=8.18956;
//"FILTR1": FILTER, TYPE="RELATIVEFFTLOWPAS", THRESHOLD=0.01;
//"WAKEFIELD": WAKE, TYPE="1D-CSR-IGF", NBIN=20, FILTERS="FILTR1";
"FS1": fieldsolver,bboxincr=1.0,fstype="FFT",mt=32.0,mx=16.0,my=16.0,

    parfftx=true,parffty=true;
```

```
"DIST1": distribution, ekin=0.4, emissionmodel="ASTRA", emissionsteps=20
    \rightarrow maxstepssi=500.0,nbin=5.0,sigmat=0.0006,sigmax=0.0028,sigmay=0.001
    \rightarrow 28,tfall=2.45e-12,

    tpulsefwhm=5.04e-12,trise=2.45e-12,type="GUNGAUSSFLATTOPTH";

    "BEAM1": beam,bcurrent=beamcurrent,bfreq=BF,npart=45000.0,particle="E_

    LECTRON",pc=P0;

    "T1": track,beam=beam1,dt=1e-11,line=Injector,maxsteps=30000.0,zstop=1
    \hookrightarrow 10.0;
   run,

→ beam=beam1, distribution=Dist1, fieldsolver=Fs1, method="PARALLEL-T";

   endtrack;
  Python code to generate simulated data from experimental parameters
#Reading the parameters for the simulation from files saved in the folder
# under the names of "folder_name_experimentalData", and executing
# sequences of the variables ['ID_run', 'rfphase', 'rfpower', 'sol', 'laser'].
#The file "nameofSimulationFile", that must be saved in the same
→ directory as this running file,
# will be taken as the template for the OPAL simulation ".in" file.
#IMPORTS
import pandas as pd
import os
import re
import numpy as np
from math import pi, floor, log10
import shutil
from datetime import datetime
from pytz import timezone
```

#GLOBAL VARIABLES ------

```
#example for experimental files: 20240321104718_hpop2_rfphase_31.0deg_rfp|
→ ower_0.00dB_sol_96.0A_laser_30.98uJ_LT1HX_0.350A_0
#Constants related to OPAL files
searchword1 = "accelphase = 25.0"
searchword2 = "accelvolt = 120.0"
searchword3 = "solcurrent = 96.0"
searchword4 = "beamcurrent = 2.459345657376521e-08"
searchword5 = "LPOP1f"
searchword6 = "HPOP1f"
searchword7 = "HPOP2f"
samplefilename = "/home/sirepo_user/OPAL/Ambar/fromExperim/Simulation_202_
                        → OPAL FILE*****************
#Constants related to experimental file manipulation
x_{variables} = [] #we will store the numbers found in the files here,
folder_name_experimentalData = ['20240301',
→ '20240304','20240305','20240321'] #The first two, 2024030 and
→ 20240304, contain only LPOP, thus will be
   # used for average beam profile and radii comparison. The third has
   # before and after acceleration images, and will be used for
   # and beam profile, in both locations. Finally, 20240321, has only
   # measurements after acceleration that will be used for emittance
   \hookrightarrow calculation.
c = 299792458 \ \#m/s
mkg = 9.1093837e-31 \#kg
h = 6.62607015e-34 \#J/Hz
q_e = 1.602176634e-19 \#C
                         ate ate ate ate
#Start loop to read different groups of folder. See more information
\hookrightarrow further up.
for 1 in range(len(folder_name_experimentalData)):
```

```
dir_expData = '/home/sirepo_user/MeasurementsATF/' +
outfiledir =

→ '/home/sirepo_user/OPAL/Ambar/fromExperim/Simulation_20240523/'

#FUNCTIONS ------
def Get_experimentalNumbers(file_name, ID):
 # Regular expression pattern to extract numeric values after specific
  \hookrightarrow keywords
 pattern1 = r"rfphase_([\d.]+).*rfpower_([\d.]+).*sol_([\d.]+).*laser_{-}
  pattern2 = r"rfphase\_-([\d.]+).*rfpower\_([\d.]+).*sol\_([\d.]+).*laser_+
  pattern3 = r''([hl])pop(\d+)''
 pattern4 = r''([HL])POP(\d+)''
 values1 = re.search(pattern1, file_name)
 if not values1:
   values1 = re.search(pattern2, file_name)
 if values1:
   values2 = re.search(pattern3, file_name)
   if not values2:
     values2 = re.search(pattern4, file_name)
   if values2:
      numeric_values = ([ID] + [values1.group(j) for j in range(1,
       else:
     numeric_values = 0
 else:
   numeric_values = 0
 return numeric_values
def SearchforANDchageWord(filename, searchword, newword):
 with open(filename, 'r') as file:
   data = file.read()
   data = data.replace(searchword, newword)
 with open(filename, 'w') as file:
   file.write(data)
```

```
return
```

```
def GenerateNewFile(samplefile, newname):
  src = samplefile
 dest = newname
 doCopy = shutil.copyfile(src,dest)
 return
def Average_oneVarinList(variable_list, n):
 new_list = variable_list.copy()
 # Extract the number from each sublist
 numbers = [sublist[n] for sublist in variable_list]
 # Calculate the average
 if len(numbers) > 0:
     average = sum(numbers) / len(numbers)
 else:
     average = None
 for i in range(len(new_list)):
   new_list[i][n] = average
 return new list
#GETTING VARIABLES ------
#The laser variation is used to account for statistical error (we don't

→ want simulations to vary in number

# of electrons). We will make an average and save that for all sets in

    ← the list, and trim again the set of

# unique permutations to simulate.
#Reading files
     #********* (missing in
      → putty format)
dir_list = os.listdir(dir_expData)
i = 0
for file name in dir list:
 if file_name.endswith(".asc"):
   x_variables_thisFile = Get_experimentalNumbers(file_name, i)
   if x_variables_thisFile:
     x_variables.append(x_variables_thisFile)
     i+=1
```

```
print("Exracted array of variables:\n", x_variables)
#Code to filter and save only the unique sequences in the lists saved

    in x_variables

x_var_IDonly = []
for i in range(len(x_variables)):
  x_var_IDonly.append(x_variables[i][1:5])
unique_sequences = set()
x_unique = []
for seq in x_var_IDonly:
    seq_tuple = tuple(seq)
    if seq_tuple not in unique_sequences:
        unique_sequences.add(seq_tuple)
        x_unique.append(seq)
num_files = len(x_unique)
#Converting units from saved in file to used by OPAL
for i in range(num_files):
  x_unique[i][1] = 10**(float(x_unique[i][1])/20) * 120
  \leftarrow #conversion from dB to volts dB = 20*log(volts/ref_volts), where
  \hookrightarrow ref_volts = 120 MV
  E_{phot} = c*h/265e-9
  num_phot = float(x_unique[i][3])*1e-6/E_phot #The energy of laser is

    provided in microJoules

  x_{unique}[i][3] = (num_phot * 0.0035) * q_e  #conversion from
  \rightarrow laser power to current; assuming QE = 0.0035 = #elect/#photons,
  \rightarrow AND E_phot=c*h/lambda, lambda = 265nm AND q_e=1.602176634e-19
  n = 3
         #The index number for the beam current (in x_unique) to be set
→ as constant for the simulation of this folder
x_unique = Average_oneVarinList(x_unique, n)
unique_sequences = set()
x_unique_new = []
for seq in x_unique:
    seq_tuple = tuple(seq)
    if seq_tuple not in unique_sequences:
        unique_sequences.add(seq_tuple)
        x_unique_new.append(seq)
num_files = len(x_unique_new)
x_unique = x_unique_new
print("Number of unique permutations of variables:", num_files)
print("Unique data sets to be simulated:\n", x_unique)
```

```
#LOOP THAT GENERATES INPUT FILES, RUN OPAL SIMULATION AND SAVE INFO TO
\hookrightarrow TABLE -----
referencefile = "ReferenceTable.txt"
hs = open(referencefile, "a")
tz = timezone('US/Eastern')
current_time = datetime.now(tz)
line = str(current_time) +'\n'
hs.write(line)
line = "LinacPhase1 \t LinacPhase2 \t GunPhase \t SolenoidCurrent \t
hs.write(line)
hs.close()
for i in range(num_files):
  #Generating new names
 dataID = str(x_unique[i][0])+"_"+str(x_unique[i][1])+"_"+str(x_unique[i][1])
  dataID = dataID.replace('.', 'dot')
 dataID = dataID.replace('-', 'pow')
 infilename = "ATFlinac" + dataID + ".in"
 newphase = "Accelphase = " + str(x_unique[i][0])
 newpower = "Accelvolt = " + str(x_unique[i][1])
 newScurrent = "solcurrent = " + str(x_unique[i][2])
 newBcurrent = "beamcurrent = " + str(x_unique[i][3])
 newmonitor1 = searchword5 + dataID
 newmonitor2 = searchword6 + dataID
 newmonitor3 = searchword7 + dataID
  #Running functions
 GenerateNewFile(samplefilename, infilename)
 SearchforANDchageWord(infilename, searchword1, newphase)
 SearchforANDchageWord(infilename, searchword2, newpower)
 SearchforANDchageWord(infilename, searchword3, newScurrent)
 SearchforANDchageWord(infilename, searchword5, newmonitor1)
  SearchforANDchageWord(infilename, searchword6, newmonitor2)
 SearchforANDchageWord(infilename, searchword7, newmonitor3)
```

#Run opal simulation

```
outfilename = outfiledir + "outfile.out"
command = "opal "+ infilename + ' > ' + outfilename
print("\n0pal simulation started, with command: ", command)
os.system(command)
print("Opal simulation ended, count: ", i+1, ", with values")
print("\t linac phase:", x_unique[i][0], ",\t linac power:",

    x_unique[i][1], ",\t solenoid current:", x_unique[i][2], ",\t

    beam current:", x_unique[i][3])

print("\tThe corresponding unique ID:", dataID)
#Save details to table
hs = open(referencefile, "a")
line = str(x_unique[i][0])+"\t"+str(x_unique[i][1])+"\t"+str(x_unique
\rightarrow [i][2])+"\t"+str(x_unique[i][3]) + "\t" + newmonitor1 + ".h5
\hookrightarrow \n"
hs.write(line)
hs.close()
```

Python code to read experimental data and determine the beam's radii

```
#Script to sequentally read a collection of ascii monitor data (filename
# example: #ID_{EXP_CONDTS}_HPOP#ID.amf, where the #ID of the images for
# emittance measuremeants in folder 202403, and {EXP_CONDTS} is replaced
\hookrightarrow by rf
# phase, rf power, laser power, solenoid current). It then crops to
# the beam edges, assuming that is wherever the count is less than
# current_tolerance% of maximum average count. Here the count is taken as
# electron current.
#TMPORTS
import numpy as np
import pandas as pd
from math import pi,sin, cos, exp, sqrt, floor
import matplotlib.pyplot as plt
import matplotlib.image as im
import scipy
```

```
from google.colab import drive
import os
import shutil
import h5py as h5
import collections.abc
import re
#GLOBAL VARIABLES
#example file: 20240321104718_hpop2_rfphase_31.0deg_rfpower_0.00dB_sol_96
→ .0A_laser_30.98uJ_LT1HX_0.350A_0
plot_bool = 1  #boolean to decide to plot of not the trimmed radius
current_tolerance = 0.35 #*** We are assuming that the beam ends where
\hookrightarrow the everage pixel count drops 65% from the average maximum
x_variables_names = ['ID_run', 'rfphase', 'rfpower', 'sol', 'laser',
→ 'JPOP', 'POPN'] #the unique ID by which each run is saved as, the
→ RF phase and power for the acceleration cavities, the current at the

    → focusing solenoids, and the laser power in the photocathode

y_variables_names = ['r_x', 'r_y', 'r_ms', 'center_x', 'center_y']
x_variables = []
y_variables = []
folder_names = ['20240301']
c = 299792458 \ \#m/s
mkg = 9.1093837e-31 \#kg
meV = 0.5109989461e6 \#eV
#FUNCTIONS
def get_avergMax(n, data):
  #assuming data is pandas dataframe
 values_series = data.stack()
 highest_values = values_series.nlargest(n).tolist()
 average = np.mean(highest_values)
```

```
return average
```

```
def find_edges(image, percent):
  len_y, len_x = image.shape
  steps_y, steps_x = floor(len_y/3), floor(len_x/3)
  currMax = get_avergMax(100, image) #Saving the average high beam
  tolerance = currMax * percent #We are assuming that the whatever signal

→ is below percent (70%) of the maximum is background

 beam_x = [] #Here we'll save the indeces for which the current in that
  → row (horizontal) was above tolerance
 beam_y = [] #Here we'll save the indeces for which the current in that
  → column (vertical) was above tolerance
  for i in range(steps_x):
   n_largest_values_i = image.iloc[:, i*3].nlargest(10)
   max_value_column = np.mean(n_largest_values_i.values)
   if max_value_column >= tolerance:
     beam_x.append(i*3)
  for j in range(steps_y):
   n_largest_values_j = image.iloc[j*3, :].nlargest(10)
   max_value_row = np.mean(n_largest_values_j.values)
   if max_value_row >= tolerance:
     beam_y.append(j*3)
 return beam_x, beam_y
def edges_are_different(image, tolerance):
 boolean = 0
  lenx, leny = image.shape
  avrg_ax1_0 = np.mean(image.iloc[:, 5])
  avrg_ax1_n = np.mean(image.iloc[:, leny-5])
  avrg_ax2_0 = np_mean(image_iloc[5, :])
 avrg_ax2_n = np.mean(image.iloc[lenx-5, :])
 ratio_ax1 = avrg_ax1_0/avrg_ax1_n
 if ratio_ax1 > 1:
   ratio_ax1 = avrg_ax1_n/avrg_ax1_0
 ratio_ax2 = avrg_ax2_0/avrg_ax2_n
 if ratio_ax2 > 1:
   ratio_ax2 = avrg_ax2_n/avrg_ax2_0
 if ratio ax1 <= tolerance or ratio ax2 <= tolerance:</pre>
   boolean = 1
 return boolean
def cut_unmatched_ax(image, tolerance, n):
  #finding average values of current at each end of each axis
  lenx, leny = image.shape
```

```
avrg_ax1_0 = np.mean(image.iloc[:, 5])
  avrg_ax1_n = np.mean(image.iloc[:, leny-5])
  avrg_ax2_0 = np.mean(image.iloc[5, :])
  avrg_ax2_n = np.mean(image.iloc[lenx-5, :])
  ratio_ax1 = avrg_ax1_0/avrg_ax1_n
  if ratio_ax1 > 1:
    ratio_ax1 = avrg_ax1_n/avrg_ax1_0
  ratio_ax2 = avrg_ax2_0/avrg_ax2_n
  if ratio ax2 > 1:
    ratio_ax2 = avrg_ax2_n/avrg_ax2_0
  #cutting axis below tolerance at the edge with lowest average current

    value

  if ratio_ax1 <= tolerance:</pre>
    if avrg_ax1_0 < avrg_ax1_n:</pre>
      beam_image_cut = image.iloc[:, n:]
    else:
      beam_image_cut = image.iloc[:, :leny-n]
  if ratio_ax2 <= tolerance:</pre>
    if avrg_ax2_0 < avrg_ax2_n:</pre>
      beam_image_cut = image.iloc[n:, :]
    else:
      beam_image_cut = image.iloc[:lenx-n, :]
  return beam_image_cut
def get_y_variables(beam_image, ax1, ax2, Cam_resol):
  #Getting radius, center_x, center_y
  center_x, center_y = int((beam_y[0]+beam_y[-1])/2)* Cam_resol,
  \rightarrow int((beam_x[0]+beam_x[-1])/2)* Cam_resol
  len_x, len_y = beam_image.shape
  r_x, r_y = (len_x/2*Cam_resol), (len_y/2*Cam_resol)
  radius = sqrt((r_x**2 + r_y**2)/2)
  y_var = [r_x, r_y, radius, center_x, center_y]
  return y_var
#DATA HANDLING
drive.mount('/content/drive')
for this_folder in folder_names:
  dir = '/content/drive/My Drive/Codigos/ExperData/' + this_folder
```

```
dir_list = os.listdir(dir)
i = 1
for file_name in dir_list:
  if file_name.endswith(".asc"):
    #Load individual image data
    full_path = dir + '/' + file_name
    beam_image = pd.read_csv(full_path)
    #Regular expression pattern to extract numeric values after
    pattern1 = r"rfphase\_([\d.]+).*rfpower\_([\d.]+).*sol\_([\d.]+).*lase_{|}
    \hookrightarrow r_([\d.]+)"
    pattern2 = r''([hl])pop(\d+)''
    pattern3 = r''([HL])POP(\d+)''
    pattern4 = r"rfphase\_-([\d.]+).*rfpower\_([\d.]+).*sol\_([\d.]+).*las_{|}
    \hookrightarrow er_([\d.]+)"
    values1 = re.search(pattern1, file_name)
    if not values1:
      values1 = re.search(pattern4, file_name)
    if values1:
      #Looking for beam edges and cutting
      beam_x, beam_y = find_edges(beam_image, current_tolerance)
      cols, rows = len(beam_x), len(beam_y)
      beam_image_cut = beam_image.iloc[beam_y[0]:beam_y[-1],
      \rightarrow beam_x[0]:beam_x[-1]]
      #Verifying for outlier
      cut_lenx, cut_leny = beam_image_cut.shape
      \#abs(beam_x[0]-beam_x[-1]), abs(beam_y[0]-beam_y[-1])
      if cut_lenx > 250 or cut_leny > 65:
        edges_ratio_tolerance = 0.4
        if edges_are_different(beam_image_cut, edges_ratio_tolerance):
          print("This image was trimmed twice")
          beam_image_cut =
          cut_unmatched_ax(beam_image_cut,edges_ratio_tolerance, 25)
          beam_x, beam_y = find_edges(beam_image_cut, .50)
          beam_image_cut = beam_image_cut.iloc[beam_y[0]:beam_y[-1],
          \rightarrow beam_x[0]:beam_x[-1]]
          cut_lenx, cut_leny = abs(beam_x[0]-beam_x[-1]),
          \rightarrow abs(beam_y[0]-beam_y[-1])
      #Evaluate and save values for x_variables and y_variables
      values2 = re.search(pattern2, file_name)
      if not values2:
        values2 = re.search(pattern3, file_name)
```

```
x_variables_thisFile = ([i] + [float(values1.group(j)) for j in
\rightarrow range(1, 5)] + [values2.group(1), values2.group(2)])

    #x_variables = ['ID_run', 'rfphase', 'rfpower', 'sol', 'laser',

\hookrightarrow 'JPOP', 'POPN']
if x_variables_thisFile[5] == 'h' or x_variables_thisFile[5] ==

    'H':

           #every pixel has a resolition of approximately 15e-6

→ [m] for HPOPs and...
 y_variables_thisFile = get_y_variables(beam_image_cut, beam_x,
  \rightarrow beam_y, 15e-6) #y_variables = ['r_x', 'r_y', 'r_ms',
  elif x_variables_thisFile[5] == 'l' or x_variables_thisFile[5]
← == 'L': #...approximately 50e-6 [m] pixel resolution for
\hookrightarrow LPOPs
 y_variables_thisFile = get_y_variables(beam_image_cut, beam_x,
  \rightarrow beam_y, 50e-6)
x_variables.append(x_variables_thisFile)
y_variables.append(y_variables_thisFile)
i+=1
#Print the information and plot the image
print('\n')
table = 'Values for' + file_name + ':\n\t'
for var in range(len(x_variables_names)):
 table = f'{table}{x_variables_names[var]} \t
  for var in range(len(y_variables_names)):
 table = f'{table}{y_variables_names[var]} \t
  print(table)
if plot_bool:
 imshow = plt.imshow(beam_image_cut)
 plt.colorbar(imshow)
 title = "Automated crop around beam edges [x:" + str(cut_lenx)
  plt.title(title)
 plt.show()
```

Python code to determine emittance from experimental data

```
#This script assumes that one of the codes in the previous section has \hookrightarrow been run.
#It takes:
```

```
# x_variables = ['ID_run', 'rfphase', 'rfpower', 'sol', 'laser', 'JPOP', 'POPN']
# y_variables = ['r_x', 'r_y', 'r_ms', 'center_x', 'center_y']
# and calculates the emittance.
#IMPORTS
import numpy as np
import matplotlib.pyplot as plt
from math import pi,sin, cos, exp, sqrt, floor
from scipy.optimize import minimize
import re
#GLOBAL VARIABLES
#We assume that the minimum of beta is located somewhere between the
→ HPOP3 and HPOP4
plot_bool = 1  #boolean to decide to plot of not the trimmed radius
si_HPOPs = {2:8.545, 3:12.052, 4:13.176, 5:14.653} #location of the
\hookrightarrow HPOP[2,3,4,5] in the beamline in meters
       #location in the x variable for JPOP
r = [2, 3, 4] #locations for the r measurement in the value arrays of

    dictionaries → key:[JPOP,POPN,{y_variables}]

r_{measured} = ['x', 'y', 'rms']
all_sigma_s = {} #all the 4-tuple combinations of the beam radii and
\hookrightarrow position data { ID:[[{rx_data}], [{ry_data}], [{rms_data}]], ID:[[]],
→ ...}; each ri_data has lx4 number of [sigma,s] pairs, where 1
→ correspond to the number of minimum data arrays in the NPOP dictionary
all_emmitance_eq = {} #the results of optimized [emittance, beta0, s0]
\hookrightarrow for all the 4-tuple pictures of the beam.
c = 299792458 \ \#m/s
mkg = 9.1093837e-31 \#kg
```

meV = 0.5109989461e6 #eV

```
#FUNCTIONS
```

```
def emittance_functn(params, sigma, s):
  emittance, beta0, s0 = params
 predicted_sigma = np.sqrt(abs(emittance * (beta0 + (s - s0)**2 /
  \rightarrow beta0)))
 return np.sum((sigma - predicted_sigma)**2)
def find_min_number(lst):
    if all(x == lst[0] for x in lst):
        return lst[0]
    else:
        return min(lst)
#CALCULATING
#Saving the results of radii (sigma) and location (s), in groups of 4, as
# measured experimentally.
grouped_x_y = [] #x_variables + y_variables = [['ID_run', 'rfphase',

    'rfpower', 'sol', 'laser', 'JPOP', 'POPN', 'radius', 'center_x', 'center_y']]

dict_x_y = \{\} #{[ID]:[values],...} = {['rfphase', 'rfpower', 'sol',
→ 'laser']:[['JPOP', 'POPN', 'radius', 'center_x', 'center_y']]}
n0, n1, n2, n3 = 1, J-1, J, (J + len(y_variables_names))
                                                            #values for
→ ID of run and the new y_variables which include JPOP and NPOP
\# ID = x[n0:n1], AND values = x[n2:n3]
#Create grouped array
for 1 in range(len(x_variables)):
  grouped_x_y.append(x_variables[1] + y_variables[1])
#Create dictionary
for x in grouped_x_y:
 ID = tuple(x[n0:n1])
 value = x[n2:n3]
 if ID in dict_x_y:
    dict_x_y[ID].append(value)
 else:
    dict_x_y[ID] = [value]
```

```
print("Unique IDs in the data:")
print(dict_x_y.keys())
#Sorting information into groups of 4 consecutive measurements
for key in dict_x_y.keys():
 \hookrightarrow 0.0008100000000000001, 0.0008611946644052087], [], ... []]
 NPOPs_dict = {}
  for sublist in y_arrays:
     N = int(sublist[1])
     if N in NPOPs_dict:
       NPOPs_dict[N].append(sublist)
     else:
       NPOPs_dict[N] = [sublist]
 len_Ns = []
  for N in NPOPs_dict.keys():
      len_Ns.append(len(NPOPs_dict[N]))
 if len(len_Ns) == 4:
   1 = find_min_number(len_Ns)
   sigmas_s = {ri:[] for ri in r_measured}
    for i in range(1):
      for N in NPOPs_dict.keys():
         Ni_array = NPOPs_dict[N]
         Ni_array = Ni_array[i]
         s = si_HPOPs.get(N)
         sigmas_s[r_measured[0]].append([Ni_array[r[0]], s])
         sigmas_s[r_measured[1]].append([Ni_array[r[1]], s])
         sigmas_s[r_measured[2]].append([Ni_array[r[2]], s])
   all_sigma_s[key] = [sigmas_s[r_measured[0]], sigmas_s[r_measured[1]],
    \hookrightarrow sigmas_s[r_measured[2]]]
#Print result of grouping of information
print("\nResult for all_sigma_s")
for key in all_sigma_s.keys():
 print(' KEY:', key)
 print(' values:', all_sigma_s[key])
 value = all_sigma_s[key]
 print(' rx: values[0][0]:', value[0][0])
 print(' ry: values[1][0]:', value[1][0])
 print(' rms: values[2][0]:', value[2][0])
  sigmas = value[0][0:4]
  sigmas = [item[0] for item in sigmas]
 print(" First 4-tuple of sigmas:", sigmas)
#Perform optimization and save results of fitted parabola
num_of_samples = int(len(value[0])/4)
```

```
for key in all_sigma_s.keys():
 values = all_sigma_s[key]
  for i in range(len(r)):
    for j in range(num_of_samples):
      sigma = values[i][j:j+4]
      sigma = np.array([item[0] for item in sigma])
      s = values[i][j:j+4]
      s = np.array([item[1] for item in s])
      emittance_guess = np.mean(sigma**2)
      beta0_quess = np.min(s)
      s0_guess = np.mean(s)
      initial_quess = [emittance_quess, beta0_quess, s0_quess]
      print("\nInitial guess:", initial_guess)
      result = minimize(emittance_functn, initial_guess, args=(sigma,s),

    method='Nelder-Mead')

      emittance_opt, beta0_opt, s0_opt = result.x
      if key in all_emmitance_eq:
        all_emmitance_eq[key].append(result.x)
      else:
        all_emmitance_eq[key] = [result.x]
      print("Result of fitting (emittance_opt, beta0_opt, s0_opt):",
      \hookrightarrow result.x)
      #Optional plotting
      if plot_bool:
        s_{fit} = np.linspace(min(s), max(s), 1000)
        sigma_fit = np.sqrt(emittance_opt*(beta0_opt + (s_fit -

    s0_opt)**2/beta0_opt))
        plt.figure(figsize=(5, 3))
        plt.scatter(s, sigma, label='Measured Points')
        plt.plot(s_fit, sigma_fit, label='Fitted Function', color='red')
        plt.xlabel('s')
        plt.ylabel('sigma')
        #plt.title('Measured Points and Fitted Function')
        plt.legend()
        plt.grid(True)
        if i == 0:
          print('Case for r_x')
        elif i == 1:
          print('Case for r_y')
        elif i == 2:
          print('Case for r_ms')
        plt.show()
```

```
print("\n\n\nRESULTS FOR EMITTANCE OPTIMIZATION:")
for ID in all_emmitance_eq.keys():
   print(" ID:", ID)
   sets = all_emmitance_eq[ID]
   for i in range(len(sets)):
      print('\t', sets[i][0])
```